

INTEGRATION OF OPTOELECTRONICS AND MICROFLUIDICS FOR
BIOLOGICAL AND CHEMICAL SENSING

Thesis by

Mark Lee Adams

In Partial Fulfillment of the Requirements

for the Degree of

Doctor of Philosophy

California Institute of Technology

Pasadena, California

2004

(Defended December 12, 2003)

© 2004

Mark L. Adams

All Rights Reserved

Acknowledgement

I would like to thank my loving wife, Beth, for her support throughout my time in graduate school. Although it has been a constant struggle, we have persevered and grown closer in the process. She has been a constant friend and companion who has kept me grounded through my time as a graduate student. I would also like to thank several individuals who have enlightened me through conversation and have in general made my life as a graduate student much more enjoyable. They include Brett Maune, Ali Husain, David Barsic, Terrell Neal, Jeremy Witzens, Tomo Yoshie, Joshua Marcus, Dr. Marko Loncar, Dr. Jordan Gerton and Carl Hansen. Finally I would like to thank my advisor, Professor Axel Scherer, for providing me the opportunity and resources to complete my Ph.D.

Abstract

Over the past decade, rapid advances in microfluidics have led to the creation of valves, pumps, mixers, multiplexers, along with a large variety of other devices. This technology has allowed for many fluidics applications to be performed on a chip that is approximately an inch square in area. Such applications include cell sorting, PCR on chip, crystal growth, combinatorial mixing and many others. Although the complexity of these devices may seem overwhelming, they are based on simple process called multilayer soft lithography, which uses a silicone-based elastomer to create these amazing devices. However, with the current state of technology, the applications are somewhat limited. New devices need to be created to further such fields as fluidic logic and biomimetics.

Another major issue that challenges true acceptance of microfluidics is the need for a typically large interrogation setup to determine what is actually happening in the flow cell. In general, a microfluidic chip is placed under a bench top optical microscope in order to perform either colorimetric, absorption, or luminescence spectroscopy. Through these methods everything from cells to chemicals can be identified; however, a true lab-on-a-chip must not rely on something as cumbersome as a microscope. Integrated sensors must be developed to truly make lab-on-a-chip reasonable.

Through this thesis, several approaches for realization of integrated optoelectronic microfluidic systems are presented. The systems are capable of performing optical interrogation of analyte, from both outside of the flow cell as

well as directly inside a flow channel. Also, some novel microfluidic devices which should pave the way for greater advancement in the field of microfluidics are discussed. Through the technologies presented, true lab-on-a-chip systems should be even closer to realization.

Table of Contents

| | |
|--|-------|
| Chapter 1 – Introduction | 1-1 |
| Chapter 2 – Overview of Microfluidics | 2-5 |
| Microfluidic Flow Dynamics | 2-8 |
| Pulse Injection Simulation and Verification | 2-14 |
| Microfluidic Diode (One-Way Valve) | 2-19 |
| Microfluidic Amplifier | 2-24 |
| PDMS Etching | 2-27 |
| Electrostatic Valves | 2-28 |
| Chapter 3 – Early Integration: CMOS Imagers and Spectroscopy | 3-30 |
| CMOS Absorption Spectroscopy | 3-32 |
| Broadband Absorption Spectroscopy | 3-37 |
| Theory | 3-39 |
| Modeling | 3-41 |
| Fabrication | 3-48 |
| Results and Discussion | 3-51 |
| Fluorescence Spectroscopy | 3-52 |
| Image Acquisition and Analysis | 3-56 |
| On-chip Flow Cytometry and μ FACS | 3-57 |
| Emission Sources | 3-59 |
| Chapter 4 – Vertical Cavity Enhancement | 4-61 |
| Theory | 4-61 |
| Simulation | 4-65 |
| Fabrication | 4-69 |
| Testing | 4-71 |
| Results and Discussion | 4-73 |
| Chapter 5 – Photonic Crystal Lasers | 5-75 |
| Nanocavity Design | 5-77 |
| Photonic Crystal Nanolasers as Chemical Sensors | 5-91 |
| Fabrication Procedure | 5-92 |
| Microfluidic Integration of Photonic Crystal Cavities | 5-96 |
| Chemical Sensing Using Photonic Crystal Nanolasers | 5-99 |
| Detection and Quantization of Nanoparticles | 5-104 |
| Multiphoton Cavity Processes | 5-106 |
| Dense Integration of Laser Sensors | 5-108 |
| Conclusions | 5-112 |
| References | 5-114 |
| Appendix A – FDTD Computer Code | 5-118 |
| Appendix B – Fabrication Procedures | 5-135 |
| Appendix D – Imager Maker Code | 5-151 |

List of Illustrations and Tables

| | |
|---|------|
| Figure 1. Transmission characteristics of PDMS, glass and fused silica. The transmission is very similar in the visible wavelength range. | 1-2 |
| Figure 2. Simulation results for a 100 μm wide flow channel as a fluidic plug progresses in time. | 2-15 |
| Figure 3. (a) A 10 μm channel and (b) a 50 μm channel showing the initial fluid plug and the final dispersion. | 2-16 |
| Figure 4. A picture of the device used to perform the pulse injection experiments. The dead volume of the injection device is highlighted. This volume can be minimized through careful design of the device. | 2-17 |
| Figure 5. Pulse injection results for 100 μm wide channels. As can be seen, Poiseuille flow is developed in the channels via peristaltic pumping ¹ | 2-17 |
| Figure 6. Simulation results of flow induced via (a) peristaltic pumping and (b) pressure driven flow in an elastomer flow channel. The flow profile develops the parabolic shape typically encountered in Poiseuille flow. The dispersion is indicated for each flow type. | 2-19 |
| Figure 7. Microfluidic diode illustration. The flow from the right direction is stopped as the flap presses against the orifice of the left channel. Flow from the left is allowed to flow since the flap is unobstructed in the right channel. | 2-21 |
| Figure 8. (a) Fluidic diode with the flap rolled upon itself. (b) The flap was unrolled into the channel. | 2-21 |
| Figure 9. (a) Microfluidic diode device with 4 pairs of two opposing diodes. (b) Diodes tested with 100 μM fluorescein. The fluorescein flows in the direction of flow for the bottom diode and does not flow in the opposing device. The channel does eventually fill due to dead volume filling, but fluid does not leak past the diode. | 2-22 |
| Figure 10. A flow rate vs. pressure curve for the three fluidic diode geometries described above. This curve is analogous to an electronic diode's I-V curve. | 2-24 |
| Figure 11. Microfluidic pressure amplifier schematic. | 2-25 |
| Figure 12. Picture of the amplifier structure taken with an optical microscope shows (a) the valve open and (b) the valve closed. The pressure necessary for sealing was approximately the same as without the amplifier. | 2-26 |
| Figure 13. Miniaturization of a spectroscopic measurement system by use of a commercial CMOS imager. | 3-34 |
| Figure 14. (a) A schematic illustration of how the absorption spectroscopy is performed. (b) A PDMS microfluidic chip imaged by the APS CMOS imager. The light source is a 588 nm λ_{max} AlInGaP LED and the channels contain 7.5 mM to 30 μM bromophenol blue solutions. The far left channel is empty and the far right channel contains water for reference. This is an 8 bit image which is considerably less than the 12 bit resolution of the imager. | 3-34 |

| | |
|---|------|
| Figure 15. Absorption spectra of various Bromophenol Blue and Orange G concentrations taken with a Shimadzu spectrophotometer and the APS CMOS imager..... | 3-37 |
| Figure 16. Absorption spectra of a 31 layer SiO ₂ /Si ₃ N ₄ Fabry-Perot cavity..... | 3-38 |
| Figure 17. Convention defining the positive directions of the electric and magnetic vectors for p-polarized light..... | 3-45 |
| Figure 18. Illustration of the incident wavefront on a simple thin film..... | 3-46 |
| Figure 19. (a) 31 layer $\lambda/4$ dielectric thin-film reflector. (b) 31 layer $\lambda/4$ dielectric thin-film half-wave cavity..... | 3-48 |
| Figure 20. (a) Geometrically graded filter grown on a reactive sputter deposition system. The grading is produced by placing the sample at an angle to the sputter source. (b) Patterned filter with flow substrate sealed to the surface..... | 3-50 |
| Figure 21. Transmission spectra for graded filter showing the minimum and maximum wavelength filter responses..... | 3-51 |
| Figure 22. Spectrum of bromophenol blue taken by the CMOS imager with graded filter and taken by a Shimadzu 1601 spectrophotometer..... | 3-52 |
| Figure 23. A quarter wavelength dielectric thin-film filter grown on the CMOS imager to block the excitation light, but pass, with minimal loss, the emission light..... | 3-53 |
| Figure 24. Fluorescent absorption and emission spectra for fluorescein. Blocking filter absorption spectrum shown in relation to second y axis. The emission peak corresponds to a region just outside the block band where the transmission is roughly 50%. This can easily be improved by constructing a narrower band-blocking filter..... | 3-54 |
| Figure 25. 170 μ M and 85 μ M fluorescein in 100 μ m wide by 14 μ m flow channels on 460 nm blocking filter illuminated by an Ar ion laser at 488 nm with no. 2 and no. .5 neutral density filters in the beam path to decrease the excitation light intensity so that the imager is not saturated..... | 3-55 |
| Figure 26. (a) Cell sorting chip as compared to a penny. (b) Image of cell sorter chip taken with the integrated imaging system showing the T channel, pump, and valves..... | 3-58 |
| Figure 27. Schematic illustration of a vertical-cavity based analysis system... | 4-61 |
| Figure 28. Simulation of the vertical cavity transmission (red) as a function of concentration at $\lambda = 591$ nm. The flow structure without the cavity (blue) is shown for comparison..... | 4-66 |
| Figure 29. Absorbance of the vertical cavity structure vs. the noncavity structure. The inset shows that the noncavity absorbance is linear as expected..... | 4-67 |
| Figure 30. Simulation of the vertical cavity transmission (red) vs. the same flow structure without a cavity (blue). The cavity is designed to operate at $\lambda = 591$ nm..... | 4-68 |
| Figure 31. Variable tuning of the vertical cavity structure as a function of separation distance..... | 4-69 |
| Figure 32. Fabrication procedure for creating the vertical cavity structure. Significant care must be given to the fabrication tolerances for any chance of success..... | 4-71 |

- Figure 33. Measured vertical cavity spectrum for a cavity tuned to 591 nm. The FWHM of the cavity is much broader than the simulation, which is a result of many factors including lower mirror reflectivity, shift in mirror wavelength, and loss of phase matching..... 4-72
- Figure 34. Dispersion diagram for the modes supported in the triangular lattice planar photonic crystal ($r/a = 0.3$ this time). Mode profiles for one component of the E field in the dielectric (red) and air (blue) band, take at the X point, are also shown..... 5-78
- Figure 35. (a) Conventional single-defect cavity ($p=0$). When structure is "cut" along the dashed line, and two PPC half-planes are dislocated along ΓX direction by $p/2$, (b) high-Q cavity can be formed ($p=0.25 \cdot a$). 5-81
- Figure 36. Defect modes of the cavity with $p/a=10\%$ and $r_{\text{def}}=0.2a$. (a) Cavity supports two dipole modes, and their profiles are shown (B_z component and vector of the E field). Spectrum of the modes supported in the cavity, obtained using 3-D FDTD, is also shown. The bandgap is shown in white. (b) Amplitude of the E field is shown. It can be seen that light is localized in the small defect hole. 5-83
- Figure 37. (a) Dependence of the eigen-frequencies of the two dipole modes of the cavity on the amount of dislocation introduced (p), and the size of the defect hole (r_{def}). (b) Dependence of the vertical quality factor of the HQ mode on p and r_{def} . Only five layers of photonic crystal surrounding the defect hole was used. 5-85
- Figure 38. Air-band and dielectric-band edge dependence on the refractive index of environment (n_{env}) surrounding PPC slab, for $r/a=0.3$ (red) and $r/a=0.4$ (blue). 5-86
- Figure 39. Dependence of the (a) Q factor and (b) eigen-frequency of cavity resonance on the refractive index of analyte introduced in the cavity with $p/a=25\%$ 5-88
- Figure 40. Dependence of E_{def} on refractive index of the environment n_{env} 5-90
- Figure 41. Scanning electron micrograph and calculated field distribution ($|E_{\text{ampl}}|$) of a photonic nanocavity laser sensor. It can be seen that the energy of the mode is mostly confined to the central defect hole..... 5-92
- Figure 42. SEM micrograph of high-Q planar photonic crystal cavity, defined in the suspended membrane 5-95
- Figure 43. Fabrication procedure for PPC lasers made in InGaAsP material. RF sputtering (1) is used to deposit dielectric and is followed by deposition of PMMA e-beam resist (2). E-beam lithography is used to define patterns in PMMA (3) and RIE to transfer them into Si_3N_4 (4). Finally, patterns are etched into InGaAsP using ICP-RIE (5) and the membrane is released from the substrate in HCl (6). Final structure is a free standing InGaAsP membrane with four quantum wells (thin red layers). 5-96
- Figure 44. (a) A planar photonic crystal (PPC) structure embedded in a PDMS flow cell. (b) The PPC lasers can be seen underneath the flow channels. The channels are $40\mu\text{m}$ wide and spaced $15\mu\text{m}$ apart. 5-99
- Figure 45. Experimental setup. Pump beam ($\lambda=830$ nm) is focused on the sample using high-power NIR lens (100x). Si detector behind beam splitter (BS) is

| | |
|---|-------|
| used to monitor the pump power. Emission from the sample is collected using the same lens, and is analyzed with an optical spectrum analyzer (OSA). The emission from photonic crystal resonators can also be monitored with a cooled CCD camera or a fiber-optic spectrometer using a pair of flip-up mirrors..... | 5-100 |
| Figure 46. (a) Sensor response measured from 6 nanocavities with a lattice parameter of $a=446$ nm (dashed lines) and $a=460$ nm (solid lines) as a function of p/a dislocation parameter. The three curves correspond to the laser wavelength with air, methanol and IPA backfilled into the cavity. (b) Spectrum change and (c) threshold curve change of laser before and after filling with IPA. | 5-102 |
| Figure 47. Dependence of (a) a/λ and (b) λ of HQ mode on refractive index of the environment (n_{env}). Three different cavities, labeled R_6C_3 , R_7C_5 and R_7C_3 were tested. | 5-103 |
| Figure 48. The photoluminescence spectra of PPC laser R_7,C_3 with 100nm diameter beads in water interfacing with the cavity. The spectra show that the peak wavelength shift is quantized according to the number of beads interacting with the cavity..... | 5-106 |
| Figure 49. A Jablonski diagram of a four-photon process. The planar photonic crystal laser could supply the necessary energy to pump the molecule into its highest excited state $ N\rangle$ | 5-107 |
| Figure 50. (a) Fabricated structure consists of three cavities integrated within the same photonic crystal mirror. Defect holes are indicated by arrows, and their size increases from right to left. (b) Resonances detected in each cavity. Mode experience blue-shift as the size of defect hole increases. Positions of pump-beam are shown. | 5-109 |
| Figure 51. Simultaneous emission from two adjacent nano-lasers pumped simultaneously using big pump spot. Insets show near-field image of the light emitted from nanolasers..... | 5-111 |
| Table 1. Microfluidic diode performance as a function of geometry..... | 2-22 |
| Table 2. Sorting accuracy for the integrated μ FACS..... | 3-59 |
| Table 3. Transmission measurements normalized for maximum transmission and path length..... | 4-74 |
| Table 4. InGaAsP wafer structure..... | 5-93 |

Chapter 1 – Introduction

Over the past few years, the application of micromachining techniques has grown rapidly to include many devices such as accelerometers [1, 2], pressure sensors [3], ink-jet print heads [4], fiber-optic communications [5, 6], displays [7], and microfluidics [8-12]. Two of the most common methods for the production of microelectromechanical systems (MEMS) include bulk micromachining and surface micromachining. These methods employ silicon or glass as their main substrate component. Bulk micromachining involves etching away single-crystal silicon to form three-dimensional structures, while surface micromachining centers around the addition of different materials such as polysilicon, metals, silicon nitride, silicon dioxide, etc., to define structures. Both methods are somewhat limited by the semiconductor substrates which increase the difficulty of multilayer device production. Careful consideration must also be given to production facilities and process conditions to realize acceptable device yields.

An alternative microfabrication technique that has gained popularity in recent years is elastomer replica molding, loosely referred to as soft lithography. It has been used to make blazed grating optics, stamps for chemical patterning, and microfluidic devices [13, 14]. This technique involves curing an elastomer, typically silicone, on a micromachined mold. The mold can be generated using bulk or surface micromachining, but is typically generated via photolithography. A standard mold can be generated by exposing a thick UV sensitive photoresist through a high-resolution contact mask. The pattern can then be developed and

baked for a short while to finish the mold. Through the use of these techniques many microfluidic devices such as peristaltic pumps, valves, mixers, and cell sorters have been developed [15-17].

A major problem that exists with most semiconductor-based microfluidic structures is the inability to perform optical analysis on the device's contents. Due to the absorption of silicon, these devices are limited to use in the infrared range. Visible/UV spectroscopy is virtually impossible to perform without an amazingly elaborate device. In fields such as biochemistry, this becomes a very limiting factor since many experiments are based on visible/UV absorption and fluorescence spectroscopy. Specific silicone elastomers, such as polydimethylsiloxane (PDMS), circumvent this problem since they are optically transparent and have similar UV absorption characteristics to those of glass as shown in Figure 1. This property allows for integration of elastomer microfluidic devices and optoelectronics to perform spectroscopy.

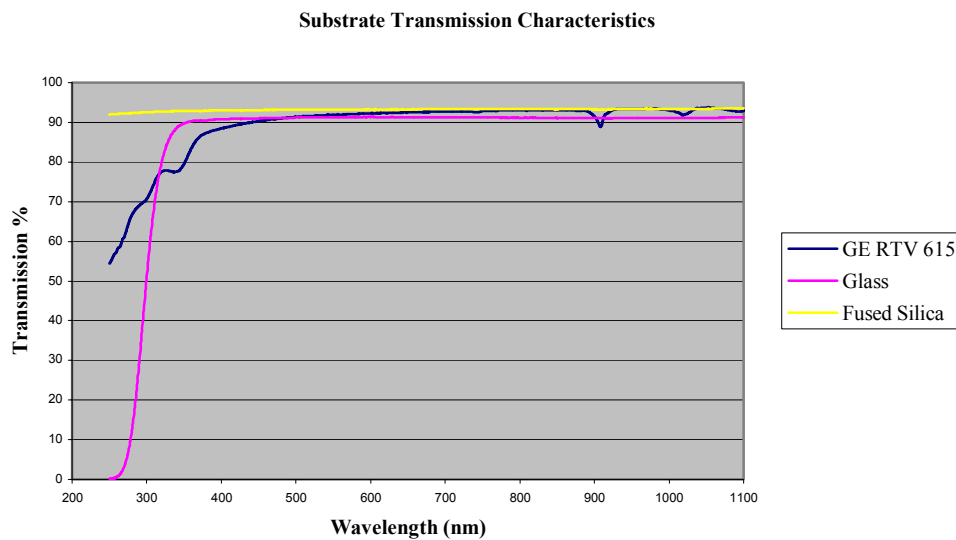


Figure 1. Transmission characteristics of PDMS, glass and fused silica. The transmission is very similar in the visible wavelength range.

Since the advent of microfluidics, a multitude of devices with various functions have been developed. Technologies such as microelectromechanical systems (MEMS) and multilayer soft lithography (MSL) have become commonplace. A great deal of effort has gone into creating miniaturized devices for a wide array of purposes including cell sorters, enrichment chips, protein crystallization, DNA sizing and sorting, PCR amplification [13-18]. However, the full impact of microfluidics has yet to be felt. New devices are being created daily with ever greater complexity and functionality and with one important overarching goal. A laboratory-on-a-chip, once thought to be only science fiction, has become a realistic possibility and today's microfluidic technology is now enabling it ever to replace conventional instrumentation. Unfortunately the vast majority of miniaturization has concentrated on the chip functionality. Although this may seem intuitive, one must realize that the fluidic chip is only part of a functional analysis system. In order to fully develop a laboratory-on-a-chip, other pieces must be assembled to complete a functional testing tool.

Perhaps, the most important piece missing from the miniaturization puzzle is a suitable detection system. Some type of transducer is necessary to analyze exactly what is happening inside the fluidic chip. Current systems rely on bulky bench top equipment such as inverted microscopes or stereoscopes to provide a user with information pertaining to the microfluidic chip. Although, this technique is practical within a laboratory research environment, it hardly meets the requirements for a portable lab-on-a-chip for disease diagnostics or chemical analysis. A better approach is to miniaturize the transducer so that it is of

comparable size to the microfluidic chip. However, many trade-offs exist must be addressed before a suitable detection system to be developed.

For a detection system to be widely accepted, it must be small, inexpensive, easy to use, and most importantly accurate. The system needs to have similar performance characteristics to technologies used today. This presents a significant problem that must be studied carefully to allow for a solution that best meets these qualifications.

In order to design a suitable detection system, one must first fully understand the microfluidic chip. The study of multilayer soft lithography (MSL) yielded a great deal of information and techniques which were used to explore detection system design. While investigating MSL, a need for other microfluidic devices was discovered. A more in depth understanding of flow channels and microfluidic flow was acquired through design, modeling, and experimentation. To this end, the beginning of this thesis discusses microfluidic design and implementation. Fluidic flow is modeled via finite difference time domain (FDTD) and novel microfluidic devices are presented in detail.

Chapter 2 – Overview of Microfluidics

Multilayer soft lithography is primarily based upon the molding of layers of silicone elastomer. Polydimethylsiloxane (PDMS) was originally created to be used as a room temperature vulcanized (RTV) sealing agent, and has many attributes which make it a good choice for microfluidic devices. Since it is an elastomer, it has a Young's modulus much lower than that of silicon or silicon dioxide, and is chemically inert and optically transparent. The absorption characteristics of PDMS are very similar to that of glass, which makes it ideal for integration with optical detection techniques. PDMS is also very inexpensive, which is of some importance when discussing lab-on-a-chip platforms.

PDMS was first applied to the field of micromachining by Professor George Whitesides' group at Harvard University. Whitesides' group was able to produce elastomer structures through a process called replica molding [13, 14]. This process allowed for a device to be created from a master mold. He coined the term soft lithography to describe the process. A mold could be fabricated through a variety of techniques such as surface or bulk micromachining, but was most typically created from a photoresist mold.

A photoresist mold is created through standard micromachining practices created by the semiconductor electronics business. A mold is made by spinning an ultraviolet (UV) light sensitive polymer onto a substrate, i.e., silicon wafer, and exposing it through a mask to UV light. The mold can then be rinsed in photoresist developer to develop the pattern that appeared on the mask. Common

resist types include Shipley SPR 1800 series, Shipley SPR 5740, Microchem SU-8, and Clariant AZ100.

Once the photoresist mold has been generated, the replica molding process can continue. The mold is treated with trimethylchlorosilane (TMCS) to prevent the PDMS from adhering to the photoresist. This step is very critical since one typically wishes to reuse the mold many times. TMCS is deposited as a monolayer through gas phase deposition. Essentially, the mold is placed in a sealed container with a small amount of TMCS inside. The TMCS evaporates and coats the photoresist mold. After the mold has been surface treated, it is ready for PDMS to be poured on it.

PDMS is a two part mixture including the bulk elastomer and a curing agent. The two parts are mixed with varying ratios depending upon the application. For example, five parts elastomer to one part curing agent is commonplace. Other common ratios include 3:1, 10:1, 20:1, 30:1. PDMS requires mixing and degassing before it can be applied to the mold. A Keyence HM-10 hybrid mixer is used to mix and degas the PDMS. Once mixed it is poured onto the photoresist mold and further degassed using a small vacuum chamber. The PDMS coated mold is then placed in an 80°C oven to cure. The curing time varies depending on the manufacturer of the PDMS, but typically takes between thirty minutes and two hours.

After the PDMS has cured, the flow device can be cut out from the mold. Holes are then punched into the device to allow fluid entry and the device is sealed to a new substrate such as a glass slide. There are many ways to seal the

device, but one of the most common involves spraying both the PDMS device and the sealing substrate with ethanol, blowing them dry with nitrogen and sealing them together. The sealed device is then placed in an oven at 80° C for several hours to cure. This technique allows for the device to withstand pressures up to 30 psi.

Although a great deal of functionality can be designed into a single layer, the creation of multilayer soft lithography (MSL) by Professor Stephen Quake's group added another dimension to standard soft lithography. By combining multiple layers of PDMS together active devices such as valves, pumps, and mixers are created [15-17]. MSL allowed for a huge advancement in the functionality of microfluidic chips through the use of such techniques as large scale integration.

MSL is responsible for the creation of devices such as valves, peristaltic pumps, circular mixers, multiplexers, and many others. The creation of active devices is the primary advantage of MSL. Instead of relying solely on diffusion one can actively pump fluids around at much faster rates [16]. In addition, complex functionality can be built into the fluidic chip for applications such as enrichment, cell sorting, PCR, and protein crystallization.

The only significant difference in the fabrication procedure is now instead on one layer, there are at least two. The layers typically consist of a flow layer and a control layer. They are joined together through a technique developed in the Quake lab in which the two layers are comprised of different ratios of curing agent to elastomer, i.e., flow layer is 5:1 and the control layer is 20:1. After

placing the two layers together, the assembly is placed into an 80° oven and baked for several hours. The final assembly is then no longer two layers, but one composite layer comprised of the two original ones.

Multilayer soft lithography provides an enormous building block for creating microfluidic devices. However, in order to fully comprehend the power of this technique, a strong background in microfluidic fundamentals is required. With this knowledge one can design and create devices with new functionality.

Microfluidic Flow Dynamics

Fluid flow can be broadly classified as either a viscous flow or an inviscid flow. An inviscid flow is one in which viscous effects do not significantly influence the flow and thus are neglected. In a viscous flow the effects of viscosity can not be ignored. Viscosity can be thought of as the internal stickiness of a fluid. It accounts for the energy losses associated with transport of a fluid in a channel and plays a primary role in the generation of turbulence. Most liquids of interest are viscous, e.g., air and water [18].

Viscous flow can be further classified into either laminar or turbulent flow. In laminar flow, fluid flows with no significant mixing of neighboring fluid particles except through molecular diffusion. In a turbulent flow, fluid motions vary irregularly so that flow velocity and pressure show a random variation in time. This flow instability is what causes neighboring fluids to mix readily in turbulent flow.

The flow regime depends upon three physical parameters which describe the flow conditions. These are the length scale of the flow field (i.e., the channel

width/diameter), the spatial average of the flow velocity, and the kinematic viscosity. If the length scale is large or the velocity is large enough, the flow may be turbulent. This is also true if the kinematic viscosity of the fluid is very small. In general these parameters are combined into a single parameter called the Reynolds number. It is a dimensionless parameter defined as

$$\text{Re} = \frac{VL}{\nu} \quad 2.1$$

where L and V are the characteristic length and velocity, respectively, and ν is the kinematic viscosity. Flow is laminar if $\text{Re} < \text{Re}_{\text{crit}}$ which is defined as the critical Reynolds number. The critical Reynolds number is dependent upon the geometry of the flow structure. For a rectangular microfluidic channel the critical Reynolds number is on the order of 5,000.

For noncompressible, Newtonian fluids such as water, the velocity of the fluid is related to the pressure on the fluid by the Bernoulli equation. It is defined as

$$\frac{V^2}{2} + \frac{p}{\rho} + gh = \text{const} \quad 2.2$$

where V is the average velocity of the fluid, p is the pressure, ρ is the density, g is the gravitational acceleration, and h is the height. This equation is very useful for analyzing flow within channels and is probably the most well known equation for fluid flow. The Bernoulli equation can be derived by applying Newton's second law of motion to a fluid particle. Although the derivation will not be presented here, it is useful to realize the relation between the pressure exerted by a fluid and its velocity. Pressure is defined as

$$p = \lim_{\Delta A \rightarrow 0} \frac{\Delta F_n}{\Delta A} \quad 2.3$$

where ΔF_n is the incremental normal compressive force acting on the incremental area ΔA . However, for most applications the pressure can be taken as $p=F/A$.

Fluid flow is best described by the Navier-Stokes equations. Although it is empirically impossible to solve the Navier-Stokes equations for all but the simplest of systems, the fluidic dynamics of a particular system can be studied through computer modeling. A 2-D finite element model was used to simulate the flow of a fluid inside a rectangular channel. The model was simplified by assuming a 10:1 ratio between the width and height of the channel. The assumption is based upon the fluidic resistance of a microfluidic channel. Given laminar flow conditions and a Newtonian fluid, the volume flow rate of a rectangular channel is given by

$$Q = \Delta P / R \quad 2.4$$

where ΔP is the pressure difference and R is the fluidic resistance. R is proportional to the channel dimensions and is defined as

$$R = \frac{12\mu L}{wh^3} \quad 2.5$$

where L , w , and h are the length, width, and height of the channel, respectively. Since w and h are interchangeable, the fluidic resistance simply assumes a high aspect ratio [19].

In order to accurately model the fluid flow inside the channel, a joint FEM/FDTD simulation was created. The model is based upon the differential continuity equation, the Navier-Stokes equations, and Fick's laws for mass

transport. Each of these equations is critical to understanding how the fluidic system was modeled so they will be discussed in some detail below.

In its most general form the differential continuity equation can be expressed as

$$\frac{D\rho}{Dt} + \rho \nabla \cdot \vec{V} = 0 \quad 2.6$$

where ρ is the density of the media and $\vec{V} = u\hat{i} + v\hat{j} + w\hat{k}$ is the velocity vector.

However, for incompressible flows in which the density does not change as a function of time the continuity equation simplifies to

$$\nabla \cdot \vec{V} = 0 \quad 2.7$$

The Navier-Stokes equations then take the vector form

$$\rho \frac{D\vec{V}}{Dt} = -\nabla p + \rho \mathbf{g} + \mu \nabla^2 \vec{V} \quad 2.8$$

where \mathbf{g} is the gravitational constant and μ is the viscosity. Through the vector form both sets of equations can be applied to other coordinate systems, although for the simulation purpose, rectangular coordinates were chosen [18].

The simulation uses a two-dimensional model with the length of the channel along the x axis and the width of the channel along the y axis. The model assumes a noncompressible Newtonian fluid with all streamlines parallel to the walls of the channel. Since all the streamlines are parallel to the walls only the x-component of the velocity will be non-zero. If the no-slip conditions are used as the boundary conditions, the velocity at the sidewall is zero and the differential equation simplifies to

$$\frac{\partial p}{\partial x} = \mu \left(\frac{\partial^2 u}{\partial y^2} + \frac{\partial^2 u}{\partial z^2} \right) \quad 2.9$$

which can be solved through numeric approximation by FEM. One can further simplify Eq. 2.9 by invoking the wide channel approximation in which the width of the channel exceeds the height of the channel by at least a factor of 8. This approximation was validated by modeling Eq. 2.9 through FEM. Through this approximation Eq. 2.9 becomes

$$\frac{\partial p}{\partial x} = \mu \frac{\partial^2 u}{\partial y^2} \quad 2.10$$

which can empirically be solved and leads to a velocity that can be expressed as

$$u(y) = \frac{1}{2\mu} \frac{dp}{dx} (y^2 - ay) \quad 2.11$$

where a is the channel width. By combining Eqs. 2.4-2.5 and by noting that the maximum velocity occurs at the center of the channel, Eq. 2.11 can further be simplified to yield

$$u(y) = \frac{-4u_{\max}}{a^2} (y^2 - ay) \quad 2.12$$

where u_{\max} is the maximum velocity in the x direction. This velocity profile can then be used for the FDTD modeling.

It becomes necessary to include Fick's laws into the model if something of interest is inside the fluid, e.g., dye in water. According to Fick's first law (in one dimension)

$$J = -D \frac{dC}{dx} \quad 2.13$$

where J is the mass flux of the material, D is its diffusion constant, and C is the initial concentration. If one assumes that the material, i.e. dye, is conserved, the one dimensional mass transport equation becomes

$$\frac{\partial C}{\partial t} = \frac{\partial J}{\partial x} \quad 2.14$$

Since the concentration of the diffusing material depends upon both time and space, the partial derivative is used in place of the ordinary derivative in Fick's first law, Eq. 2.10. Fick's second law in one dimension is given by combining Eq. 2.10 with 2.11 and can be written as

$$\frac{\partial C}{\partial t} = D \frac{\partial^2 C}{\partial x^2} \quad 2.15$$

Although molecular diffusion described above is present, it is almost always dominated by the more rapid transport mechanism performed by the motion of the fluid itself. This motion was discussed earlier in this section and is describe through the Navier-Stokes equations. This kind of transport is typically referred to as *advection*. Advective transport is expressed in terms of the flux vector along a given axis per unit perpendicular to that axis [18]. For the simulation's case the flux is given by

$$J = uC \quad 2.16$$

where u is the velocity in the x -direction and C is the concentration of the material. Given the advective flux, the total mass transport of the system (in one dimension) is given by

$$\frac{\partial C}{\partial t} + \frac{\partial}{\partial x}(uC) = D \frac{\partial^2 C}{\partial x^2} \quad 2.17$$

The mass transport equation for multiple dimensions can then be obtained by considering mass flux components all each coordinate direction. The final differential equation which is solved through simulation is as follows

$$\frac{\partial C}{\partial t} + u \frac{\partial C}{\partial x} + v \frac{\partial C}{\partial y} = D \nabla^2 C \quad 2.18$$

A full listing of the program developed to perform the simulation is listed in appendix A.

Pulse Injection Simulation and Verification

One of the first applications for the FDTD model was to examine how a plug of fluid disperses and travels inside a flow channel. The primary example that this application applies to is fluidic metering. Many applications rely on very precise amounts of fluid to be delivered during a certain time interval. For instance, drug delivery is an example in which it is critical that the correct amount of medicine is delivered to the subject in an appropriate time. Also there are many biological and chemical experiments which require reagents to be combined in very precise amounts to facilitate a reaction.

A problem occurs when one tries to send a plug of fluid down a microfluidic flow channel. Although the fluidic soliton exists, it is extremely difficult to reproduce it within a microfluidic channel in which flow is pressure driven, as is the case with most active PDMS devices. Instead of the plug maintaining uniformity as it travels down the channel, it disperses and takes on a Gaussian shape. As stated above, the flow profile depends upon the geometry of the flow channel. For example, a 100 μm wide by 10 μm high channel was

simulated under pressure driven flow conditions. Three different simulation times are shown in Figure 2.

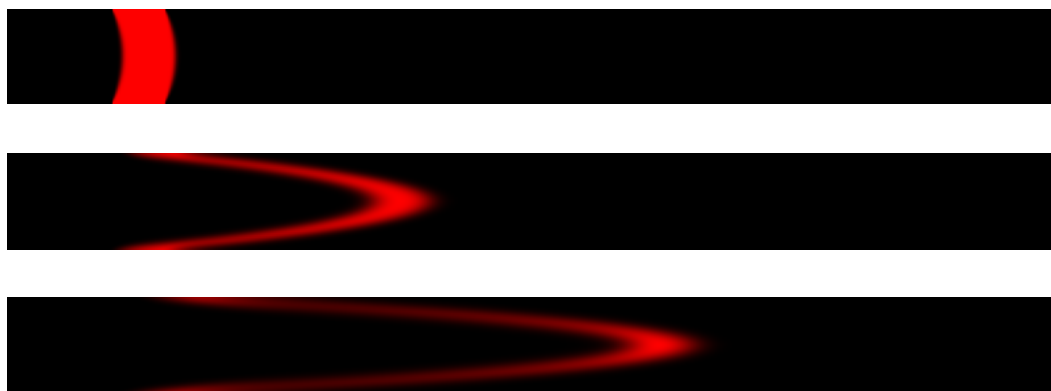


Figure 2. Simulation results for a 100 μm wide flow channel as a fluidic plug progresses in time.

One can see that the fluid profile for Poiseuille flow develops as time elapses.

Although, the plug dispersion is dominated by advection, one must carefully consider the diffusion of the material. For the typical dimensions of a microfluidic channel, diffusion plays a large role in the dispersion. The idea behind the simulation was to make sure that the fluid did not diffuse more than necessary. Unfortunately, the simulation over estimates the material diffusion, due to numerical diffusion inherent in the model. The material diffusion can be expressed as

$$x_{diff} = 2\sqrt{Dt} \quad 2.19$$

where D is the diffusivity of the material and t is the time. The numerical diffusion can then be calculated by subtracting the material diffusion from the total amount of diffusion that occurred during the simulation. For the simulations presented the numerical diffusion was approximately a factor of three greater than

the material diffusion. Figure 3 illustrates the numerical diffusion inherent in the model. Both a 10 μm wide and a 50 μm wide channel are shown with the material diffusion indicated. Since both simulations were run for the same amount of time the material diffusion is identical in both channels. The numerical diffusion can be improved by either increasing the order of the model or by decreasing the time step and discretization steps. However, both of these solutions require a substantial increase in processing time and power.

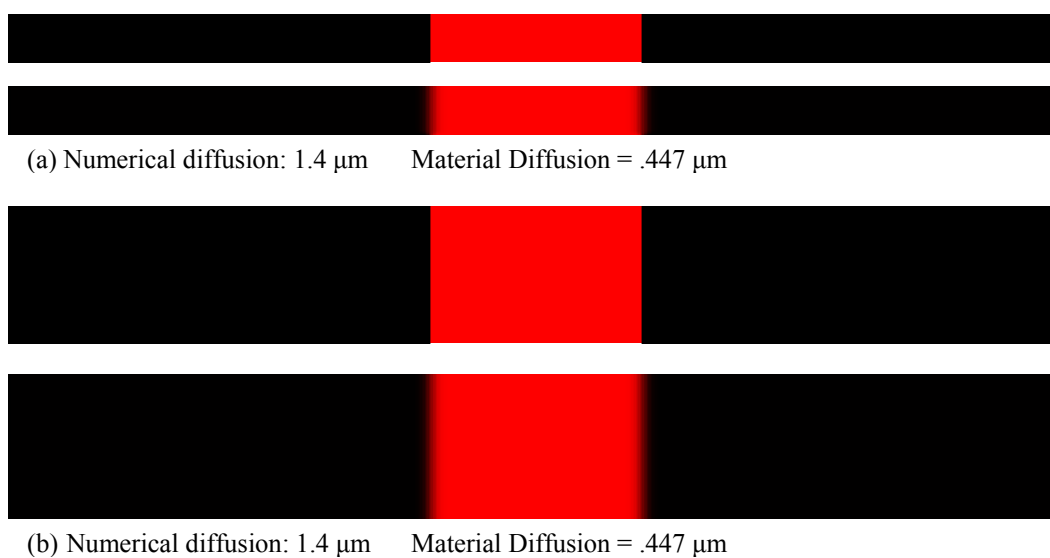


Figure 3. (a) A 10 μm channel and (b) a 50 μm channel showing the initial fluid plug and the final dispersion.

The simulation was experimentally verified by creating a cross injection flow channel system. Photoresist molds were made for the cross injection devices through standard processing techniques. The fabrication process is described in detail in Appendix B under the section – Molds for Poiseuille Flow. After the molds were fabricated, the PDMS flow structure was created. An example of the device is shown in Figure 4. Each of the devices was tested and compared to the simulation. Some of the results of the experiments are shown in Figure 5.

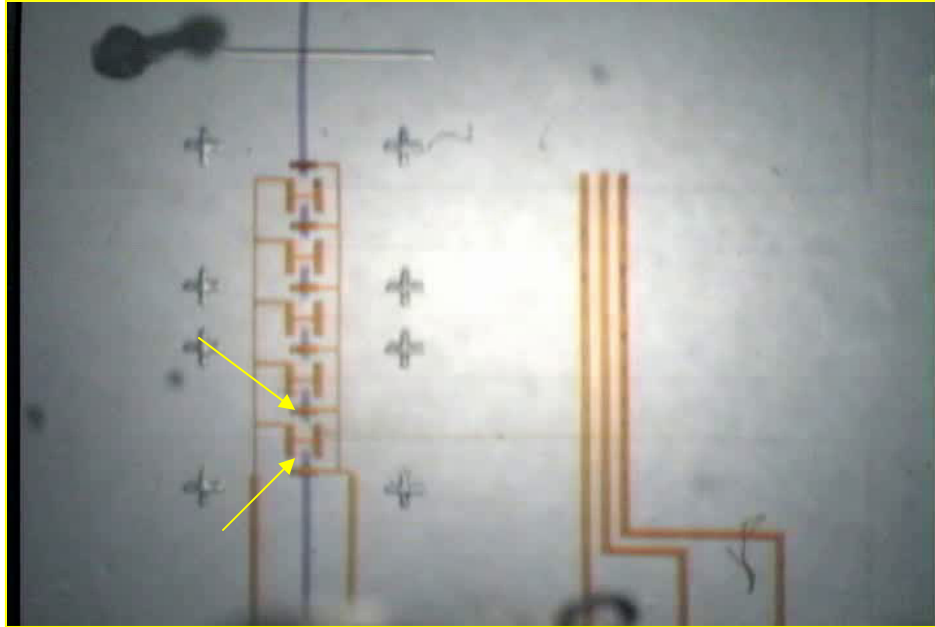


Figure 4. A picture of the device used to perform the pulse injection experiments. The dead volume of the injection device is highlighted. This volume can be minimized through careful design of the device¹.

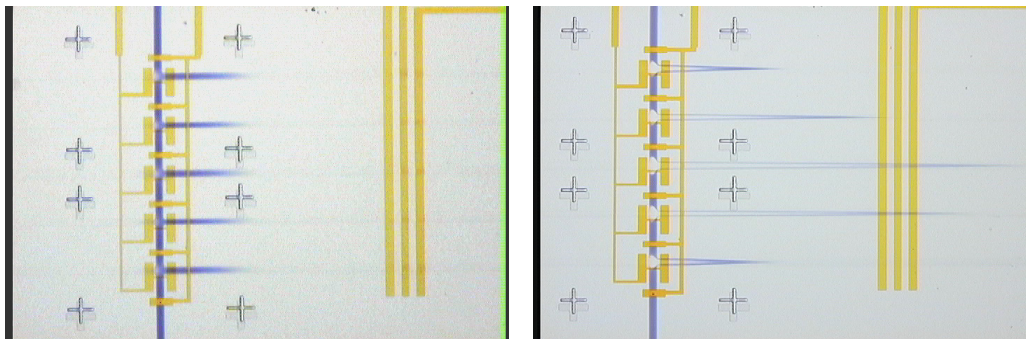


Figure 5. Pulse injection results for 100 μm wide channels. As can be seen, Poiseuille flow is developed in the channels via peristaltic pumping¹.

The experimental results verify the simulation as expected. Through cross injection, accurate amounts of fluid can be measured and injected into the flow channel. The volume of injected fluid is controlled through the inherent geometry of the flow channel. The dead volume which occurs due to the valves, shown in Figure 3, can be minimized by placing the valves closer to the cross injection

¹ Photos courtesy of Mr. Carl Hansen

channel. Although it is impossible to eliminate the dead volume entirely, it can be calibrated for in the experiment.

As with most MSL chips, the driving force behind fluid flow is not applied pressure. Instead fluid is pumped by using a series of valves which creates a peristaltic pump. This method was modeled since the pumping is different than standard pressure driven flow. The pumping was modeled as a series of pressure pulses in a given time, similar to a square wave. However, due to the elasticity of the PDMS, the more accurate description is that of a modified square wave. For modeling purposes the modified square waveform was chosen. Figure 6 depicts simulation still shots of fluid under both pressure driven flow and peristaltic pumping. It can be seen that the fluid develops the standard Gaussian profile associated with Poiseuille flow. Therefore it is reasonable to assume that the peristaltic pump provides a uniform pressure if the pump frequency is large enough. However, since the pressure field is not applied continuously, the flow dispersion is affected to a greater degree by diffusion. The dispersion was measured for both situations. The results can be seen in Figure 6 for both flow types. As expected the dispersion for the peristaltic driven channel was greater than the pressure driven flow; however, both maintain the Poiseuille flow dynamic.

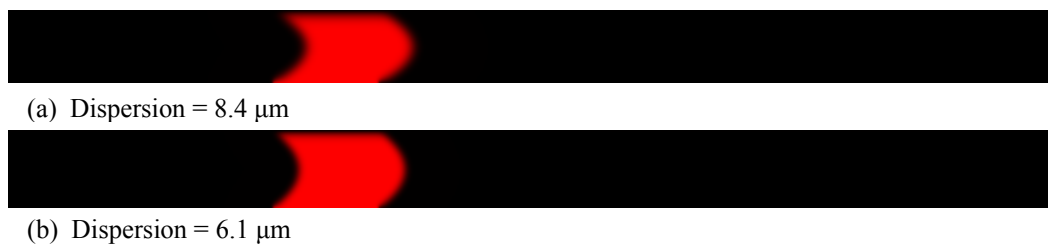


Figure 6. Simulation results of flow induced via (a) peristaltic pumping and (b) pressure driven flow in an elastomer flow channel. The flow profile develops the parabolic shape typically encountered in Poiseuille flow. The dispersion is indicated for each flow type.

Microfluidic Diode (One-Way Valve)

The microfluidic diode is analogous to an electronic diode in function.

Where an electronic diode prevents current flow in one direction, the fluidic diode prevents fluid flow in a certain direction and serves the function of a rectifier.

Although there have been other attempts at making valves which limit flow in one direction, they almost always involve a very complex fabrication procedure in which many steps are needed to produce the device [20-25]. The fluidic diode is a single-layer, planar device that can be fully integrated with standard MSL technology.

The applications for such a device are many and varied. One of the most important uses of the device is to prevent backflow. In many situations it is desirable to avoid a solution leaking back from where it had come. Another use is in the creation of microfluidic logic. Once again, an analogy can be drawn from diode-diode logic in electronics. The fluidic diode can be a basic building block for logic devices such as fluidic inverters and nand/nor gates. One can also envision making pumps, pressure reservoirs, or oscillators with the fluidic diode.

The device, developed as part of this work, is based upon a mechanical effect in which a flap of PDMS seals to a channel in one direction and opens in the flow direction. This is very similar to a swinging door which has a door jam on one side but is free to swing in the other direction. The device is illustrated in Figure 7. It is important to note that the flap hangs from the top of the wider channel. This channel is also higher than the other channel, so that the flap can completely seal against the small channel. The properties of the diode can be adjusted by changing the flap thickness as well as the ratio of channel heights. For most applications the channel height ratio needs to be at least 2:1 and the ratio between the large channel height and the flap thickness should be 3:1 minimum. A detailed fabrication process for the fluidic diode is listed in Appendix B – Fluidic Diode.

One potential problem that can occur during fabrication involves the deformation of the flap. Since the flap is quite tall and narrow, when the elastomeric device is removed from the mold, the flap is placed under substantial tension. Once free from the mold, the flap can snap back and sometimes, depending upon the aspect ratio, the flap can roll up onto itself. This causes a partial blockage within the channel which limits, but does not prevent flow. A device in which the flap is rolled upon itself is shown in Figure 8 (a) and (b) illustrates the flap in its unrolled state.

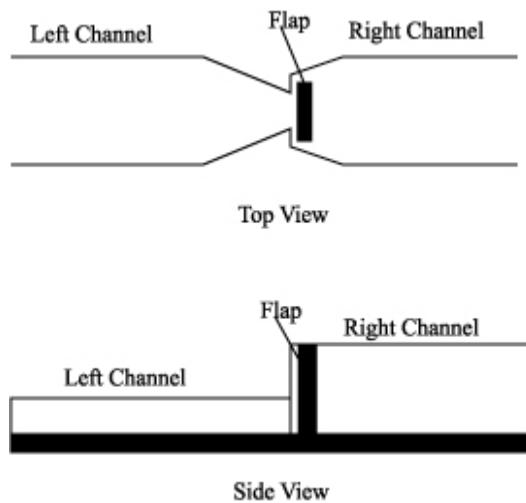


Figure 7. Microfluidic diode illustration. The flow from the right direction is stopped as the flap presses against the orifice of the left channel. Flow from the left is allowed to flow since the flap is unobstructed in the right channel.

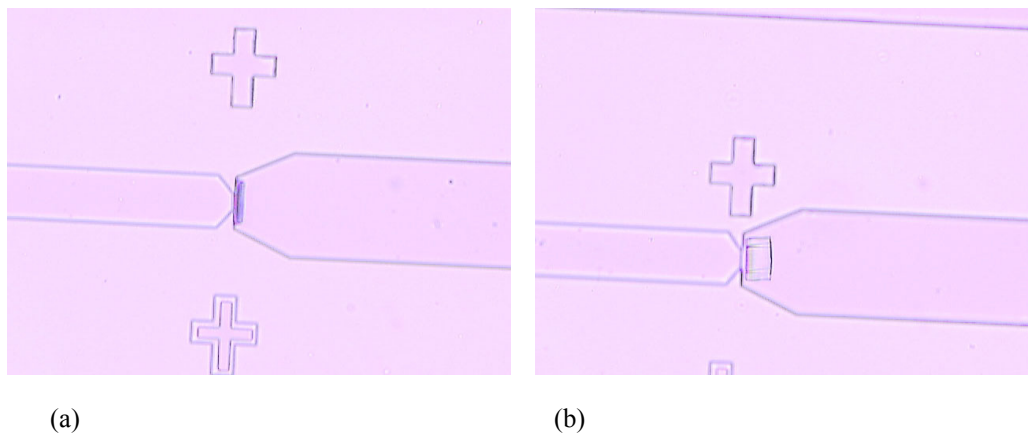


Figure 8. (a) Fluidic diode with the flap rolled upon itself. (b) The flap was unrolled into the channel.

By changing the flap parameters, one can adjust the turn on pressure of the diode as well as the response time of the flap. The stiffer the flap, the faster it will respond when the flow direction is reversed. Devices with different geometries were characterized by applying regulated pressure to the flow direction and then

the non-flow direction. Each device was tested with 100 μM fluorescein with an inverted microscope and mercury lamp. A picture of the tested device appears in Figure 9. The device shown has two microfluidic diodes which are facing in opposing directions. The fluorescein enabled the easy determination of when the fluid started flowing as well as if there was any leakage in the non-flow direction. Table 1 lists turn on pressure and reverse standoff pressure for some devices. As can be seen the reverse standoff is quite high and generally the sample became unsealed before the device failed.

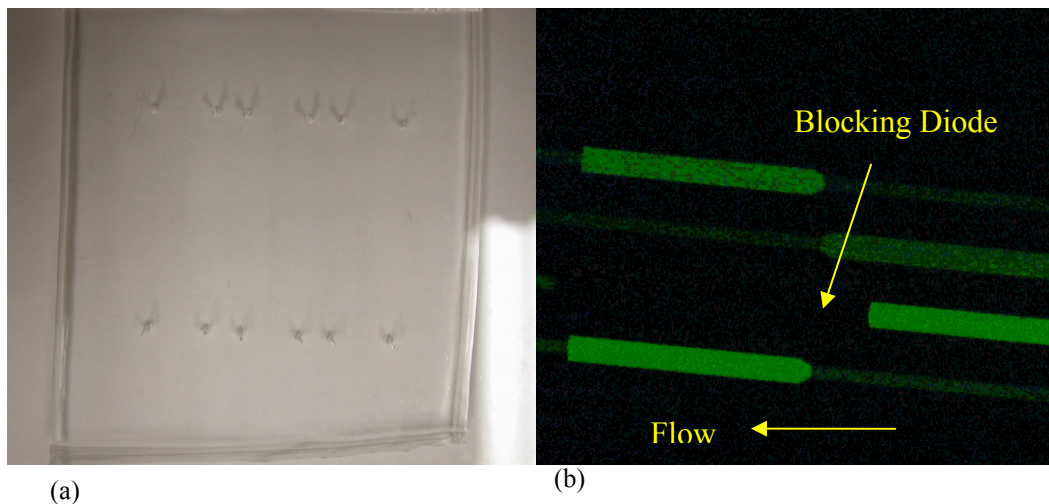


Figure 9. (a) Microfluidic diode device with 4 pairs of two opposing diodes. (b) Diodes tested with 100 μM fluorescein. The fluorescein flows in the direction of flow for the bottom diode and does not flow in the opposing device. The channel does eventually fill due to dead volume filling, but fluid does not leak past the diode.

Table 1. Microfluidic diode performance as a function of geometry.

| Aspect ratio (height/thickness) | Turn on (PSI) | Reverse standoff (PSI) |
|------------------------------------|---------------|------------------------|
| 2:1 | 8.3 | 25 |
| 3:1 | 5.5 | 25 |
| 4:1 | 3.2 | 25 |

Since the fluidic diode is an obvious analog of the electronic diode, it was of interest to try and determine the analogy of an i-v curve. Since in microfluidics pressure is equivalent to voltage, much of the data had already been acquired. However, the fluidic equivalent to current is flow which is very difficult to measure in a microfluidic system. The flow rate can be calculated as described above given the pressure drop and the fluidic resistance of the channel; however, experimental data was needed to verify the calculations. In order to determine an approximate flow rate, fluorescent beads were used to track the flow inside the channel. Since the exact length of the channel was known, the speed of the bead could be determined by measuring the distance traveled in a certain time period. Through this method an Q_1 -P (flow rate vs. pressure) curve was generated and is shown in Figure 10. It can be seen that the higher aspect ratio channels achieve slightly larger flow rates for a given pressure. This can be attributed to the dependence of fluidic resistance on channel geometry as described in Eq. 2.5. The dislocation that occurs in each of the curves at its turn-on is due to the inability to sample the flow velocity at very small intervals of pressure. The pressure regulator used for testing only allowed .1 psi accuracy. With a more accurate pressure regulator and a faster video capture mechanism, the curves could be filled in with greater detail.

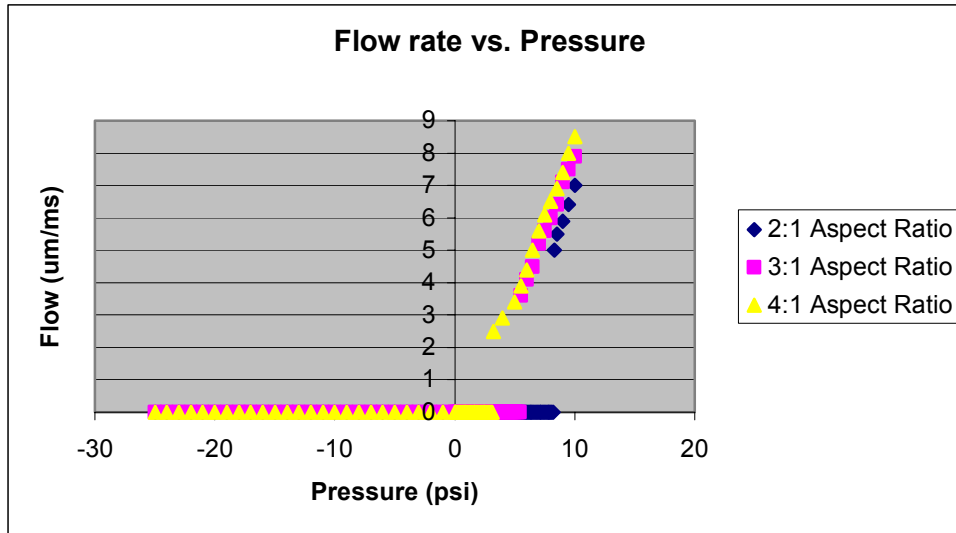


Figure 10. A flow rate vs. pressure curve for the three fluidic diode geometries described above. This curve is analogous to an electronic diode's I-V curve.

Microfluidic Amplifier

Another very useful device for MSL technology is a microfluidic pressure amplifier. A pressure amplifier would allow a flow channel with a higher pressure to be closed by a control channel with a lower pressure. This would allow higher flow rates without increasing the total pressure required to run a multilayer chip.

The fluidic amplifier is based upon a very simple mechanical principle. Since pressure is defined as

$$P = \frac{F}{A} \quad 2.20$$

where F is the applied force and A is the area, one can create a device in which the force acting on each channel is identical. This is accomplished by creating a mechanical linkage between the two channels as shown in Figure 11.

Pressure Amplifier Device Structure

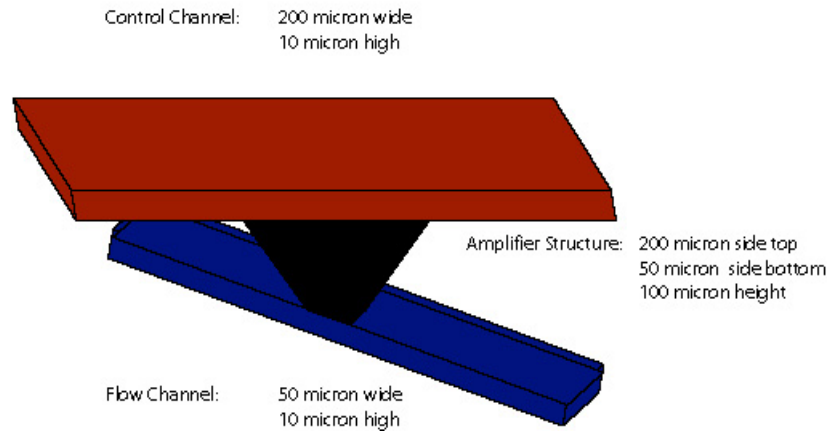


Figure 11. Microfluidic pressure amplifier schematic.

If the control channel area is larger than the flow channel and the forces are equal, the control channel pressure needed to close the flow channel is less by a factor of the ratio of the areas, i.e.,

$$\begin{aligned}
 F_{control} &= F_{flow} \\
 A_{control} &> A_{flow} \\
 F_{control} &= P_{control} A_{control} = P_{flow} A_{flow} \\
 P_{control} &= P_{flow} \frac{A_{flow}}{A_{control}}
 \end{aligned}
 \tag{2.21}$$

The mechanical linkage comes from a truncated pyramid which is inserted in between the flow and control layers. A bulk micromachined mold and soft lithography were used to create the truncated pyramid. A 110 silicon wafer with 10000Å of silicon dioxide was patterned using photolithography and then etched in HF. The photoresist was removed with acetone and isopropyl alcohol. The

wafer was then etched at 80°C in KOH to form the pyramid structures in the silicon for one hour. This technique produced truncated pyramids which were 200µm square on the top and 50µm square on the bottom. The flow and control molds were standard soft lithography molds which matched the pyramid dimensions, i.e., 200µm control channel and 50µm flow channel. For a detailed fabrication procedure see Appendix B – Microfluidic Amplifier.

Originally the pyramid was formed out of PDMS; however, since PDMS is an elastomer, a true mechanical linkage could not be established. Instead of seeing gain, the amplifier typically showed a loss. This was due to non uniform force transfer from the control layer to the flow layer. The PDMS pyramid bent and collapsed in on itself instead of transferring the full force of the control channel to the flow channel. However, even though the amplifier had no gain it was still able to close a channel as can be seen in Figure 12.

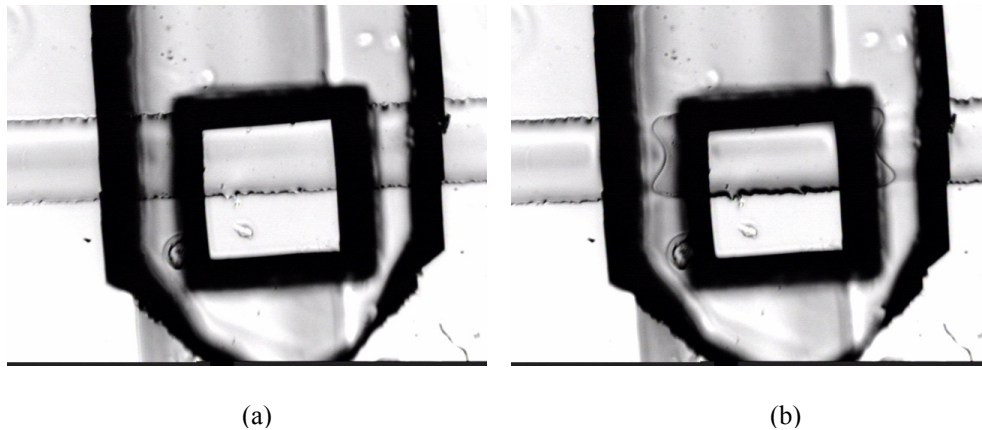


Figure 12. Picture of the amplifier structure taken with an optical microscope shows (a) the valve open and (b) the valve closed. The pressure necessary for sealing was approximately the same as without the amplifier.

Another attempt was made to perfect the amplifier. Since PDMS obviously would not work, another suitable material was needed. The best choice was SU8. Although it is normally used to make photoresist molds, it is much stiffer than PDMS but is also optically transparent. So a thin membrane with the truncated pyramids was made by spinning SU8-2050 on the silicon mold. The membrane was then sandwiched between the standard flow and control layers and sealed. Unfortunately the PDMS did not seal well to the SU8 and the device was not very robust. However, upon testing the device did show some amplification. Although the gain was not the factor of four expected from the design it was greater than one. Most likely the problem was that the pyramid was not fully coupling between the channels since the SU8 layer was not bonded well to the PDMS layers. One solution to the problem would be to find a suitable adhesion promoter for PDMS and SU8.

PDMS Etching

Another very useful technique developed to extend current MSL techniques was a plasma etching recipe for PDMS. For future applications, it may be necessary to build MSL devices with multiple flow layers. These layers would need to be connected through some type of via as is typically done in integrated circuit design. Etching allows for vias to be created after the molding process has occurred. Etching also provides a technique for doing surface patterning onto a PDMS layer.

The etch recipe developed consists of a non-directional plasma etch which uses O₂ and a blend of O₂/CF₄ process gasses. The process pressure is between

200 and 300 mTorr. The O₂ flow rate is 20 sccm and the O₂/CF₄ flow rate is 60 sccm. The etch is performed in a Tegal Plasmaline with a forward power of 200 W. The etch rate achieved in PDMS is between .5 to 1 μm per minute.

Unfortunately since the etcher is a non-directional DC system, large aspect ratios are difficult to achieve. Patterned aluminum is used to mask the PDMS, since PDMS is incompatible with most standard photoresist. Aluminum foil can easily be patterned through photolithography and etched to yield excellent proximity masks for PDMS.

Electrostatic Valves

A substantial amount of effort was placed into making electrostatic valves so that a pneumatic actuation would no longer be necessary. Electrostatic valves would simplify designs by allowing flow channels to be closed without a control channel. The original design consisted of patterning aluminized mylar and bonding it to PDMS membranes. The total device thickness was on the order of 50 μm. With one side of the flow membrane maintained at ground potential, the channel could be closed by applying a large voltage across the adjacent mylar pad. For channels around 10 μm high, 100V was needed to close an empty channel. If a pressure or fluid was applied to the channel, the voltage increased dramatically. Another major problem encountered was that of ionic solutions. Since the valve was dependent upon Coulomb force, an ionic solution created a path for charge to flow and thus prevented the valve from closing. After realizing that the practicality of the electrostatic valve was somewhat limited, the project was

abandoned in order to pursue other ventures, such as optoelectronic integration,
with more fervor.

Chapter 3 – Early Integration: CMOS Imagers and Spectroscopy

Over the past few years, the use of replication molding for the definition of microfluidic systems in elastomers has allowed the rapid development of compact analysis systems useful for chemical sensing and biological diagnostics. For example, fluorescently activated cell sorters [13] based on pumps, valves and channels defined in RTV silicone elastomers have demonstrated excellent throughput and sorting accuracy. These have been fabricated inexpensively into very small and robust microfluidic devices. Chemical surface pretreatment of specific areas within a flow channel has led to the possibility of developing very compact disease diagnostic chips, and even single molecule sizing systems can be built from elastomeric flow channels [14].

In all of these applications, the overall size of the analysis system is typically limited by the dimensions of the optical excitation and detection components, and miniaturization of the read-out optics is therefore very desirable. However, miniaturization of grating-based spectrometer geometries ultimately is limited by a reduction of the spectral resolution, which can be predicted from the optical path-lengths between the grating and the detection slit. For example, multi-wavelength 4 mm by 12 mm spectrometers operating at 1500 nm typically yield a measured spectral resolution of approximately 1 nm. This compromise between resolution, insertion losses and size has in the past limited the minimum size of such optical analysis systems. Much better spectral performance can be

obtained by using dielectric filters, which can be directly deposited onto detector arrays to form multi-wavelength detector arrays. Such filtering has in the past been used for monolithic hyper-spectral imaging applications. Filtered detector arrays offer an inherent opportunity for the miniaturization of spectroscopic instruments in microfluidic applications, with the additional opportunity of obtaining low-resolution “lens-less” images of the contents in the flow channel. CMOS imagers were chosen for their ease of use and commercial availability. Imager elements based on CMOS technology also offer compatibility with other CMOS processes such as VLSI for integrating onboard signal processing.

One of the most important advantages of using elastomeric flow channels is the inherent transparency of the elastomer material in the visible wavelength range. Many semiconductor based microfluidic structures previously proposed have suffered from the inability to perform optical analysis of the device’s contents in the visible and near-UV spectral ranges. Due to the absorption edge of silicon, for example, optical measurements in flow channels defined by this material are typically limited to the infrared range and visible/UV spectroscopy is virtually impossible to perform without using very elaborate geometries. For applications such as biochemistry, this poses a severe limitation since many absorption and fluorescence experiments are based on visible/UV fluorescent dyes. Silicone elastomers circumvent this problem since they are optically transparent and have similar UV absorption characteristics to those of glass. This property enables the easy integration of elastomer microfluidic devices with standard optoelectronic sources and detectors. Moreover, silicone elastomers are

simple to integrate on top of already fully fabricated detector arrays, forming a hermetic seal to the passivation layer of the detector arrays.

Miniaturization of absorption spectrometers will advance rapidly over the next few years, due to development of short wavelength LED's and faster computer interconnects, as well as the development of inexpensive and high-quality CMOS imaging arrays.

CMOS Absorption Spectroscopy

The external optical excitation and read-out equipment setup used in the experiments described here include a 588 nm light emitting diode and a CMOS camera chip. One key difference between the measurement system and more conventional cell-sorting systems is that no lenses were used for imaging. This is a very simple approach to reducing the size of a spectroscopic imaging system and it eliminates the need for focusing optics by placing the microfluidic devices directly onto the imaging detector array. This detector can consist of silicon-based avalanche photodiodes (APDs), charge coupled devices (CCDs), or CMOS integrated p-n diode sensors. All of these devices are commercially available at reasonable costs. CCD arrays, although in general more sensitive, suffer from the need to read out the entire image information in order to determine intensity information from the pixels underneath the flow channels. Avalanche photodiodes typically require larger areas, and thus significantly reduce the resolution of the imaging system. CMOS imagers, on the other hand, offer direct control over individual pixels, and, since most of the area of the image array is typically not

used, can provide much faster response times and long integration times.

Although the lateral resolution of these imagers cannot match that of an optical microscope, it is suitable for most visible spectroscopy experiments on larger objects. The highest resolution of such a proximity imaging system is determined by the pixel size on the imaging array, and can be less than 10 microns. The sensitivity of the imaging system is in turn dependent on the active area of the pixel, as well as leakage currents in the pixels. Other factors that determine the performance of an imaging detector array in a spectrometer application are its sensitivity and dynamic range. The sensitivity becomes extremely important when examining picoliter volumes with a correspondingly small optical interaction length.

Here a CMOS imaging array was chosen as the sensor of the spectroscopic measurement system. This choice was based on the ease of directly addressing individual pixels in the array, and the opportunity for changing the integration time per pixel for more sensitive analysis. Figure 13 and Figure 14 show the geometry used for our spectroscopic measurements. The light source was a 588 nm AlInGaP light emitting diode, placed above the flow channels, which in turn were directly placed on the image array.

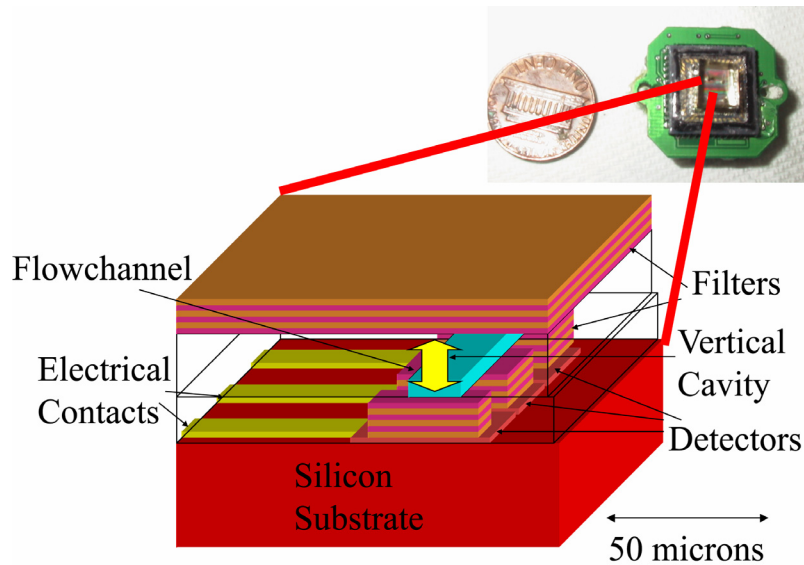


Figure 13. Miniaturization of a spectroscopic measurement system by use of a commercial CMOS imager.

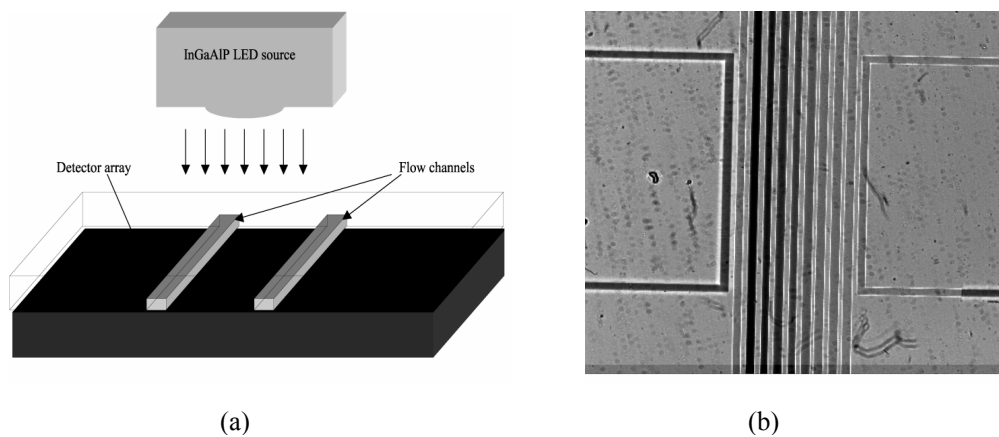


Figure 14. (a) A schematic illustration of how the absorption spectroscopy is performed. (b) A PDMS microfluidic chip imaged by the APS CMOS imager. The light source is a 588 nm λ_{max} AlInGaP LED and the channels contain 7.5 mM to 30 μ M bromophenol blue solutions. The far left channel is empty and the far right channel contains water for reference. This is an 8 bit image which is considerably less than the 12 bit resolution of the imager.

Since the typical size of an elastomer microfluidic channel is on the order of 50 to 250 microns wide by 10 to 20 microns deep, the absorption path length is

quite small compared to more conventional cuvette-based absorption spectrometers with interaction lengths 100-1000 times larger. According to the Beer-Lambert law, the absorbance A is proportional to the concentration of the absorbing material c and the absorption pathlength l , so that

$$A = \epsilon cl \quad 3.1$$

where ϵ is the molar absorption constant or molar absorptivity. Thus, the difference in the expected detected intensity of a channel filled with reagent versus a channel filled with water is very small for dilute solutions. Therefore the higher the sensitivity of the detectors in the sensor array, the greater the concentration range that can be detected.

The first absorption experiment was performed using a ten-bit resolution black and white CMOS imager provided by NASA's Jet Propulsion Laboratory. This imager has a typical pixel size of 12 μm , a dynamic range > 65 dB, and a responsivity $> 1.3 \mu\text{V}/\text{photon}$ at room temperature. The active imaging area consisted of 512x512 pixels. First, the minimum concentration of dye, which can be detected in this system, was determined. The absorptivity of various concentrations of bromophenol blue (Aldrich Chemical Company, Inc. #62625-28-9) were then tested on a calibrated Shimadzu BioSpec 1601 spectrophotometer with solution filled into 1cm cuvettes. The molar absorption constant was then calculated and a curve fit was applied to generate the control data for a 14 μm channel. Next, a polydimethylsiloxane (PDMS) microfluidic chip consisting of eleven 100 μm wide by 14 μm deep channels spaced 100 μm apart was placed directly on our CMOS imaging chip. The channels were filled with each

concentration of interest and one channel was filled with water for background measurements. Figure 14(b) shows a typical image of light transmission through the multi-channel silicone structure observed by the CMOS imager. The illumination source consisted of a Yellow AlInGaP LED with $\lambda_{\text{max}}=588$ nm and $I_0=1500$ mcd, and was optimized for the absorption peak of bromophenol blue. Although it may be difficult for the reader to distinguish the difference in the lower concentrations, the imager is more sensitive than the human eye and can readily distinguish differences down to the sub-micromolar range. The results of the experiment are summarized in Figure 15. A similar test was conducted on Orange G, excited with light at 470 nm. Measurements were made by averaging the values from 5mm long sections of the flow channel. Each of these sections has an approximate volume of 7 nL. Since the CMOS imager allows for individual sections to be analyzed, any area which might have imperfections such as air or droplet formations could be selectively removed. From these figures, it is seen that the monolithic CMOS device displays similar performance to the commercial Shimadzu spectrometer system over the conditions tested. The important advantages of the imager spectrometers over more conventional absorbance spectroscopy systems include the capability to characterize spectra from picoliter volumes, and enable the observation of many channels in parallel.

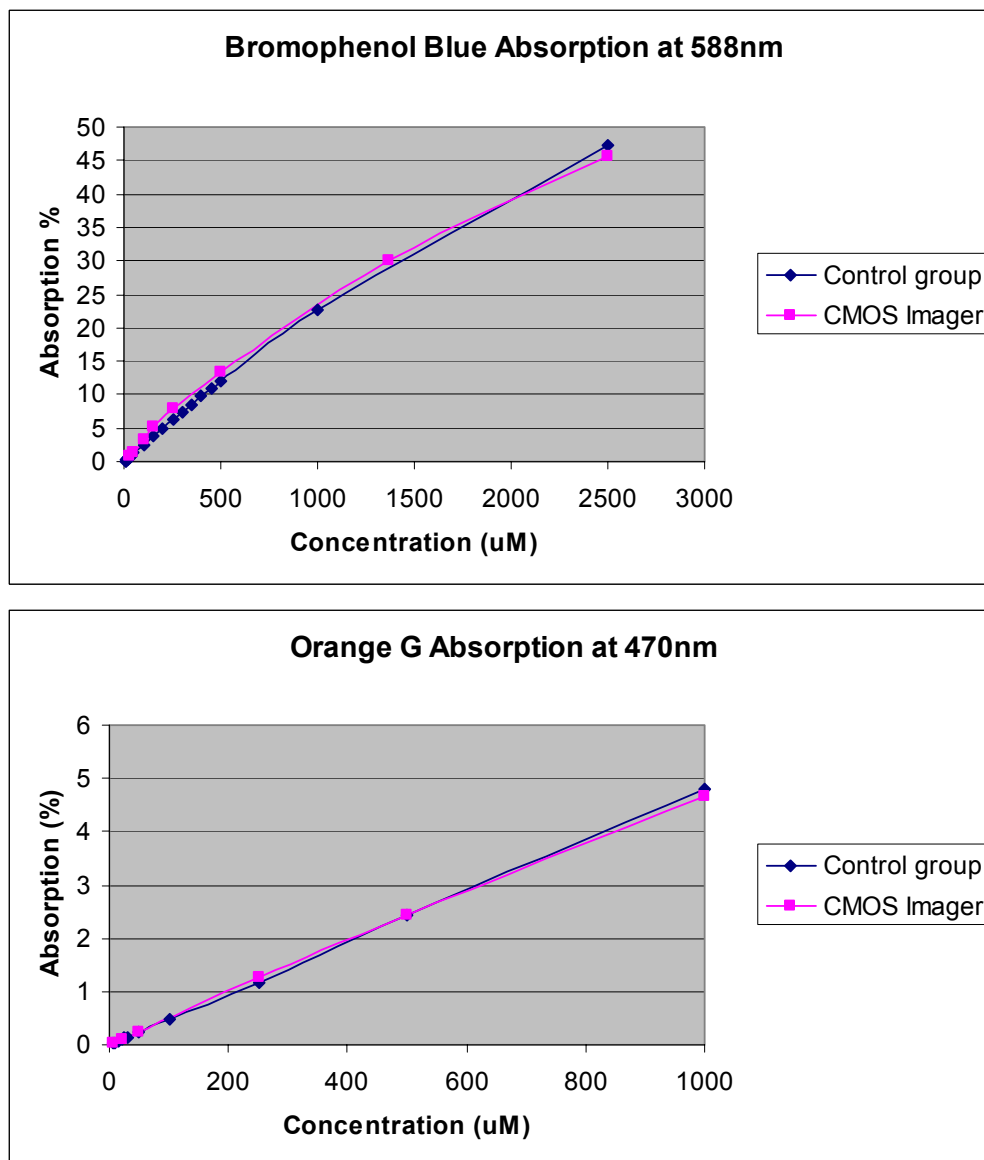


Figure 15. Absorption spectra of various Bromophenol Blue and Orange G concentrations taken with a Shimadzu spectrophotometer and the APS CMOS imager.

Broadband Absorption Spectroscopy

In the previous section, a technique was described in which the solution under test was known. This allows one to select the appropriate light source to best overlap with the absorption spectra and determine the concentration of the

solution. However, in many cases, the solution under test is not known and broadband absorption spectroscopy is needed to determine the absorption spectra of the solution. For this application, individual detectors can be filtered by using $\text{Si}_3\text{N}_4/\text{SiO}_2$ multilayer Fabry-Perot cavities (Figure 16) deposited onto the silicon detector array before definition of the fluidic structures. Filters can be deposited with a deliberate thickness variation in order to obtain a specific wavelength response for each detector in the imaging array, providing a hyper-spectral imaging array. By pumping the solution of interest over these filtered detectors and observing their response, a spectrum of the absorption or fluorescence of a very small solution volume can be obtained.

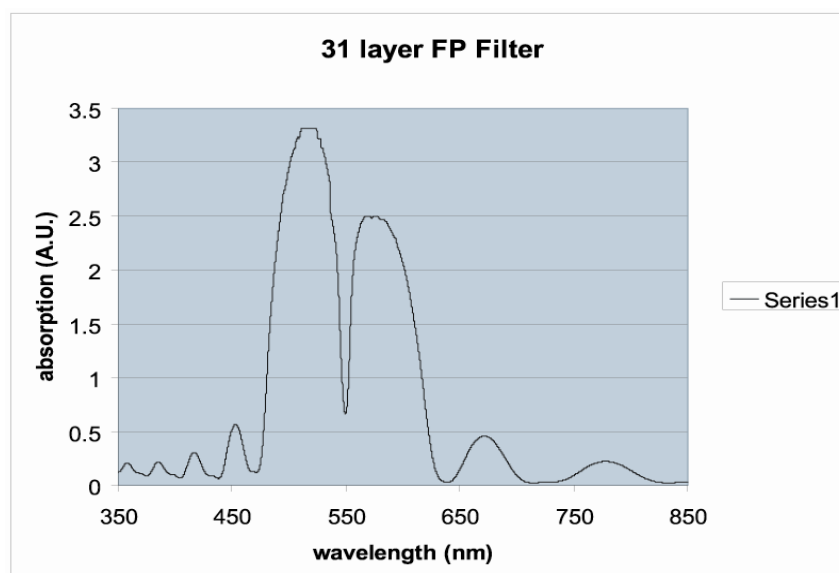


Figure 16. Absorption spectra of a 31 layer $\text{SiO}_2/\text{Si}_3\text{N}_4$ Fabry-Perot cavity.

Dielectric thin film filters have been in use for the past several decades for a multitude of applications. They offer excellent reflectivity with minimum absorption over most wavelengths of interest. However, in their simplest form,

which consists of a series of alternating $\lambda/4$ layers, they suffer from small reflectance bands and large side lobes. These problems can be corrected through material selection and careful design. Another way to solve these problems is by stacking consecutive filters on top of one another. Although this approach seems to be trivial, in reality it requires very specific design criteria. In general, multilayer dielectric stacks are modeled before they are fabricated and in most cases they are generated for a single wavelength.

In order for multiple wavelength filters to be grown on a single substrate, the thickness of the dielectric layers must be changed over the surface of the substrate. This can be accomplished in several ways, but typically involves changing the position of the substrate with respect to the source. A simple change in position can drastically affect the thickness of the deposition. Through this method, a geometrically graded multiple wavelength filter can be fabricated.

Theory

In most thin-film deposition, the consistency of the film is of critical importance. The film layers need to be homogeneous in thickness, purity, and index of refraction. Although one should be very concerned about the latter two, one can purposely take advantage of inhomogeneity in the thickness. The goal is to vary the thickness of the individual layers across the substrate, which allows for multiple wavelength filters to be fabricated on a single substrate. However, this must be done with a very precise method so that the wavelength range can be tailored to meet the specific application.

In order to understand how this can be accomplished, a quick review of magnetron sputtering physics is in order. A sputter system bombards ionized atoms into a specific target, which in turn knocks atoms off of the target. In reactive sputter systems, this is accomplished by providing a high-frequency AC field (typically 13.56 MHz) between the anode and cathode of the sputter source. This field ionizes atoms, typical an inert gas such as argon, which are used to expel atoms from the surface of the target. An inert gas is used so that no stoichiometric reactions occur between the impinging species and the species that is sputtered. The sputtered target atoms follow the magnet flux lines generated by the two permanent magnets contained within the magnetron sputter source. To generate other materials, such as SiO_2 from a Si target, another gas, i.e. oxygen, can be introduced into the system. As long as the necessary stoichiometry conditions are met, the composite material will be grown.

The most straightforward method of varying the thickness of a film layer is by changing its position with reference to the sputter source. Since the probability of a sputtered atom impinging on the sample substrate is a function of its mean free path, by changing the geometric distance between the sample and the source, the thickness can be changed. One is also able to predict the mean free path since it is a function of the system pressure and atomic diameter. With this knowledge a fairly accurate description of the sputtered layer thickness can be determined. The mean free path can be predicted as follows

$$mfp = \frac{k_B T}{\sqrt{2} p \pi d^2} \quad 3.1$$

where p is the vacuum pressure, d is the diameter of the atom, k_B is Boltzmann's constant, and T is the temperature. Since the system uses RF sputtering, the system pressure can be lower and thus the fewer collisions will take place. This allows for a more line-of-sight sputtering to occur than in a DC system, which in turn enables the geometric grading of the sample. For example, the mean free path for Si at a pressure of 3 mTorr and room temperature is approximately 2.13 cm, which is more than enough to ensure that the sample will be coated. In reactive sputtering, the chemical reaction takes place on the substrate, thus allowing SiO_2 or Si_3N_4 to be grown. Since RF sputtering is a basically a line of sight process, the point of the sample closest to the target will have the thickest film deposition and likewise the farthest point from the target will have the thinnest deposition.

Modeling

Before any fabrication occurs, the appropriate filter is modeled and its spectral response is calculated to ensure that the filter will behave as expected. Although modeling is not necessary for the simplest of filters, it is very necessary for producing filters with multiple extraction wavelengths or side lobe suppression. In general, multilayer dielectric filters can be modeled by admittance matrix theory as described by Heavens [26]. Each layer has an admittance matrix which describes its behavior. These matrices can then be multiplied together to yield the overall system matrix. A derivation of the model is provided below. For further information please see Heavens [26] or McCleod [27].

In order to derive the appropriate model, one must start by defining some terminology. Given the wave equation

$$\nabla^2 \mathbf{E} = \mu \varepsilon \left(\frac{\partial^2 \mathbf{E}}{\partial t^2} \right) + \sigma \mu \left(\frac{\partial \mathbf{E}}{\partial t} \right) \quad 3.1$$

a solution to the wave equation is a plane polarized plane harmonic wave of the form

$$\mathbf{E} = \mathcal{E} \exp \left(i \omega \left(t - \frac{x}{v} \right) \right) \quad 3.2$$

which represents a wave propagating along the x axis with velocity v . \mathcal{E} is the vector amplitude and ω is the angular frequency. For this to be solution to the wave equation

$$\frac{\omega^2}{v^2} = \omega^2 \mu \varepsilon - i \sigma \mu \omega \quad 3.3$$

With a small amount of manipulation we achieve

$$N^2 = \frac{c^2}{v^2} = \varepsilon_r \mu_r - i \left(\frac{\mu_r \sigma}{\varepsilon_r \omega_0} \right) \quad 3.4$$

This implies that N is of the form

$$N = \frac{c}{v} = n - ik \quad 3.5$$

N is the complex refractive index, n is the real part, and k is the extinction coefficient. So now our solution to the wave equation takes the form

$$\mathbf{E} = \mathcal{E} \exp \left[i \omega t - \left(\frac{2\pi N}{\lambda} \right) x \right] \quad 3.6$$

where λ is the free space wavelength ($\lambda = 2\pi c/\omega$.) From Maxwell's equations we can derive the optical admittance of a medium. For free space the admittance is given by

$$y = \sqrt{\frac{\epsilon_0}{\mu_0}} \quad 3.7$$

Since at optical frequencies μ_r is unity

$$y = Ny \quad 3.8$$

The irradiance for a wave propagating in an arbitrary direction is defined as

$$\mathbf{I} = \frac{1}{2} \text{Re}(\mathbf{E} \times \mathbf{H}^*) \quad 3.9$$

After some manipulation

$$I = \frac{1}{2} ny |\mathcal{E}|^2 \exp\left[-\left(\frac{4\pi k}{\lambda}\right)(\alpha x + \beta y + \delta z)\right] \quad 3.10$$

For a simple boundary as illustrated in Figure 17, the tangential components of the electric and magnetic fields must be continuous so for p-polarized light (TM)

$$\mathcal{E}_i \cos \varphi_0 + \mathcal{E}_r \cos \varphi_0 = \mathcal{E}_t \cos \varphi_1 \quad 3.11$$

Since $\mathcal{H} = y\mathcal{E}$

$$y_0 \mathcal{E}_i - y_0 \mathcal{E}_r = y_1 \mathcal{E}_t \quad 3.12$$

So one can then find the ratios of $\frac{\mathcal{E}_r}{\mathcal{E}_i}$ and $\frac{\mathcal{E}_t}{\mathcal{E}_i}$

$$\frac{\mathcal{E}_r}{\mathcal{E}_i} = \frac{(y_0 \cos \varphi_1 - y_1 \cos \varphi_0)}{(y_0 \cos \varphi_1 + y_1 \cos \varphi_0)} \quad 3.13$$

$$\frac{\mathcal{E}_t}{\mathcal{E}_i} = \frac{2y_0 \cos \varphi_0}{(y_0 \cos \varphi_1 + y_1 \cos \varphi_0)} \quad 3.14$$

The reflected and transmitted irradiances can then be defined as

$$R = \frac{I_r}{I_i} = \left(\frac{\mathcal{E}_r}{\mathcal{E}_i} \right)^2 \quad 3.15$$

$$T = \frac{I_t}{I_i} = \left(\frac{\mathcal{E}_t}{\mathcal{E}_i} \right)^2 \quad 3.16$$

Similar expressions can be derived for s-polarized light (TE.)

Snell's Law can be applied to calculate φ_1

$$N_0 \sin \varphi_0 = N_1 \sin \varphi_1 \quad 3.17$$

From this point on it is easiest to only concern ourselves with p-polarized light (TM waves), although s-polarized light can be described through a similar method. For simplicity one can define

$$\begin{aligned} E_i &= \mathcal{E}_i \cos \varphi_0 \\ H_i &= \mathcal{H}_i = y_0 \mathcal{E}_i = \left(\frac{y_0}{\cos \varphi_0} \right) E_i \end{aligned} \quad 3.18$$

$$\begin{aligned} E_r &= \mathcal{E}_r \cos \varphi_0 \\ H_r &= \left(\frac{y_0}{\cos \varphi_0} \right) E_r \end{aligned} \quad 3.19$$

$$\begin{aligned} E_t &= \mathcal{E}_t \cos \varphi_1 \\ H_t &= \left(\frac{y_1}{\cos \varphi_1} \right) E_t \end{aligned} \quad 3.20$$

Then one can express (a) the electric field parallel to the boundary as

$$E_i + E_r = E_t \quad 3.21$$

and (b) the magnetic field parallel to the boundary as

$$\left(\frac{y_0}{\cos \varphi_0} \right) H_i - \left(\frac{y_0}{\cos \varphi_0} \right) H_r = \left(\frac{y_1}{\cos \varphi_1} \right) H_t \quad 3.22$$

The optical admittance at oblique incidence can now be defined as

$$\eta = \frac{H}{E} \quad 3.23$$

$$\eta_p = \frac{y}{\cos \varphi}$$

The reflected and transmitted irradiances can then be defined in terms of

$$R = \left(\frac{\eta_0 - \eta_1}{\eta_0 + \eta_1} \right)^2 \quad 3.24$$

$$T = \frac{4\eta_0\eta_1}{(\eta_0 + \eta_1)^2} \quad 3.25$$

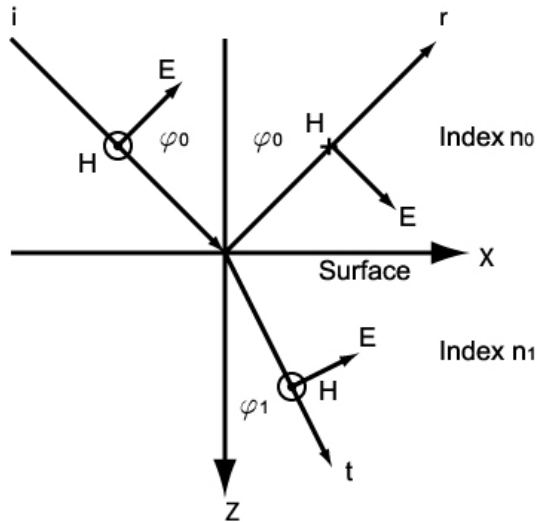


Figure 17. Convention defining the positive directions of the electric and magnetic vectors for p-polarized light

One can quickly examine a plane wave incident on a thin film as show in Figure 18. Since multiple boundaries exist, it is easiest to use the vector sum of the fields traveling the + (positive going) or – (negative going) waves.

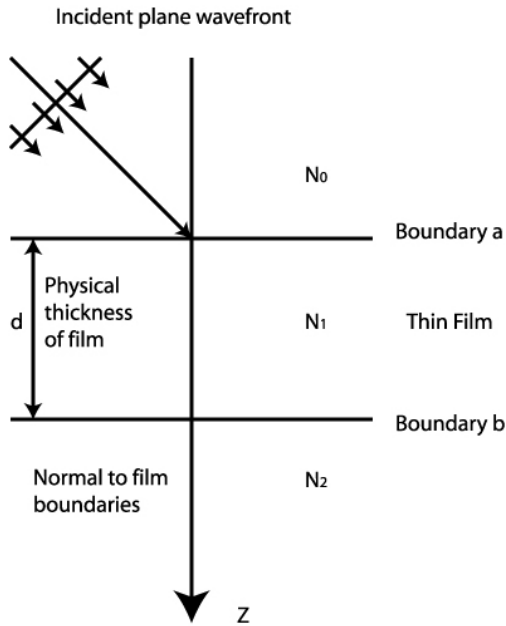


Figure 18. Illustration of the incident wavefront on a simple thin film.

At boundary **b** we have

$$\begin{aligned} E_b &= E_{1b}^+ + E_{1b}^- \\ H_b &= \eta_1 E_{1b}^+ - \eta_1 E_{1b}^- \end{aligned} \quad 3.26$$

Neglecting the common phase factors and where E_b and H_b represent the resultants; at boundary **a**

$$\begin{aligned} E_{1a}^+ &= E_{1b}^+ e^{i\delta} = \frac{1}{2} \left(\frac{H_b}{\eta_1} + E_b \right) e^{i\delta} \\ E_{1a}^- &= E_{1b}^- e^{-i\delta} = \frac{1}{2} \left(\frac{-H_b}{\eta_1} + E_b \right) e^{-i\delta} \\ H_{1a}^+ &= H_{1b}^+ e^{i\delta} = \frac{1}{2} (H_b + \eta_1 E_b) e^{i\delta} \\ H_{1a}^- &= H_{1b}^- e^{-i\delta} = \frac{1}{2} (H_b - \eta_1 E_b) e^{-i\delta} \end{aligned} \quad 3.27$$

So that

$$\begin{aligned} E_a &= E_{1a}^+ + E_{1a}^- \\ H_a &= H_{1a}^+ + H_{1a}^- \end{aligned} \quad 3.28$$

In order to correct for the phase change as the wave travels through the medium a factor δ is defined as

$$\delta = \frac{2\pi N_1 \cos \varphi_1}{\lambda} \quad 3.29$$

From the previous equations, one can express the solution in matrix form as

$$\begin{bmatrix} E_a \\ H_a \end{bmatrix} = \begin{bmatrix} \cos \delta & (i \sin \delta) / \eta_1 \\ i \eta_1 \sin \delta & \cos \delta \end{bmatrix} \begin{bmatrix} E_b \\ H_b \end{bmatrix} \quad 3.30$$

An assembly of thin films can then be characterized by applying the above method as follows

$$\begin{bmatrix} B \\ C \end{bmatrix} = \left\{ \prod_{r=1}^q \begin{bmatrix} \cos \delta_r & (i \sin \delta_r) / \eta_r \\ i \eta_r \sin \delta_r & \cos \delta_r \end{bmatrix} \right\} \begin{bmatrix} 1 \\ \eta_m \end{bmatrix} \quad 3.31$$

where the suffix m denotes the substrate or emergent medium. The reflectance, transmittance and absorptance can now be calculated where the following relationship must hold

$$\begin{aligned} 1 &= R + T + A \\ R &= \left(\frac{\eta_0 B - C}{\eta_0 B + C} \right) \left(\frac{\eta_0 B - C}{\eta_0 B + C} \right)^* \\ T &= \frac{4\eta_0 \operatorname{Re}(\eta_m)}{(\eta_0 B + C)(\eta_0 B + C)^*} \\ A &= \frac{4\eta_0 \operatorname{Re}(BC^* - \eta_m)}{(\eta_0 B + C)(\eta_0 B + C)^*} \end{aligned} \quad 3.32$$

At this time it is also useful to define Absorbance which is an easily measured quantity as

$$\text{Abs} = \log_{10} \left(\frac{1}{T} \right) \quad 3.33$$

Since the mathematical model is quite complex, it was formulated within Mathcad to perform the simulation. A similar Mathcad model is included in Appendix C. The calculated spectrum for both a high reflectivity filter and a half-wave cavity are shown in Figure 19. The reflectivity of the filter and quality of the cavity are both functions of the number of dielectric thin-film layers and the index of refraction of the material. For the spectrums in Figure 19, the materials modeled were SiO_2 and Si_3N_4 .

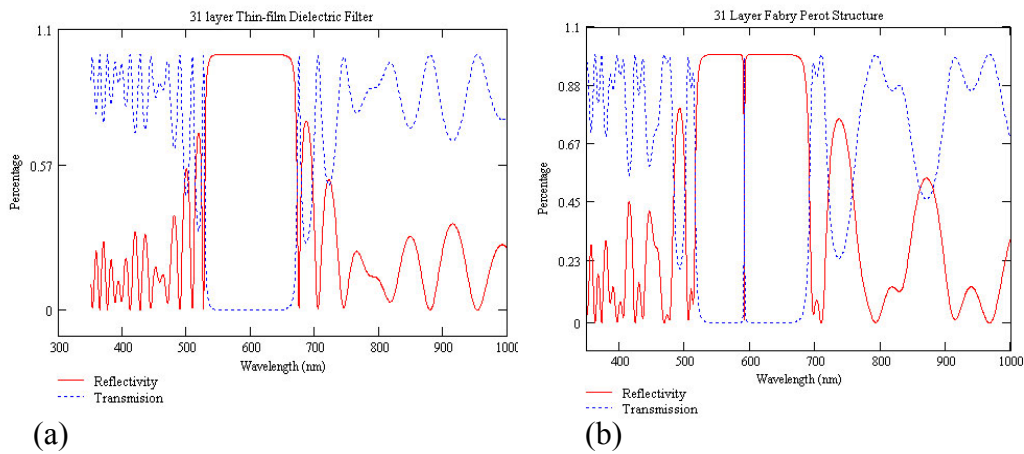


Figure 19. (a) 31 layer $\lambda/4$ dielectric thin-film reflector. (b) 31 layer $\lambda/4$ dielectric thin-film half-wave cavity.

Fabrication

The thin-film filters were grown using a toroidal magnetron source reactive sputter deposition system. The source has a 2" 99.999% purity Silicon target. The SiO_2 and Si_3N_4 films are grown by a stoichiometric process in which

O₂ or N₂ are admitted into the system, respectively. The initial plasma is started by flowing Ar into the system and increasing the pressure to 30 mTorr. After a plasma has ignited, another process gas is admitted into the system and the system pressure is regulated to 3 mTorr. The system is computer controlled and the deposition rate and film thickness are measured by a crystal monitor.

Before the actual filters were grown, the system was calibrated by growing single layer SiO₂ and Si₃N₄ films respectively on silicon substrates. These films were then patterned through photolithography and etched in a reactive ion etcher (RIE) so that the film thickness could be measured with an Alphastep 500 surface profilometer. After the thickness had been measured, each sample was placed onto a Focus ellipsometer to measure the refractive index, n , and extinction coefficient, k , of the material. For SiO₂, $n=1.47$ and $k=.00001$. For Si₃N₄, $n=2.05$ and $k=.00001$. These values indicate that the films are of high quality.

The actual filters are fabricated on glass coverslips, which have been precleaned prior to deposition. The filters consist of 23 to 41 total layers depending upon the desired reflectivity. For a 23 layer structure, the first 11 layers consist of alternating layers of Si₃N₄ and SiO₂, which are $\lambda/4$ thickness. This is then followed by a $\lambda/2$ thick layer of SiO₂. The filter is completed by growing 11 more, $\lambda/4$ thick, alternating layers of Si₃N₄ and SiO₂. This procedure produces a Fabry-Perot cavity structure which only passes a very narrow band of incident light. Due to system limitations, only one substrate can be processed at a time; however, due to the precision control of the deposition system, reproducibility is very high.

Once the appropriate wavelength has been chosen for the notch filter, a recipe is generated which includes the appropriate layer thickness and gas mixture. The recipe is easily generated via a software program that was built into the deposition system control software. After loading the sample, it must be placed in proper position to allow for the geometric grading to occur. The sample stage has X, Y, Z, and rotation, which allows for precise placement of the sample. A picture of the filter is shown in Figure 20.

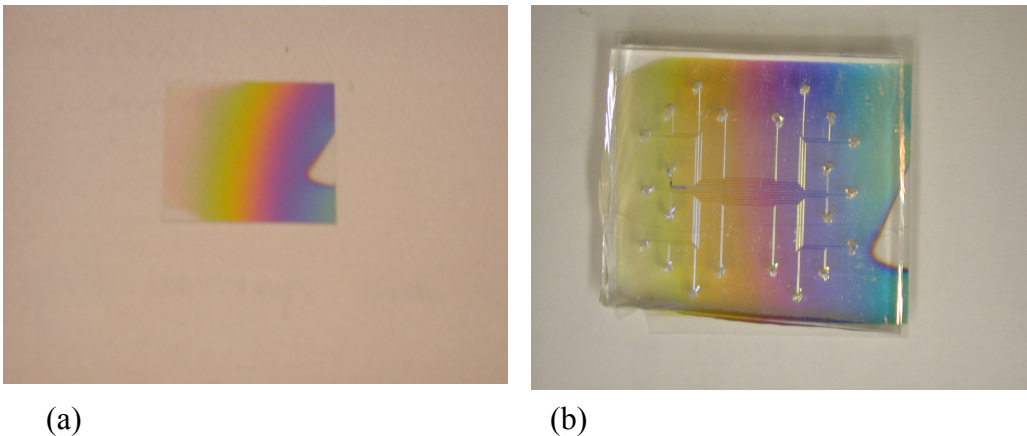


Figure 20. (a) Geometrically graded filter grown on a reactive sputter deposition system. The grading is produced by placing the sample at an angle to the sputter source. (b) Patterned filter with flow substrate sealed to the surface.

After the filter is grown, it is then patterned via photolithography to produce a 20 μm by 20 μm grid on the surface of the filter. 5000 \AA of chrome is then evaporated on to the sample. A liftoff procedure with acetone is then used to create the chrome etch mask. Once the appropriate etch mask has been placed, the sample is then etched with a reactive ion etcher (RIE.) The sample was etched with 25 sccm C_2F_6 and 5 sccm Ar at 60 W forward power for 4 hours. This allows for the unprotected areas of the filter to be removed and leave the

transparent substrate. After the RIE, the sample is finally etched in chrome etch solution to remove the protecting mask and reveal the individual filter elements.

Results and Discussion

The filter was tested via an Ocean Optics Fiber optic spectrometer so that the individual filter elements could be tested. Figure 21 illustrates a sample of the measured spectrums which were of primary interest for testing. This particular filter was designed to operate between 450 nm and 750 nm thus providing coverage for most of the visible wavelength range. It should be noted that these filters are not intended to work with white light sources. Multiple blocking filters would have to be added to the assembly in order to produce an adequate extraction from white light; however, this is possible using the same techniques described above.

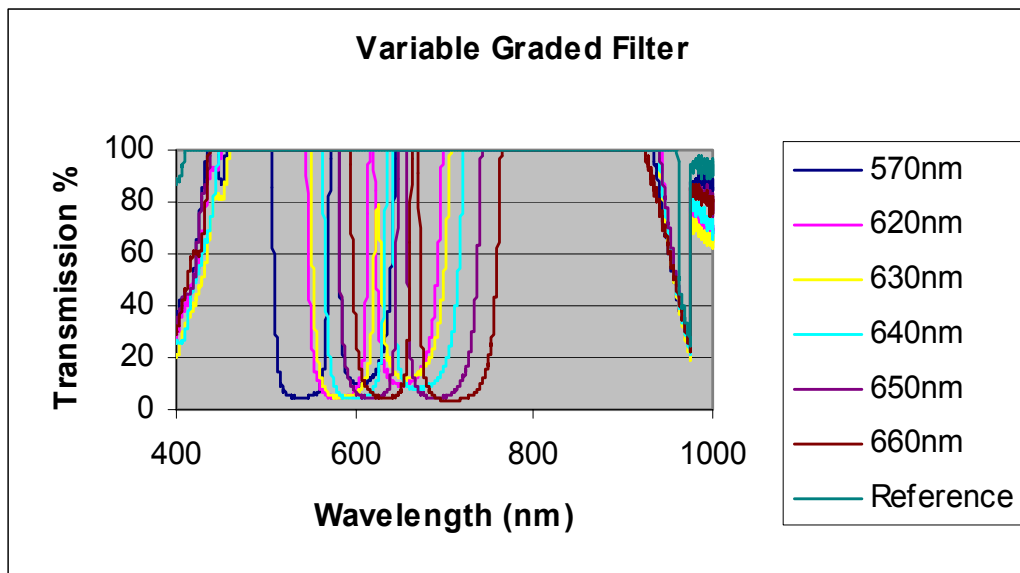


Figure 21. Transmission spectra for graded filter showing the minimum and maximum wavelength filter responses.

Figure 22 presents a spectrum using the graded filter system and a reference spectrum taken with a Shimadzu 1601 spectrophotometer. The spectrum was obtained by illuminating the microfluidic system with a series of commercial LED's and applying signal processing (discussed below) to the acquired images. Since each filter wavelength is known, and the position of each filter element with reference is known, a spectra can be generated. It should be noted that the system relies on the fact that the contents of the microfluidic channel are uniform throughout its volume. As can be seen from Figure 22, our system offers comparable performance to the commercial system.

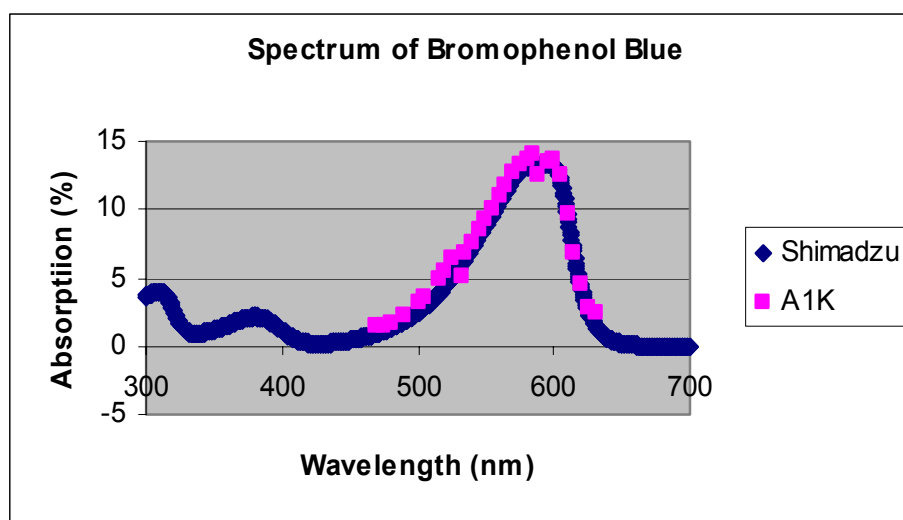


Figure 22. Spectrum of bromophenol blue taken by the CMOS imager with graded filter and taken by a Shimadzu 1601 spectrophotometer.

Fluorescence Spectroscopy

During fluorescence spectroscopy, the sample under test is excited with a light source whose wavelength is close, within 10 to 50 nm, to the emitted

fluorescent light. Typically the pump source is much brighter than the fluorescence signal, especially for experiments involving small numbers of fluorescing dye molecules, such as when performing single cell detection. Without a very efficient filter, the pump beam saturates the imager, precluding any chance of identifying the fluorescent signal. A blocking filter, which is tuned to the pump wavelength, must be placed between the microfluidic device and the imager, and should be transparent at the fluorescent wavelength.

The filter can easily be fabricated as a carefully grown dielectric thin-film mirror (Figure 23). A typical filter, deposited by reactive sputter deposition of alternate $\lambda/4$ layers of silicon dioxide and silicon nitride, is transparent at the fluorescent wavelength, and blocks over 99% of the incident pump wavelength.

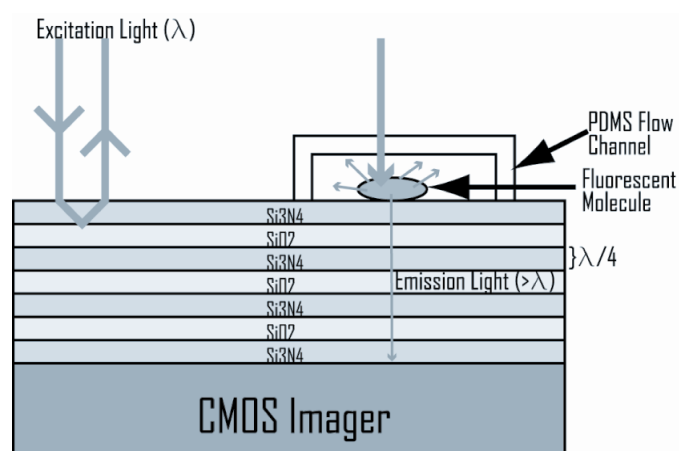


Figure 23. A quarter wavelength dielectric thin-film filter grown on the CMOS imager to block the excitation light, but pass, with minimal loss, the emission light.

Diluted fluorescein dye was used to test the performance of our monolithic fluorescence system. Figure 24 shows the absorption and emission spectra of the fluorescein dye, together with the reflectivity spectrum of the dielectric blocking

mirror. Since the mirrors and flow channel are directly deposited onto the silicon CMOS detector array, we can use the lens less contact image from this array to differentiate between concentrations of fluorescein. Spectrally resolved fluorescence measurements are also possible by slowly varying the spectral position of the reflectivity edge of the dielectric blocking mirror and measuring fluorescence intensities in different sensor pixels protected with filters with different reflectivity edges. The requirement for obtaining a high-quality fluorescence image on a miniaturized chip-based spectrometer relies on very efficient blocking of the incident excitation light by the filter whose absorption spectrum is shown in Figure 24. Otherwise the excitation light would overwhelm the fluorescing signal.

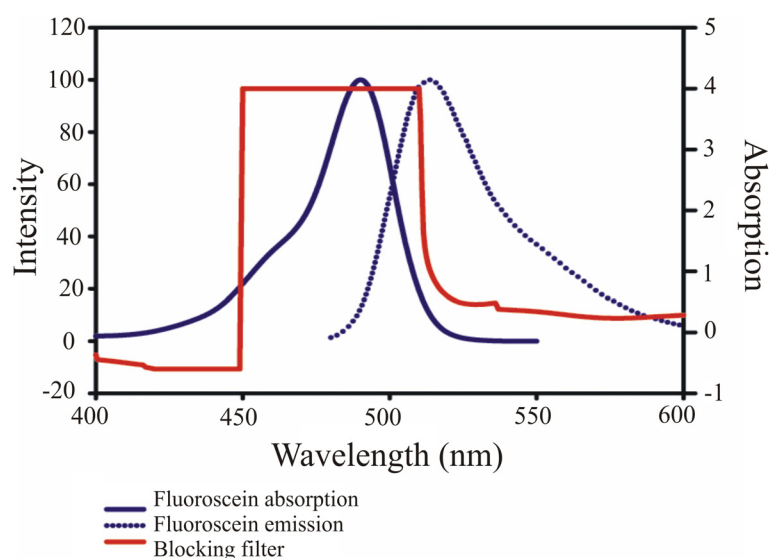


Figure 24. Fluorescent absorption and emission spectra for fluorescein. Blocking filter absorption spectrum shown in relation to second y axis. The emission peak corresponds to a region just outside the block band where the transmission is roughly 50%. This can easily be improved by constructing a narrower band-blocking filter.

Figure 25 depicts a sample image acquired with the system. In the figure, two channels were filled with different concentrations of fluorescein and illuminated with laser light. The channels were 100 μm wide and spaced 100 μm apart. The channel that resides in between the two test channels was filled with water for reference purposes. The figure illustrates that virtually all of the excitation light was blocked, and only fluorescence light was acquired by the imager. As stated previously, the reader may find it difficult to distinguish a difference between the two channels due to the loss of resolution in conversion of the imager data to picture format; however, the imager is capable of making the distinction. In fact, the concentrations of fluorescein shown in Figure 25 locally saturate the imager.

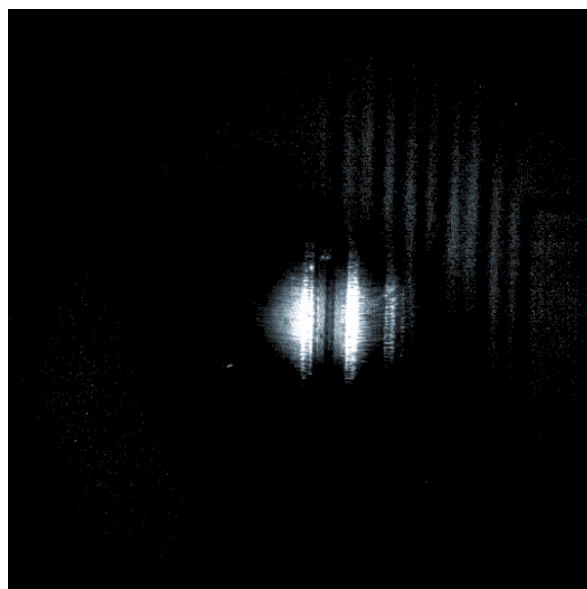


Figure 25. 170 μM and 85 μM fluorescein in 100 μm wide by 14 μm flow channels on 460 nm blocking filter illuminated by an Ar ion laser at 488 nm with no. 2 and no. .5 neutral density filters in the beam path to decrease the excitation light intensity so that the imager is not saturated.

Image Acquisition and Analysis

Although the CMOS imager is very useful for performing spectroscopy, the results shown previously are not trivial to obtain. The imager transmits information as an analog voltage which is then digitized by an analog to digital converter (ADC.) The imager does have the ability to transmit a digital data stream which provides a simpler retrieval method. However, the digital data stream is limited to 10 bit resolution which limits the achievable detection limits of the system. By using the analog mode, a full 13 bits of information is achievable and this is only limited by the DAC card installed in the capture system. The data is collected by using custom written Labview software and is saved to an ascii text file. This data can then be imported into Matlab and analyzed. For a typical graded filter absorption experiment the light source is measured with a spectrometer to obtain its spectrum. This spectrum is then used to normalize the data obtained during the experiment. Once the image is acquired, the data is manipulated so that each of the corresponding wavelengths can be obtained by geometrically normalizing the pump light to the filter characteristics. Then each specific wavelength/area is interpreted by comparing the solution under test to the specific solvent reference channel.

For other applications it is necessary to convert the data files into a bitmap image. A program was written to convert data files to both 8 bit and 16 bit bitmaps. The program was written especially so that large batches of files could be converted simultaneously since it is very easy to obtain a number of data files during a single experiment. The program code is listed in Appendix D and is very

useful for applications which have a large amount of data files that could be viewed as bitmaps.

On-chip Flow Cytometry and μ FACS

One of the most practical applications for fluorescence spectroscopy is flow cytometry and furthermore fluorescence activated cell sorting (FACS.) By using the process described above, these applications can be performed with very similar results to current standard techniques. Cell sorting in microfluidic channels was first performed by Quake's group at Caltech [13]; however, although the cell sorting was done inside a flow channel, the optical detection system involved a laser, photomultiplier tube, and the appropriate filters. The detection system was far from miniaturized. So, it seemed reasonable to test cell sorting with the integrated system described above.

In order to perform μ FACS, a suitable flow cell had to be fabricated. The flow cell consisted of a T channel in which a narrowing occurred just before the T. The nominal channel width is 50 μm which then narrows to approximately 10 μm . A picture of the cell sorter chip is shown in Figure 26. The sorting is performed by integrating valves and a pump through MSL techniques. The system is computer controlled through Labview which acquires a signal from the imager and tells a microcontroller to open or close the appropriate valves. Eventually, one could eliminate the PC control by hardwiring the microcontroller and imager together, thus simplifying the system even more. For further miniaturization the Labview computer could be replaced with a digital signal

processing (DSP) chip which would allow for a compact electronics package capable of performing both absorption and fluorescence based sorting.

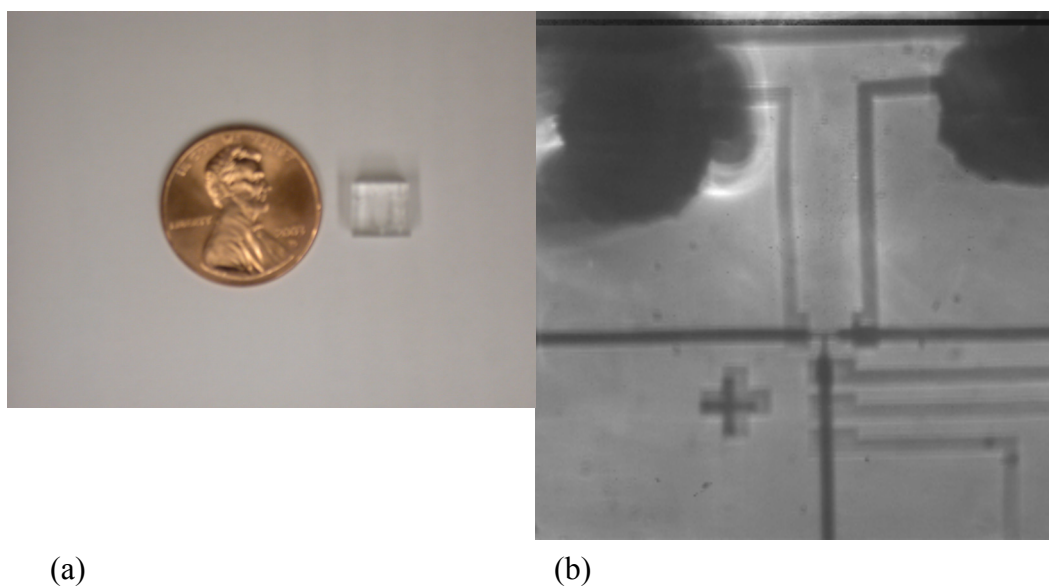


Figure 26. (a) Cell sorting chip as compared to a penny. (b) Image of cell sorter chip taken with the integrated imaging system showing the T channel, pump, and valves.

The system was tested by using 10 μm diameter fluorescently labeled beads. The beads were loaded into the channel in an aqueous buffer in very low concentration, so that statistically only one bead is interrogated at a time. A commercial LED (Stanley LED), with a peak wavelength of 505 nm, was used for illumination of the sample and a multilayer interference filter was used to extract the appropriate pump wavelength while blocking the remaining light. Another interference filter was placed on the imager to allow the fluorescence to pass while blocking any stray pump light. As a bead passed within the interrogation region, the imager signal was analyzed to determine whether it was fluorescent or not and then the appropriate sorting command was sent to the microcontroller. After the beads had been sorted a fluorescent measurement of the two sorting

chambers was made to show how accurate the sorting was. The data for the experiment is presented in Table 2 below. The sorting rate and accuracy for the first trial was relatively low, so tighter tolerances were established for the sort criteria. This improved the sorting accuracy, but unfortunately the sorting rate remained between two and three beads per second. The performance of the system could be improved by maximizing the signal-to-noise ratio of the imager. This is highly dependent upon the extraction and blocking filter performance as well as the intensity of the LED.

Table 2. Sorting accuracy for the integrated μ FACS.

| Trial | Time(s) | Beads Sorted | Beads Missed |
|-------|---------|--------------|--------------|
| 1 | 120 | $\cong 70$ | 13 |
| 2 | 300 | $\cong 150$ | 19 |
| 3 | 600 | $\cong 275$ | 26 |

Emission Sources

The monolithic integration of the microfluidic device directly on an image sensor array has been demonstrated. The next component of the system, which must be miniaturized, is the light source. In a typical visible spectrophotometer the light source is generally a tungsten or tungsten-iodine filament lamp with some models also including light emitting diodes. In a miniature spectrometer, the appropriate light source depends heavily upon the application and heat dissipation problems. The most convenient alternatives include solid-state light

emitting diodes, laser diodes, white light sources, and perhaps even the sun. For infrared analysis, the source might also be a tungsten filament lamp with a specific color filter placed directly over the microfluidic device.

Although for many applications, an array of vertical-cavity surface emitting lasers (VCSELs) could be desirable, such laser sources are very difficult to construct in the most interesting UV/visible wavelength range. Instead of using lasers, high finesse optical cavity filters can be defined on top of LED arrays to obtain filtered light sources, which can be directly placed on top of the microfluidic channel, which in turn is placed on top of a detector array, to create a fully functional on-chip visible spectrometer.

Chapter 4 – Vertical Cavity Enhancement

As previously shown, a fully integrated detection system can be created by placing the microfluidic channels directly on a CMOS imager with the appropriate thin-film filters in place. Although the system previously discussed provides adequate sensitivity for most measurements, it is path length limited and its ultimate sensitivity could be improved. To this end, an integrated vertical-cavity system was developed to enhance the system sensitivity. A schematic illustration of this system is depicted in Figure 27.

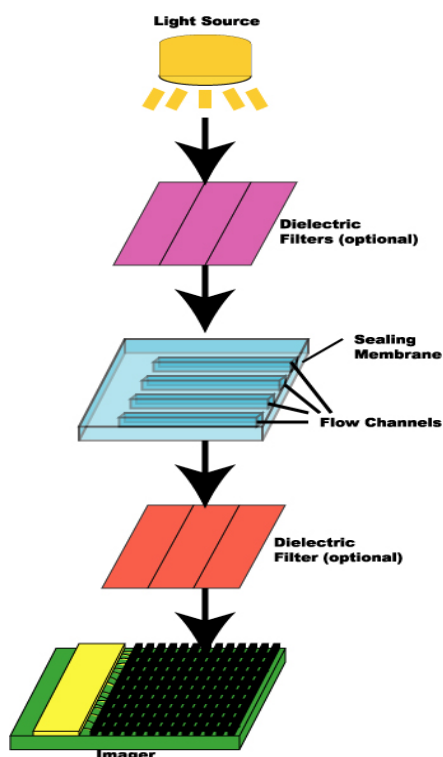


Figure 27. Schematic illustration of a vertical-cavity based analysis system.

Theory

Absorption and therefore luminescence are path-length dependent, due to the Lambert-Beer law, which states

$$A = \epsilon cb \quad 4.1$$

where A is absorption, ϵ is the molar absorptivity ($\text{L mole}^{-1}\text{cm}^{-1}$), c is the concentration (mole/L), and b is the path length (cm .) For most commercial spectrophotometers the path length is on the order of 1 cm. A typical microfluidic system has a channel height of $10\mu\text{m}$, which makes the absorption three orders of magnitude less than a commercial system. However, with the introduction of a vertical cavity structure the virtual path length can be much longer than the physical path length. This is due to the multiple passes of the light through the flow channel before exiting the cavity. However, several conditions must be met before the cavity will provide enhancement.

At this time a brief review of some of the basic concepts of cavity theory will be presented. The most straightforward cavity to analyze is the Fabry-Perot etalon. A Fabry-Perot etalon is formed by placing two reflectors a distance d apart around some medium. Each reflector has a certain reflectivity, i.e. R_1 and R_2 . For the simplest case, one can assume $R_1=R_2=R$. As a wave enters the cavity, it undergoes a phase shift proportional to the separation distance d and the index of refraction of the media. This can be written as

$$\delta = 2\pi nd \cos(\theta_i) \quad 4.2$$

where δ is the phase change (radians), n is the index of refraction of the medium, d is the separation distance, and θ_i is the angle of the incident light. For resonance to occur, the phase shift for one round trip through the cavity has to be an integral multiple of π and can be summarized as

$$\delta_{i_i} - \delta_{i_r} = m\pi \quad m = 1, 2, 3... \quad 4.3$$

A common figure of merit for a cavity is its quality factor, or Q. The Q of a cavity can be defined as follows

$$Q = \omega \frac{\text{Energy Stored}}{\text{Power Dissipated}} \quad 4.4$$

where ω is the frequency (radians.) The Q of a cavity is also related to the full-width half power points as

$$\Delta \nu_{\frac{1}{2}} = \frac{\nu}{Q} = \frac{c[\alpha - (1/d) \ln(\sqrt{R_1 R_2})]}{2\pi n} \quad 4.5$$

where c is the speed of light, α is the distributed loss constant, and ν is the cavity resonant frequency [28].

Admittance matrix theory is used to analyze the vertical cavity structure. This stems mainly from the fact that dielectric thin-film reflectors are being used in the structure and admittance matrix theory allows for straightforward modeling of the reflectors as noted above. Each layer in the structure can be described by a characteristic admittance matrix. Each of the matrices can then be multiplied together to determine the full characteristic matrix of the system. The transmission, reflection, absorption, and Q of the cavity can all be calculated from this method. For example, if the reflectors are comprised of alternating $\lambda/4$ layers of high and low index materials, the reflectance of the mirror can be easily calculated by

$$R = \frac{\left(1 - \left(\frac{n_h}{n_l} \right)^{2p} \left(\frac{n_h^2}{n_s} \right) \right)^2}{\left(1 + \left(\frac{n_h}{n_l} \right)^{2p} \left(\frac{n_h^2}{n_s} \right) \right)^2} \quad 4.6$$

where n_h and n_l are the indices of refraction of the high and low index materials respectively, n_s is the index of the substrate, and $2p+1$ is the number of layers in the stack.

One of the problems encountered when using the admittance matrix approach for characterizing the cavity structure is that concentration does not appear anywhere in the admittance matrix model. To this end, the concentration of the material inside the flow channel has to be related to the extinction coefficient k that a light wave sees as it passes through the material. This relationship can be determined by noting that the absorption is proportional to the irradiance of the light by

$$A = \log\left(\frac{I_0}{I}\right) \quad 4.7$$

where I_0 is the incident irradiance and I is the irradiance of the light after it passes through the material. In electromagnetic terms, the irradiance of the light can be written as

$$I = \frac{1}{2} n \mathcal{Y} |\mathcal{E}^2| e^{\frac{-4\pi k}{\lambda}(\alpha x + \beta y + \gamma z)} \quad 4.8$$

where \mathcal{E} is the electric field amplitude, \mathcal{Y} is the admittance of free space, λ is the wavelength, and α , β , γ are the direction cosines. (Note: direction cosine α is not to be confused with the distributed loss coefficient.) Since we are only interested in light propagation in the z direction, the equation simplifies. The points of interest are at $z = 0$, and $z = d$, the incident irradiance and the irradiance after passing through the material, respectively. By using Equations 4.7 and 4.8, one can determine the following

$$A = \log \left(e^{\frac{4\pi kd}{\lambda}} \right) \quad 4.9$$

Now, by substituting equation 1.1 for A and solving for k, one can determine the necessary correlation between concentration and extinction coefficient as follows

$$k = \left(\frac{\ln(10)}{4\pi} \right) \lambda \epsilon c \cong .1823 \lambda \epsilon c . \quad 4.10$$

Simulation

As stated previously, the admittance matrix method was used to model the physical structure. Each reflector and the flow structure have characteristic matrices associated with them. These matrices were calculated based on several variable parameters, such as flow channel height, sealing membrane thickness, concentration, and total separation distance between the reflectors. A computer model was generated to find the optimum value for these parameters.

In order to accurately model the device, it was necessary to include a suitable model for the flow channel. Although the model determines the optimized value for channel height and membrane thickness, the model must include the solution of interest that will reside within the flow channel. To this end, water was used as the primary solution for index matching purposes. However, the extinction coefficient of water was modified to resemble a lossy dye such as bromophenol blue. The absorption loss was modeled as a Gaussian curve centered around 591nm which is the absorption peak for bromophenol blue. Equation 4.10 was used to relate the extinction coefficient to the molar absorptivity, wavelength, and concentration. Through this method a more accurate determination of the

physical parameters was obtained. The simulation used an iterative method based upon initial dimensions which could be fabricated.

Along with the cavity structure a simple flow channel structure based on the same parameters minus the reflectors was calculated. The simulation was performed with Mathcad 2001i and can be found in Appendix C. Figure 28 illustrates the transmission of the vertical cavity structure and the standalone flow channel structure as a function of concentration. As can be seen, the vertical cavity structure provides great enhancement over the standalone flow structure.

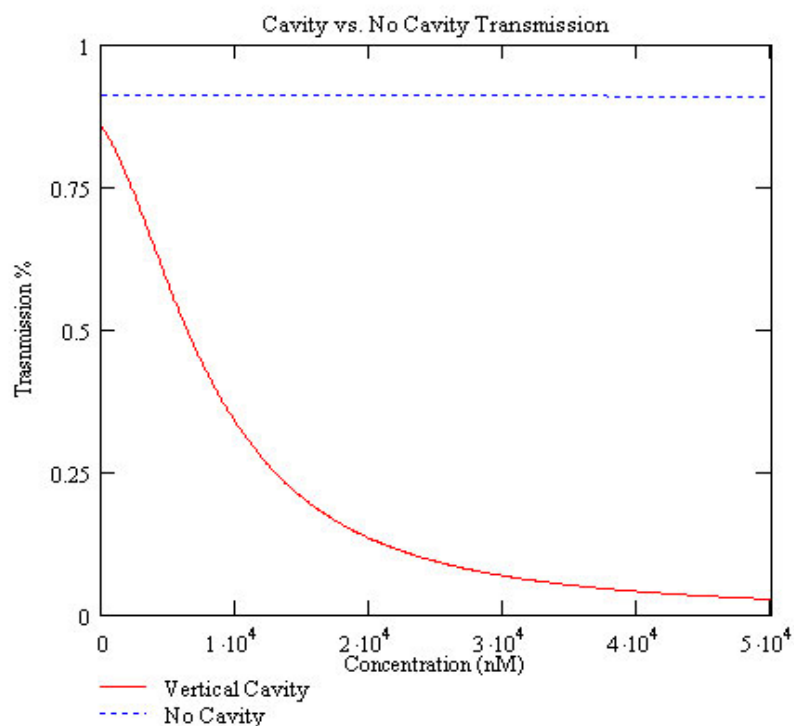


Figure 28. Simulation of the vertical cavity transmission (red) as a function of concentration at $\lambda = 591\text{nm}$. The flow structure without the cavity (blue) is shown for comparison.

Although transmission is an excellent measure of enhancement, it is often more acceptable to examine the absorbance as a function of concentration. Absorbance as described earlier is standard for performing absorption spectroscopy and for

noncavity structures is linearly proportional to the concentration. This can be seen from Figure 29. The cavity provides enhancement and thus is non-linear with concentration.

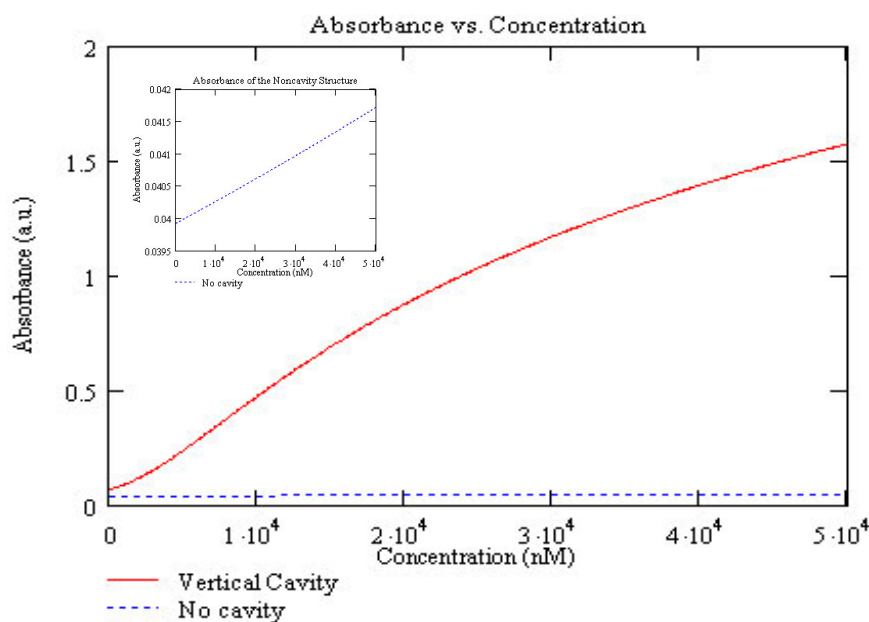


Figure 29. Absorbance of the vertical cavity structure vs. the noncavity structure. The inset shows that the noncavity absorbance is linear as expected.

The cavity's wavelength dependence is illustrated in the Figure 30. A design wavelength of $\lambda = 591$ nm was chosen to overlap with the peak absorption wavelength of bromophenol blue which was used to test the device. In addition to the peak at 591 nm another peak at a slightly longer wavelength can also be seen. This is due to the multimode nature of the cavity. The reflector separation distance is large enough to support multiple cavity modes. The enhancement of the cavity can also be calculated and optimized from the model. One can determine the enhancement for the 591 nm mode from Figure 28 and can reach a

predicted maximum of 1000. The vertical cavity structure provides enhancement for low concentrations, but the enhancement saturates as the concentration increases above 100 μM .

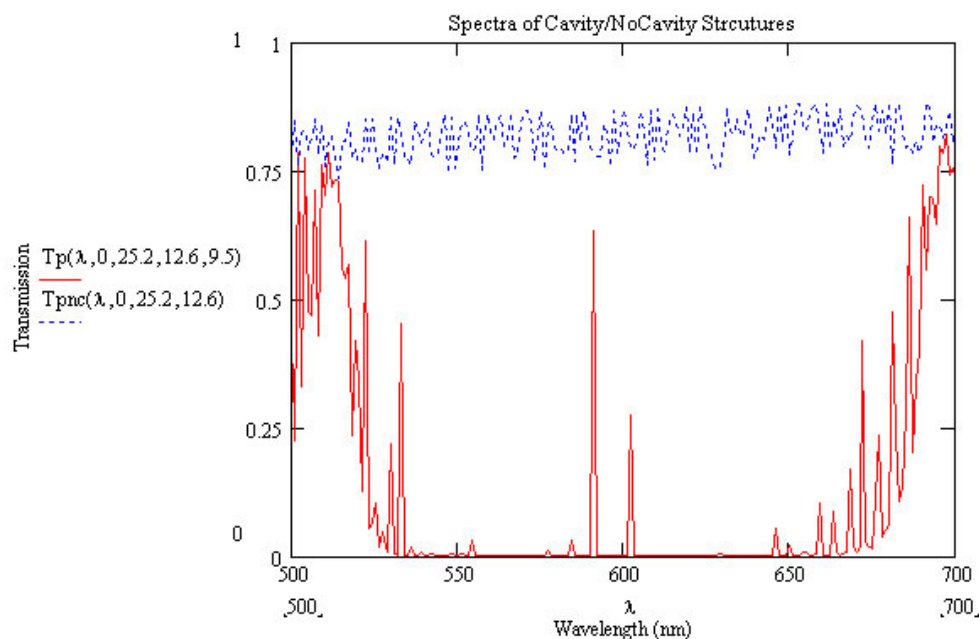


Figure 30. Simulation of the vertical cavity transmission (red) vs. the same flow structure without a cavity (blue). The cavity is designed to operate at $\lambda = 591\text{nm}$.

The simulation was extended to look at the tune-ability of the cavity. Since the cavity reflectors are separated by an elastomeric flow structure, the cavity spacing can be changed slightly by pressurizing the flow channels. Due to the nature of the device, the flow channels can not be deformed as much as in normal multilayer devices; however, a small expansion can cause a significant change in the phase matching condition of the cavity. According to Equation 4.2, the phase change is linearly proportional to the separation distance of the reflectors. This distance changes as the pressure inside the flow channel increases and the

elastomer expands. Through this technique, the cavity can be tuned so that the cavity modes change. This is shown in Figure 31 which illustrates the change in transmission peaks as a function of wavelength and change in separation distance. The separation distance change was limited to 2 μm , since this is achievable with PDMS. Although the tuning is hard to control since the pressure resolution is fairly large, the technique could be useful to overcome some fabrication tolerances.

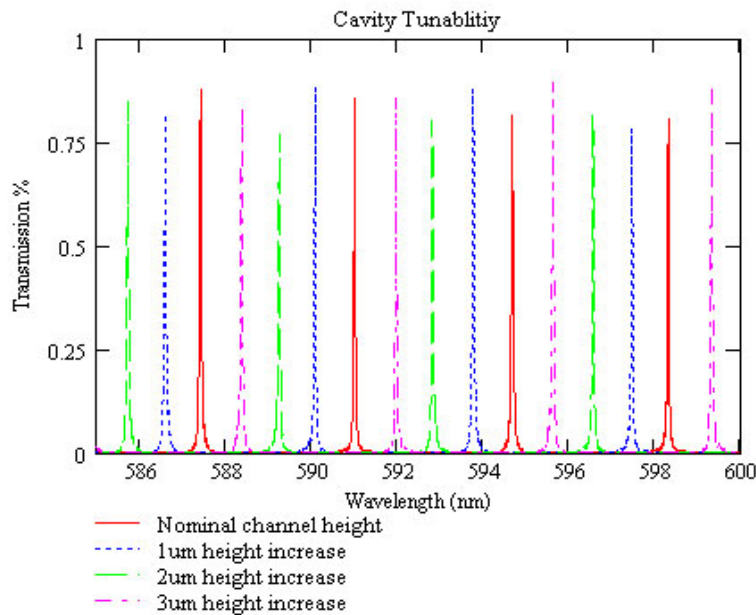


Figure 31. Variable tuning of the vertical cavity structure as a function of separation distance.

Fabrication

The device described above was fabricated by combining standard semiconductor fabrication and soft lithography. The reflectors are $\lambda/4$ dielectric thin-film stacks comprised of SiO_2 and Si_3N_4 which are deposited on No. 1 glass

microslip covers. The films are deposited by reactive sputter deposition which allows for accurate thickness and low internal stress. The reactive sputter deposition system also allows for a geometric grading of the film so that multiple wavelength cavities can be grown on a single substrate. The reflectors typically have between 15 to 20 layers depending upon the desired reflectivity. For this application, the reflectance of the mirrors is between 92% and 98%.

The microfluidic system is fabricated using multilayer soft lithography techniques. A flow channel mold is constructed using SU8-2015 spun at 4500RPM for 45 seconds with a 480RPM spread cycle for 6 seconds². The mold height was measured with an Alphastep 500 profilometer and yielded a height of 12.60 μm . The flow channel structure was then formed by spinning 20:1 GE RTV615 PDMS at 2500RPM for 60 seconds onto the mold³. This yields a flow structure of 26.4 μm . The flow structure was cured for 15 minutes at 80°C. A sealing membrane was then formed by spinning 5:1 GE RTV615 PDMS at 5400RPM for 60 seconds. The membrane thickness was measured to be 9.5 μm . The membrane was also cured for 45 minutes at 80°C. After curing the flow structure, the top reflector was placed over the flow channels and 30g of 5:1 GE RTV615 PDMS was poured on top of the reflector/flow structure assembly. This was then allowed to cure for 45 minutes at 80°C. After curing the flow system was removed and placed on top of the sealing membrane. The entire assembly was then cured at 80°C for 24 hours. An illustration of the fabrication procedure is shown in Figure 32.

² SU8 spinning was performed using a Laurel spinner model WS-400A-6NPP/LITE.

³ RTV spinning was performed using a SCS Spincoater model 6700.

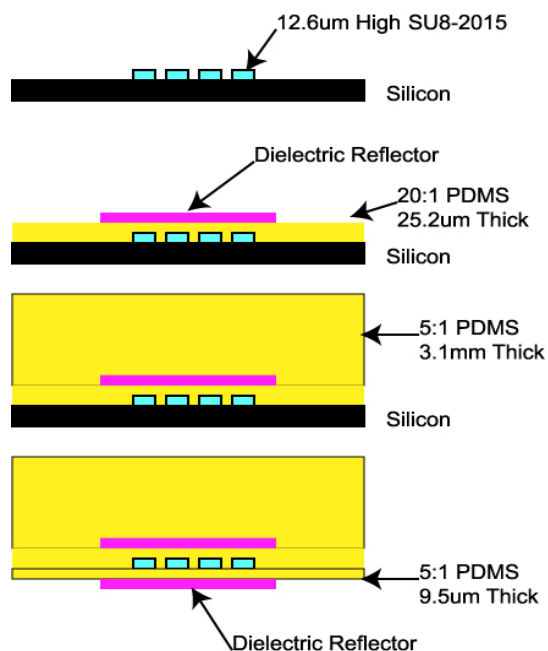


Figure 32. Fabrication procedure for creating the vertical cavity structure. Significant care must be given to the fabrication tolerances for any chance of success.

Testing

The device was tested by two distinct methods. The first method was to measure the transmission characteristics of the cavity and compare them to the simulation. The flow channels were filled with water for index matching purposes and for comparison with the simulation. Since the model takes into account the concentration of the analyte, it was necessary to establish a baseline and thus water had to be tested first. The vertical cavity structure was placed inside a Shimadzu 1601 spectrophotometer with the appropriate filter holder attachment. The cavity was compared against a baseline reference of PDMS flow cell to take into account any absorption that occurs in the material. A

transmission measurement was then performed from 350 nm to 850 nm and a spectrum was obtained. The transmission spectrum is shown in Figure 33.

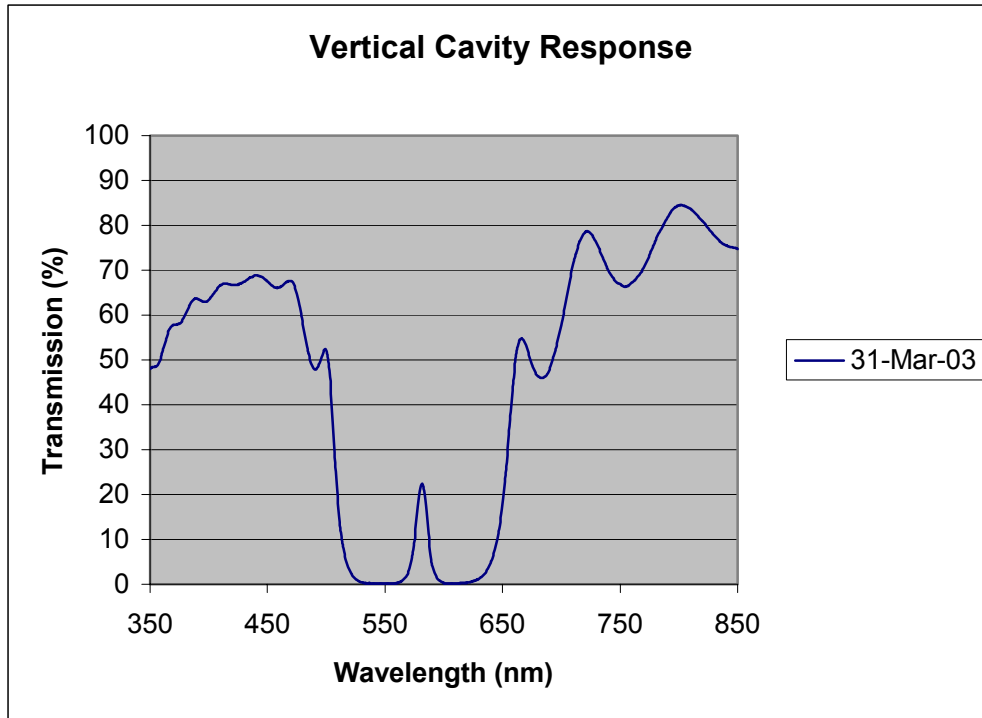


Figure 33. Measured vertical cavity spectrum for a cavity tuned to 591 nm. The FWHM of the cavity is much broader than the simulation, which is a result of many factors including lower mirror reflectivity, shift in mirror wavelength, and loss of phase matching.

The second method involved placing the vertical cavity system directly on top of a 1024x1024 pixel CMOS APS sensor. Flow channels were filled with various concentrations of bromophenol blue and water for reference. The structure was illuminated from above by a $\lambda_{\text{peak}}=588$ nm AlInGaP LED operating at 3.3V forward bias. A proximity image of the structure was taken and the channels were analyzed using image processing described earlier to determine the percentage transmission compared to the water filled channels. Multiple samples were acquired and analyzed to provide adequate statistical analysis. A similar

flow system without the integrated vertical cavity was also tested to provide comparison. A control curve was generated using a Shimadzu 1601 spectrophotometer.

Results and Discussion

Table 3 summarizes the results for the tested device, the cavityless structure, and control transmission percentage versus concentration. As can be seen, the vertical cavity structure shows significant improvement over the cavityless system in terms of determining concentration. It can also be seen that the vertical cavity system has very similar performance to the Shimadzu spectrophotometer which has a path length of 1 cm.

By testing the devices, a figure of merit which describes the enhancement can be determined. The most direct method for measuring the enhancement is to compare the lowest detectable concentration with the cavity versus without the cavity. From the experiments conducted, the greatest enhancement measured was approximately 30, although the typical value for enhancement was around 10. The system unfortunately suffers from very strict fabrication tolerances and imperfections in fabrication typically lower the enhancement. It should also be noted from Table 3 that the minimum detectable concentration of 500 nM has a relatively large error bar. This is due to the inconsistency in the measurements made for that concentration. At such low concentrations it is very difficult to distinguish the analyte under test from the water reference.

Table 3. Transmission measurements normalized for maximum transmission and path length

| | Vertical Cavity | Non-cavity | Control |
|------------------------|------------------|------------|---------|
| 500nM Bromophenol Blue | 99.985 +/- .005% | n/a | 99.987% |
| 1µM Bromophenol Blue | 99.971% | n/a | 99.974% |
| 5µM Bromophenol Blue | 99.870% | n/a | 99.872% |
| 10µM Bromophenol Blue | 99.750% | n/a | 99.744% |
| 30µM Bromophenol Blue | 99.237% | 99.239% | 99.235% |
| 50µM Bromophenol Blue | 98.725% | 98.498% | 98.729% |
| 100µM Bromophenol Blue | 97.41% | 96.689% | 97.474% |

Although only one specific substance was tested, the system can easily be created to work with any specific wavelength or a multitude of wavelengths. With this feature, miniaturized spectroscopic devices can readily be constructed. The volumes tested within the device are on the order of picoliters. Through the use of this technology multiple solutions can be tested in parallel, with a high degree of sensitivity.

A monolithic cavity enhanced microfluidic device has been developed for performing absorption spectroscopy. The integration of a vertical cavity allows for much lower concentrations of solutions to be analyzed than was previously published with our monolithic spectrometer. The vertical cavity enhancement allows for the device to compensate for some of the loss of path length that is associated with using microfluidic systems for spectroscopy. However, the system lacks the sensitivity to detect single molecules. Another technique must be developed in order to accomplish that task.

Chapter 5 – Photonic Crystal Lasers

Throughout the previous chapters, techniques for chemical and biological detection were presented which involved passing a solution of interest through a microfluidic cell and analyzing it with an external device. Although this technique provides a great deal of functionality it is somewhat limited in terms of detection limits. For instance a single protein molecule would be difficult to detect since its size is much smaller than that of the physical detector. One approach to solve this problem is to embed a sensor whose physical dimensions are similar to that of single molecules, but that could also provide useful information about the solution of interest. The planar photonic crystal laser provides a unique opportunity for solving this problem.

Photonics has recently become an attractive alternative to electronics technology owing to advantages offered by information processing in the optical domain. The photonic crystal [29-32] (PC) is one of the platforms that can enable the miniaturization of photonic devices and their large-scale integration. These man-made periodic nanostructures can be designed to form frequency bands (photonic bandgaps) within which the propagation of electromagnetic waves is forbidden irrespective of the propagation direction. Depending on the dimensionality of spatial periodicity, one can distinguish between several different classes of photonic crystals. One-dimensional photonic crystals are well-known dielectric stacks, such as described earlier, and they can be used as mirrors in vertical cavity surface emitting laser[33], for example. If the periodicity is two-dimensional (2-D), they are referred to as 2-D photonic crystals. Strictly

speaking, these structures are assumed to be infinitely long in the direction perpendicular to the plane in which 2-D periodicity exists. One of the most promising applications of 2-D PCs is photonic crystal fiber [34]. By making the spatial periodicity in three dimensions, real three-dimensional (3-D) photonic crystals [35] can be realized. 3-D PCs can have complete bandgap, and therefore can control propagation of light in all directions. These structures can be realized using standard top-down etching techniques, multiple thin-film deposition techniques, self-assembly, micromanipulation, etc. However, fabrication of 3-D PC structures is still a difficult process, and a more appealing approach is based on the use of lower-dimensional photonic crystals. A structure that has recently attracted a lot of attention is a semiconductor slab perforated with 2-D lattice of holes [36, 37]. The big advantage of these planar photonic crystals (PPC) is their fabrication procedure, which is compatible with standard planar technology used to realize microelectronic systems. Lithographic tunability is another great advantage of PPC concept. For example, lasers that operate at different wavelengths can be monolithically integrated within the same semiconductor slab, and the tuning of the lasing wavelength can be achieved by changing the periodicity of the structure [38].

One of the most promising planar photonic crystal devices is a compact and efficient optical nanocavity, capable of storing electromagnetic energy in very small volumes, for a long period of time. Such a nanoscale optical resonator is of interest for investigation of interaction between light and matter on a nanoscale level. Until recently, the applications of planar photonic crystals have been

restricted to large-scale integration of optical devices for telecommunication applications. However, such a nanocavity can be used for chemical and biological sensing.

PPC cavities can be engineered to concentrate light in the air, and therefore they are natural candidates for applications where strong interaction between light and matter placed in the high optical fields is of interest. This is the case in number of applications including cavity QED experiments [39], biochemical sensing [40] and spectroscopy. By embedding the photonic crystal nanocavities within microfluidic systems similar to those described earlier, a highly functional analysis and sensor systems can be constructed that is capable of analyzing sub-femtoliter volumes of analyte. By using microfluidics, reagents or analytes can be moved from sensor to sensor, surfaces can be selectively functionalized, and calibration tests can be performed all in one monolithic chip. Multilayer soft lithography, which has been discussed previously, exploits the elasticity and the surface chemistry of silicone elastomers in order to create monolithic valves and pumps within microfluidic devices. Through this technology, complex addressable arrays of sensors can be fully integrated within a microfluidic chip. The combination of MSL and photonic crystal based sensors allows for a tremendous amount of functionality to be built into a monolithic system.

Nanocavity Design

Photonic crystal cavities can be formed by modifying one or more holes in the photonic crystal lattice. By making one of the holes bigger, a local increase in

the amount of low-dielectric constant material (air) occurs and therefore one sees a corresponding increase in the energy of the modes supported in the bulk photonic crystal. Modes that were originally confined in the dielectric material (dielectric band modes) will now be pulled up into the band gap, and be trapped in the energy well formed by increasing the size of the hole. This bound state exists close to the dielectric band and in its nature is similar to an acceptor level in semiconductors. Therefore, modes created by modification of dielectric band are called acceptor modes. Similarly, by reducing the size of one of the holes, we form bound states close to the air band - donor modes [41]. Acceptor and donor modes in the triangular lattice are shown in Figure 34.

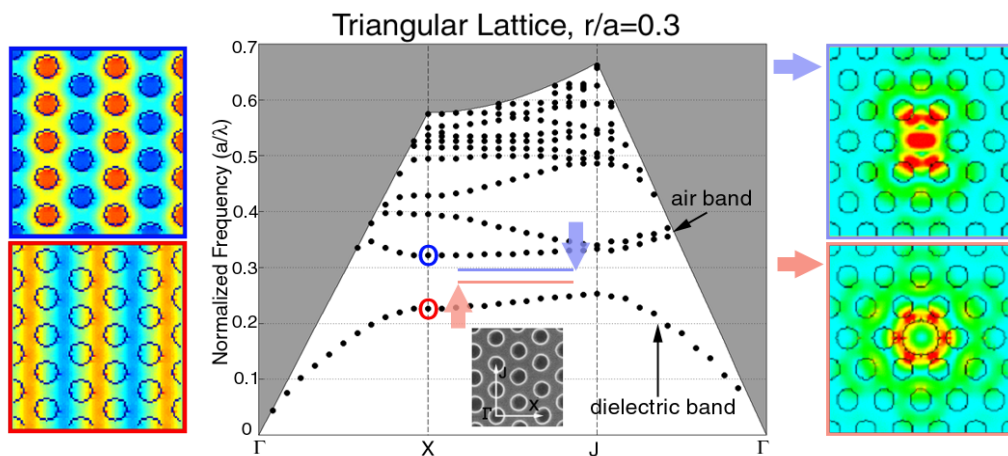


Figure 34. Dispersion diagram for the modes supported in the triangular lattice planar photonic crystal ($r/a = 0.3$ this time). Mode profiles for one component of the E field in the dielectric (red) and air (blue) band, take at the X point, are also shown.

The efficiency of a resonator, described by a quality factor (Q), can be expressed as the ratio of energy stored in the cavity and energy lost (emitted) from the cavity in one cycle:

$$Q = 2\pi \frac{W_{stored}}{W_{lost}} = 2\pi\nu \frac{W_{stored}}{P} \quad 5.1$$

where ν is the frequency of the mode and P power emitted from the laser.

In case of 2-D photonic crystal, with infinitely many PC layers around the defect, light can be completely trapped to the defect. However, in cavities defined in photonic crystal slabs, modes will suffer from radiation losses due to the coupling into the continuum of radiation modes. These components contribute to the out-of-plane losses of the cavity. At the same time, light can leak laterally due to the finite number of the photonic crystal layers surrounding the cavity, contributing to the in-plane losses of the resonator. The quality factor of photonic crystal resonator can be broken into lateral quality factor Q_{lat} and vertical quality factor Q_{vert} that take into account in-plane and out-of-plane losses, respectively.

$$\frac{1}{Q} = \frac{1}{Q_{lat}} + \frac{1}{Q_{vert}} \quad 5.2$$

By adding more photonic crystal layers around the cavity, the lateral leak can be completely suppressed and we can assume that Q_{lat} can be arbitrary high [42]. Therefore, the ultimate Q is limited by Q_{vert} . Unfortunately, the simplest photonic crystal cavity, formed by reducing the size of one of the holes, known in literature as single defect cavity, suffers from large radiative losses (small Q_{vert}). The best quality factor that one can achieve with this cavity is limited to $\approx 2,000$ [39, 43]. This Q is obtained in a cavity with $r/a=0.3$ when the radius of the defect

hole is slightly reduced to $r_{\text{def}}/a=0.2$. This cavity design is not robust since the defect hole is only slightly smaller than bulk PPC holes, and any fabrication related fluctuations can form unintentional defects and spoil the Q of the cavity. At the same time, quality factor of $Q \approx 2,000$ is not spectacular, and better Q is needed for all applications proposed in the previous section. The problem of high-Q cavity design has recently attracted a lot of research attention and several designs were proposed and characterized experimentally [44-53].

The high-Q cavity geometry that we proposed is based on fractional edge dislocations in the single defect triangular lattice photonic crystal [39]. The planar photonic crystal is based on a free-standing membrane: high dielectric constant slab (refractive index $n=3.4$) is perforated with 2-D lattice of holes with periodicity a and is suspended in the air. The cavity consists of a defect hole (radius r_{def}) that is smaller than surrounding holes (radius r) which define the photonic crystal mirror. The row that contains the defect hole is elongated by moving two photonic crystal half-planes a fraction of a lattice constant apart in the ΓX direction Figure 35. Each half-plane is moved by $p/2$, yielding total dislocation of p .

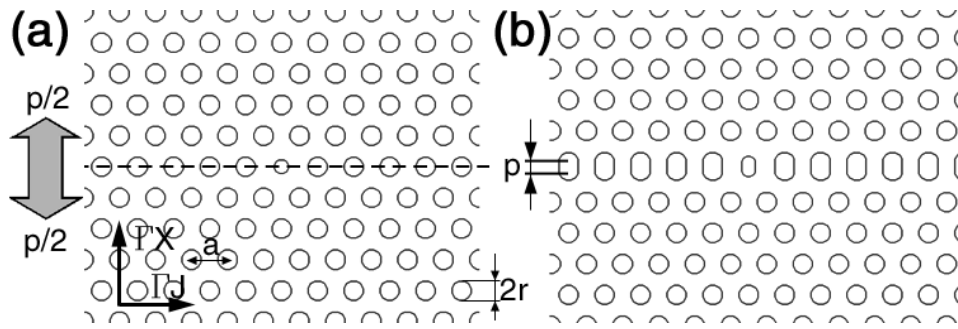


Figure 35. (a) Conventional single-defect cavity ($p=0$). When structure is "cut" along the dashed line, and two PPC half-planes are dislocated along ΓX direction by $p/2$, (b) high-Q cavity can be formed ($p=0.25 \cdot a$).

It was shown that in such photonic crystal cavity, with $r/a=0.275$, $r_{\text{def}}/a=0.2$ and $d/a=0.75$ (d is thickness of the slab), it is possible to achieve Q factors as high as 11,000 by tuning the dislocation parameter p . The Q was maximized when $p/a=10\%$. These high Q values were obtained while maintaining a very small mode volume of $V_{\text{mode}} \approx 0.1(\lambda/2)^3$. These cavities were originally designed for cavity QED experiments, where strong-coupling between atoms introduced into the high field region of the cavity and light trapped in the cavity was to be investigated[39]. However, it is clear that the presence of a hole at the point of maximum field intensity is not desirable in low-threshold laser designs, since the overlap with the gain region, provided by quantum wells is decreased. Therefore, one must revisit the problem of cavity design in order to investigate the influence of the defect hole size (r_{def}) on the Q factor of the cavity.

In order to improve the lateral confinement of light, structures with slightly bigger holes ($r/a=0.3$) were analyzed. This results in a more compact cavity, since fewer layers of photonic crystal can be used to efficiently confine the

light. On the other hand, bigger holes in the photonic crystal mirror increase the scattering of light in the vertical direction and therefore result in decreased Q factors. As the first step, the band diagram of the bulk photonic crystal with parameters $r/a=0.3$, $d/a=0.75$, and $n_{\text{slab}}=3.4$ was calculated, and it was found that a bandgap exists for vertically even modes (TE-like) for the normalized frequencies in the range $a/\lambda \in (0.2508, 0.3329)$. 3-D FDTD was used to calculate this dispersion diagram. The discretization used in FDTD algorithm was $a=20$ computational points. Next, various high-Q cavity designs were modeled in order to find their eigen modes. A single-defect donor cavity in a triangular lattice photonic crystal without the fractional edge dislocation is known to support two doubly-degenerate, linearly polarized, dipole modes [30, 42]. However, as the photonic crystal lattice is stretched by introducing a fractional dislocation, these modes start to interact and the degeneracy between them is lifted. In Figure 36 the results of 3-D FDTD analysis of the structure with $p/a=10\%$, $r_{\text{def}}=0.2a$, $r=0.3a$ and $d=0.75a$ are shown. Two dipole modes, labeled LQ and HQ, are found to exist in the cavity. The mode at longer wavelength can have an order of magnitude better Q factor value and therefore is called HQ (high-Q) mode. Additional modes are found close to the air-band, as well. Those modes are not localized to the defect hole, but are instead attributed to the waveguide modes of the elongated central row.

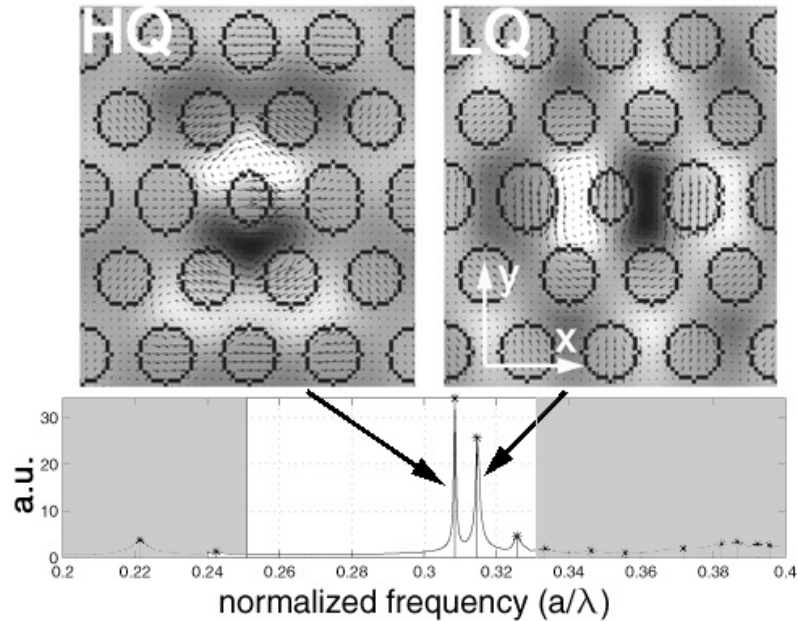


Figure 36. Defect modes of the cavity with $p/a=10\%$ and $r_{\text{def}}=0.2a$. (a) Cavity supports two dipole modes, and their profiles are shown (B_z component and vector of the E field). Spectrum of the modes supported in the cavity, obtained using 3-D FDTD, is also shown. The bandgap is shown in white. (b) Amplitude of the E field is shown. It can be seen that light is localized in the small defect hole.

In Figure 37, the dependence of the eigen-frequency and Q of HQ dipole mode on the stretching (dislocation) of the central row (p/a) and on the size of the defect hole (r_{def}/a) is shown. It can be seen that by increasing the dislocation, the splitting between the two dipole modes increases. Also, as the defect hole becomes larger, the modes shift towards higher frequencies. This shift occurs since a larger hole in the center of the cavity leads to an increased overlap between the optical field and air. One more interesting feature is that splitting between LQ and HQ modes does not depend strongly on the size of the central hole, and is mostly dependant on the amount of dislocation introduced. The mode of interest for laser applications is the HQ mode, since it has an order of magnitude higher Q and therefore will reach threshold first. The quality factors of

LQ modes are limited to several hundreds and therefore are not of practical importance. In the calculations, the cavity was surrounded with five layers of photonic crystal. Figure 37 (b) tells the reader that the best Q that one could hope to achieve in the modeled cavity geometry is around 7,000. In comparison, one is able to achieve Q's as high as 11,000 when $r/a=0.275$. As expected, due to the increased size of the bulk photonic crystal holes ($r/a=0.3$), light scattering in the vertical direction increases, and therefore the Q-factors are smaller. The optimal design (Q-factor maximized) requires more dislocation as r_{def} decreases. This can be understood by looking at spatial frequencies that exist in the Fourier spectrum of the HQ mode. In order to increase the Q of the cavity, components that lie within the light cone need to be minimized. This can be achieved by changing the size of the air-region in the cavity in order to balance the energy that exists in each lobe of the mode [Figure 36 (b)], and in that way minimize its DC component [39]. The change of the area occupied by the defect hole, induced by stretching of the central row, is $\Delta A=2r_{\text{def}} \cdot p$. From this equation it follows that in order to achieve the same influence on the mode larger p's are needed when r_{def} is made smaller. In other words, for a large defect hole, small change in p has great influence on the mode since most of the light is located in the hole.

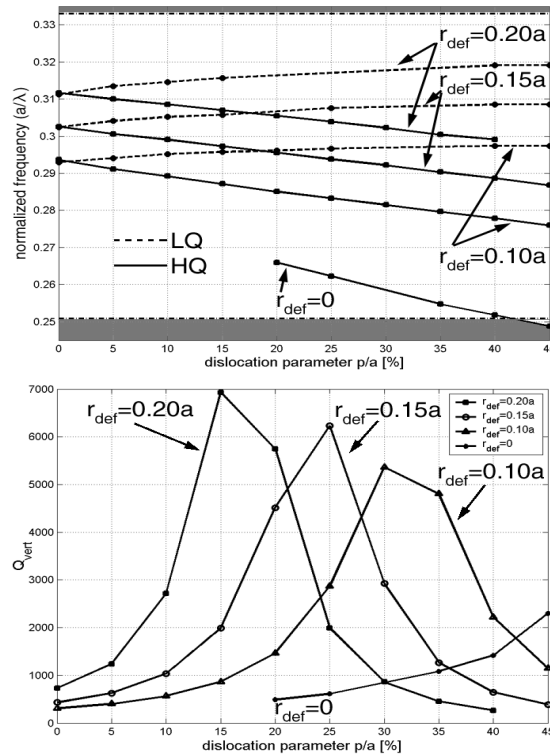


Figure 37. (a) Dependence of the eigen-frequencies of the two dipole modes of the cavity on the amount of dislocation introduced (p), and the size of the defect hole (r_{def}). (b) Dependence of the vertical quality factor of the HQ mode on p and r_{def} . Only five layers of photonic crystal surrounding the defect hole was used.

Another important figure of merit of any laser design is the gain provided by the laser cavity. As the defect hole diameter is decreased and the amount of dislocation is increased, we expect a better overlap between the optical cavity mode and the quantum wells, and therefore reduced laser threshold. However, it is important in our application that central defect hole is as large as possible so that one can achieve strong interaction between light emitted from the laser and material (nanoparticles, single molecules, chemical fluids, gasses, etc.) placed in the strong optical field of the laser. Therefore, $r_{def}=0.15a$ and $p=0.25a$ as a good compromise for our initial laser sensor design was chosen.

In most common applications, planar photonic crystals are in the form of a free standing membrane suspended in the air. However, it is also of interest to explore the PPC properties when the air is replaced with material with a refractive index greater than 1. This is the case when PPC lasers are used as chemical sensors [40] and tunable filters in which case PPC cavities are backfilled with electro-optic or non-linear polymer in order to change their resonant frequency by applying external electromagnetic fields.

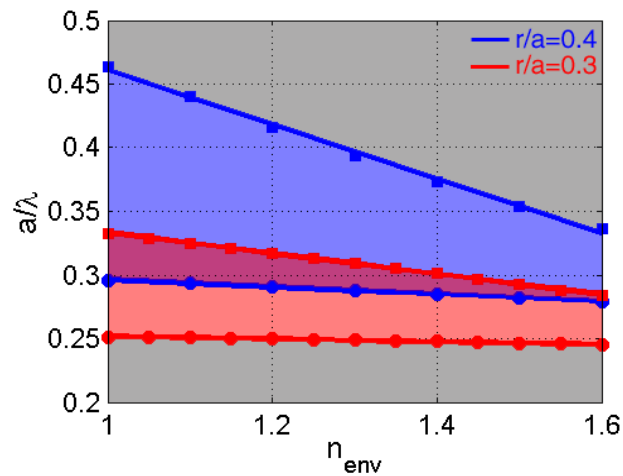


Figure 38. Air-band and dielectric-band edge dependence on the refractive index of environment (n_{env}) surrounding PPC slab, for $r/a=0.3$ (red) and $r/a=0.4$ (blue).

In Figure 38 one can see the dependence of the dielectric-band and air-band edges when a PPC is immersed in materials with various refractive indices. The thickness of the PPC is $d/a=0.75$ and its refractive index $n_{slab}=3.4$. The hole size is $r/a \in \{0.3, 0.4\}$. As expected, the band edges experience redshift when the PPC slab is immersed in a material with higher refractive index. Also, the width of the bandgap decreases when n_{env} increases. The bottom of the air band is more affected with increased n_{env} , since air-band modes have larger spatial overlap with

the environment. From Figure 38 one can deduce that the bandgap will close when $n_{env} \approx 2$ in both structures. In the case of a crystal with $r/a=0.4$ the dependence of the band-edges on n_{env} can be well approximated with

$$\frac{a}{\lambda_{dielectric}} = 0.0289n_{env} + 0.3255 \quad 5.3$$

$$\frac{a}{\lambda_{air}} = 0.2139n_{env} + .6748 \quad 5.4$$

When $r/a=0.3$, band-edges can be expressed as

$$\frac{a}{\lambda_{dielectric}} = -0.0104n_{env} + 0.2621 \quad 5.5$$

$$\frac{a}{\lambda_{air}} = -0.0104n_{env} + 0.4144 \quad 5.6$$

As expected, the structure with bigger holes is more sensitive to the changes in the refractive index of environment. From these equations one finds that the sensitivity of the air-band edge is better than $\Delta\lambda \approx 700 \cdot \Delta n$, when $r/a=0.4$. This suggests that by monitoring the shifts in the emission wavelength of a band-edge laser (that operates at the air-band edge) very small changes in the refractive index of the ambient could be detected.

It is of interest to determine the change in the Q and eigen-frequency of the modes supported in the cavity based on fractional edge dislocations as the cavity is back-filled with chemicals with higher refractive index ($n>1$). In Figure 39 (a) it is observed that the highest Q that one could hope to achieve in the modeled cavity design occurs at an ambient refractive index $n_{env}=1$ (air), and this value deteriorates as the refractive index of the ambient surrounding the photonic crystal cavity is increased. This decrease in Q is a result of the weaker vertical

confinement of light by total internal reflection, and can be compensated for by increasing the thickness of the photonic crystal slab.

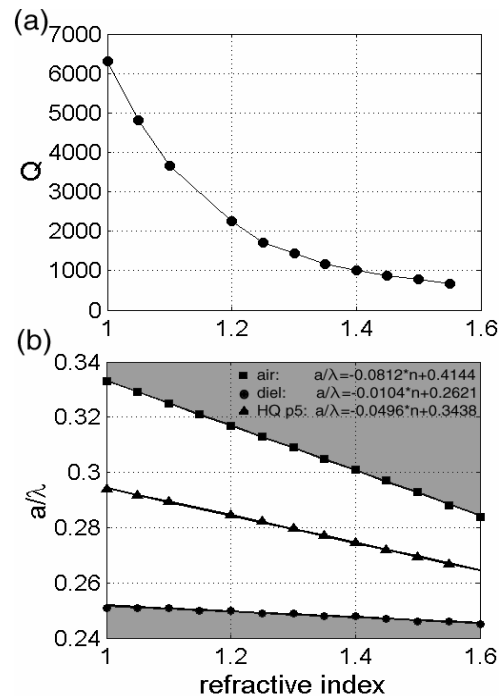


Figure 39. Dependence of the (a) Q factor and (b) eigen-frequency of cavity resonance on the refractive index of analyte introduced in the cavity with p/a=25%.

It is interesting to note that the frequency of the resonant mode also depends linearly on the refractive index of the environment (n_{env}) [Figure 39 (b)]. From linear fits of the dependence of the resonant frequency on n_{env} , one can estimate the sensitivity of the cavity, and find that the wavelength shift of the resonance is approximately $\Delta\lambda \approx 266 \cdot \Delta n_{env}$, where Δn_{env} is the change in refractive index. The simplest method of optically sensing ambient material uses wavelength shifts in the laser spectrum when the laser is immersed into a solution or exposed to a material to measure its refractive index. In this method, the sensitivity of the sensor depends on the smallest change in refractive index that

can be optically detected. In passive devices, this is related to the width of the cavity resonance peak, which in turn is determined by cavity quality Q . If one assumes that the cavity is embedded in a typical polymer ($n_{\text{env}}=1.4$) a wavelength shift that is still observable from cavity with $Q=1,000$ is $\Delta\lambda=1.55$ nm, which corresponds to change in refractive index of $\Delta n \approx 0.0056$. On the other hand, once optical gain is introduced into the cavity, as in the case of the proposed laser spectrometer, the linewidth of emission is significantly narrowed ($\Delta\lambda \approx 0.12$ nm), and sensitivities to $\Delta n < 0.001$ can be measured even in cavities with modest Q factors. Figure 39 suggests that the edge of the air band is even more sensitive to changes in the refractive index than the cavity mode itself. Therefore, band-edge lasers [54-58] might be even better choice for applications where high sensitivity to the changes of refractive index are needed. However, band-edge lasers operate at extended bulk PPC modes, with large mode volumes, and therefore are not suitable for applications where high spatial sensitivity is needed (e.g., single-molecule detection).

At the end of this section the field strength in the central defect hole of the cavity is estimated. Using Equation 5.1, one can write the energy stored in the resonator as

$$W_{\text{stored}} = PQ_{\text{env}} \frac{\lambda}{2\pi c} \quad 5.7$$

where Q_{env} is the Q factor of the cavity immersed in the environment with refractive index n_{env} . Normalized energy of the cavity mode (K_{env}) can be written as

$$K_{env} = \frac{\iiint \frac{1}{2} \varepsilon |E|^2 + \frac{1}{2} \mu |H|^2 dV}{\varepsilon_{def} |E_{def}|^2 \left(\frac{\lambda}{2}\right)^3} = \frac{W_{stored}}{\varepsilon_{env} \varepsilon_0 |E_{def}|^2 \left(\frac{\lambda}{2}\right)^3} \quad 5.8$$

and depends on the environment that the cavity is immersed into. The E_{def} is the maximum electric field strength in the hole at the center of the cavity. It is important to remember that the resonator can be embedded in materials different than air, and therefore one has to use appropriate permeability of the material for ε_{def} . Combining these equations, the maximum field strength at the center of the cavity can be expressed as

$$E_{def} = \left(\frac{4}{\lambda n_{env}} \right) \sqrt{\frac{P}{4\pi\varepsilon_0 c}} \sqrt{\frac{Q_{env}}{K_{env}}} \quad 5.9$$

In Figure 40 the dependence of E_{def} on refractive index of the environment n_{env} is shown, assuming typical emitted power of $P=60\text{nW}$ as in the case of our lasers (30nW at each side of the cavity), and emission wavelength of $\lambda=1.55\mu\text{m}$. One can see, that in the case of a cavity suspended in the air, the maximum field is on the order of the breakdown strength of the air $E_{breakdown} = 3 \frac{V}{\mu\text{m}}$.

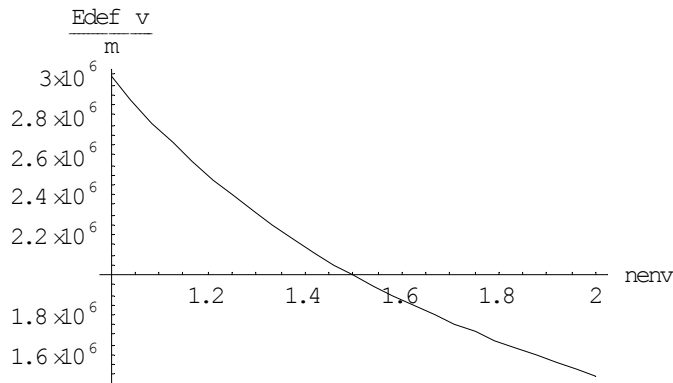


Figure 40. Dependence of E_{def} on refractive index of the environment n_{env} .

Photonic Crystal Nanolasers as Chemical Sensors

The construction of compact spectroscopic tools for the optical analysis of ultra-small ($<10^{-15}$ liter) sample volumes remains an important goal in the development of integrated microfluidics systems. Miniaturization of appropriate light sources and detectors can enable very compact and versatile "laboratory on a chip" devices, in which many analytical functions can be monolithically combined. The porous cavity design (Figure 41) permits the introduction of analyte directly into the high optical field of the laser cavity, and, due to the ultrasmall mode volume of our lasers, permits the sensitivity to optical changes within femtoliter volumes. The introduction of absorbing or fluorescing molecules into such cavities is expected to have a large influence on the optical signature, and the high fields obtained in the cavity can be used for spectroscopy of the cavity contents (e.g., Raman or absorption spectroscopy). This will enable the sensing and analysis of individual organic molecules or self-assembled quantum dots, and offers a unique opportunity to achieve strong interaction between light and molecules on a nanoscale level. By combining many of these PPC lasers each with a different peak wavelength true spectroscopy can easily be accomplished.

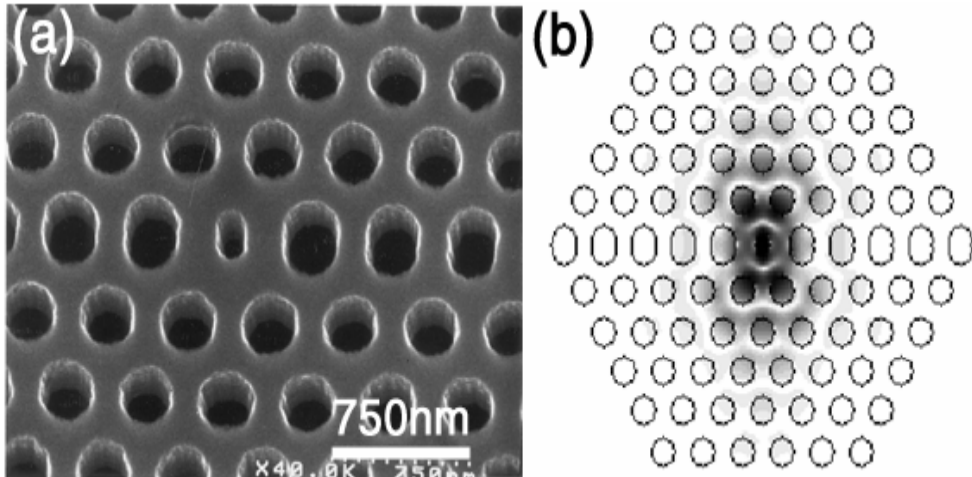


Figure 41. Scanning electron micrograph and calculated field distribution ($|E_{ampi}|$) of a photonic nanocavity laser sensor. It can be seen that the energy of the mode is mostly confined to the central defect hole.

Fabrication Procedure

InGaAsP quantum well material was grown on InP substrate using metal-organic chemical vapor deposition (MOCVD). Optical gain is provided by four 9nm thick, compressively strained, quantum wells with an electronic bandgap at $\lambda_{bg}=1.55\mu\text{m}$, separated by 20nm thick InGaAsP barriers ($\lambda_{bg}=1.22\mu\text{m}$). Because of the compressive strain, the coupling is the strongest to the TE polarized modes of the slab. This is desirable since in triangular lattice PPC the bandgap is larger for TE-polarized light. This active material is placed in the center of a 330nm thick InGaAsP slab ($\lambda_{bg}=1.22\mu\text{m}$), with 1 μm thick sacrificial InP layer underneath the slab. An InGaAs etch stop is introduced above the InP substrate, and the active quaternary material is designed to operate at $\lambda=1.55\mu\text{m}$. The wafer structure is shown in Table 4.

Table 4. InGaAsP wafer structure

| layer | composition | layer description | λ (μm) | Thickness (nm) |
|-------|-------------|-------------------|-----------------------------|----------------|
| 12 | InP | cap | | 50 |
| 11 | InGaAsP | elect. barrier | 1.22 | 117 |
| 10 | InGaAsP | QW | 1.55 | 9 |
| 9 | InGaAsP | elect. barrier | 1.22 | 20 |
| 8 | InGaAsP | QW | 1.55 | 9 |
| 7 | InGaAsP | elect. barrier | 1.22 | 20 |
| 6 | InGaAsP | QW | 1.55 | 9 |
| 5 | InGaAsP | elect. barrier | 1.22 | 20 |
| 4 | InGaAsP | QW | 1.55 | 9 |
| 3 | InGaAsP | elect. barrier | 1.22 | 117 |
| 2 | InP | sacrificial layer | | 1000 |
| 1 | InGaAs | etch stop | | 20 |
| | InP | substrate | | |

Fabrication procedure consists of electron-beam lithography, followed by two dry- and one wet-etching steps. Ideally, only one mask layer would be needed to define patterns in InGaAsP material of interest. However, due to poor etching selectivity between e-beam resist and InGaAsP in the etching system the mask amplification method is used. The etch mask consists of 100-140nm thick SiO_2 or Si_3N_4 layer, deposited at room temperature using RF sputtering technique described in Chapter 3. Both masks performed similar in the etching chemistry, but in this section a Si_3N_4 layer is used as the dielectric mask layer. 120nm of polymethyl methacrylate (PMMA), electron-beam (e-beam) sensitive resist, is deposited on top of the Si_3N_4 mask layer. A 2% solution of PMMA (molecular

weight 950K) diluted in chlorobenzene was used. The PMMA was baked on the hot-plate at 150°C for 40 min. E-beam lithography was performed using a Leica EBPG 5000. Electron beam voltage was 30KeV, and the dose used to define the pattern in PMMA was 5 μ C/cm². A number of different cavity geometries were beam-written at the same time. By varying the electron dose and the periodicity of the lattice, one can span the entire design space of the PPC nanocavities by changing a , r , r_{def} and p/a independently. Upon completing e-beam lithography, the PMMA was developed for 30s in Microchem PMMA developer and rinsed for 15s in isopropyl alcohol (IPA). This procedure removes the areas exposed by the e-beam, leaving behind a positive mask in PMMA. The PMMA patterns were transferred into the Si₃N₄ layer using reactive ion etching (RIE). 20 sccm of CHF₃ reactive gas was used and the chamber pressure was kept at 16 mTorr. The RF power used in this RIE step was 90 W and with a DC bias of 480 V. The etch was done for 3 minutes. At the end, the patterns were transferred into the InGaAsP using inductive-coupled plasma RIE etching. A mixture of Ar and Cl was used to perform this final etch step. The ICP-RIE etch starts with 15 sec treatment with 10 sccm of Ar (P=1mTorr), and is followed by 15sec etch in Cl/Ar chemistry. The etch-parameters are pressure P=1 mTorr, ICP power P_{ICP}=800 W, RF power P_{RF}=155 W and gas mixture of Cl:Ar=15 sccm:10 sccm. In spite of short etch time one could etch about 1.3 μ m into the InGaAsP/InP material with straight sidewalls throughout the thickness of the InGaAsP slab. Finally, the remaining Si₃N₄ mask is removed in a HF acid and the InGaAsP membrane is released from the substrate by wet etching in 4:1 HCl:water solution at 4°C. HCl

goes into the photonic crystal holes, and selectively attacks InP sacrificial layer, leaving InGaAsP membrane and InGaAs etch-stop layer intact. However, since HCl does not attack InP isotropically, but rather along well defined crystal planes, it is not straightforward to release the membrane from the substrate. Therefore, care needs to be taken when designing the cavities in order to facilitate the undercutting. The whole fabrication procedure is summarized in Figure 43.

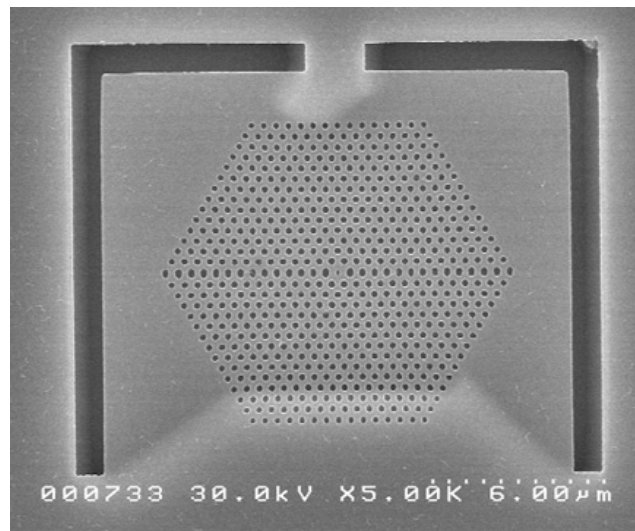


Figure 42. SEM micrograph of high-Q planar photonic crystal cavity, defined in the suspended membrane

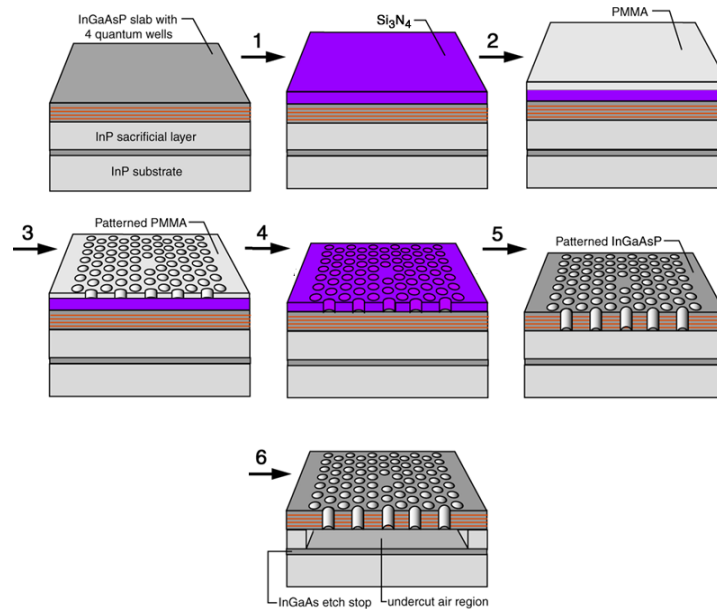


Figure 43. Fabrication procedure for PPC lasers made in InGaAsP material. RF sputtering (1) is used to deposit dielectric and is followed by deposition of PMMA e-beam resist (2). E-beam lithography is used to define patterns in PMMA (3) and RIE to transfer them into Si_3N_4 (4). Finally, patterns are etched into InGaAsP using ICP-RIE (5) and the membrane is released from the substrate in HCl (6). Final structure is a free standing InGaAsP membrane with four quantum wells (thin red layers).

Microfluidic Integration of Photonic Crystal Cavities

The structure can then be embedded into a polydimethylsiloxane (PDMS) chip for testing. The PDMS chip is fabricated using standard multilayer soft lithography (MSL) techniques. A photoresist mold is created using SU8-2015 which has been spun at 4000RPM to yield a height of approximately $12 \mu\text{m}$ ⁴. After the mold has been treated with trimethylchlorosilane (TMCS), 30 g of 5:1 GE RTV615 elastomer is poured onto the mold and partially cured at 80°C for 45 minutes to create the flow channels. Once holes have been punched into the flow channels, the flow layer is ready to be aligned to the PPC layer so that one flow

⁴ SU8 spinning was performed using a Laurel spinner model WS-400A-6NPP/LITE.

channel passes over several photonic crystal cavities. The pitch of the flow channels can be set to overlap the PC cavities in such a way that the alignment is much easier.

The PPC structure can not be directly embedded in PDMS since the phosphorous content of the PPC poisons the catalyst such that the elastomer never cures. In order to embed the PPC structure, it must first be coated with another material. PMMA was chosen since it does not interfere with PDMS curing and is also non-damaging for the PPC structure. The PPC structure is coated with PMMA by spinning 490K molecular weight PMMA at 5000RPM onto the structure⁵. The PMMA is spun onto the PPC membrane side first and then another layer of PMMA is spun onto a blank 3” silicon wafer. The PPC device is placed membrane first onto the wafer and the two are baked at 150°C for 4 hours. This bonds the PPC device to the wafer. After baking the assembly is allowed to cool to room temperature and then a layer of PMMA is spun on top of the assembly to cover the backside of the PPC device. This is also baked at 150°C for 4 hours to drive the solvent from the PMMA. After baking the sample is allowed to cool once again and is ready for PDMS treatment.

Approximately 10 g of 20:1 GE RTV615 is poured onto the PPC-wafer assembly and cured at 80°C for 8 hours. Once the PDMS is fully cured, the assembly is placed into a bath of acetone at 95°C until the PPC structure has lifted off the silicon wafer. Since PDMS is permeable, the acetone seeps through the PDMS layer and dissolves the PMMA that bonded the PPC device to the silicon wafer. After the two have been separated, the acetone is removed and replaced

⁵ PMMA spinning was performed using a Laurel spinner model WS-400A-6NPP/LITE.

with isopropyl alcohol (IPA). The sample is allowed to soak in IPA at 95°C for 10 minutes. Afterwards, the PPC device is freed from the silicon wafer, but still encapsulated by the PDMS. The PDMS is then removed from the silicon wafer with the PPC device and placed on a hotplate at 200°C for at least 2 hours. This is necessary to drive off any remaining solvents which may be trapped inside the PDMS.

In order to seal the flow layer to the PPC device layer, it is necessary to plasma treat the surface of the PPC PDMS layer. The PPC PDMS layer is placed inside a Tegal Plasmaline plasma system to perform the treatment. The layer is etched with a combination of O₂ and CF₄. The O₂ plasma treatment is common in the literature for sealing PDMS to glass; however, the CF₄ allows for a thin layer of PDMS to be removed as discussed in Chapter 2. The recipe for etching is as follows: 20 sccm O₂, 60 sccm O₂/CF₄, 200 W forward power, 120 W reflected power, 30 minutes. One bonus feature of the plasma treatment is that it cleans the surface of the PPC membrane removing any PMMA which was not removed during the solvent treatment. After the plasma treatment the flow layer and PPC layer can be aligned and sealed. The assembly is then cured overnight at 80°C. For applications in which it is not to critical to have individual flow channels, a large well, which encompasses the entire PPG structure, can be fabricated using similar methods. A picture of the integrated PPC structure with microfluidic flow channels is shown in Figure 44.

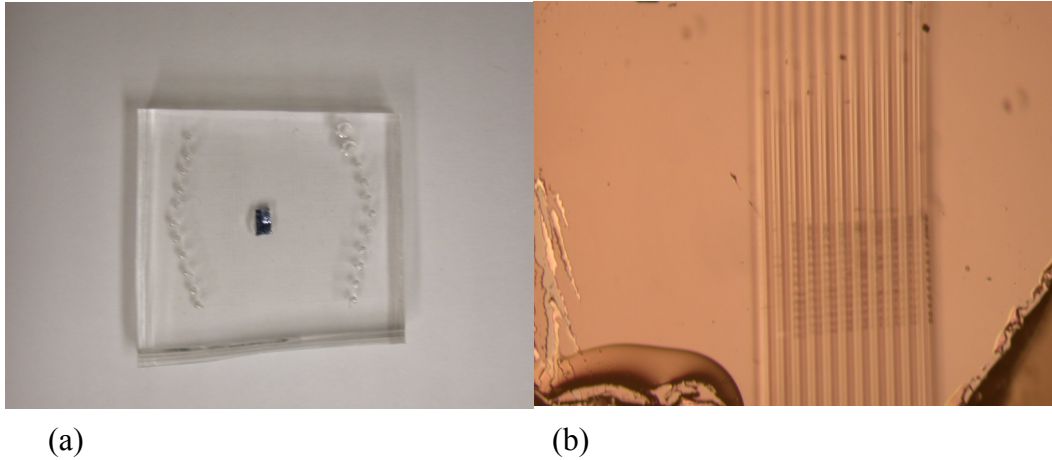


Figure 44. (a) A planar photonic crystal (PPC) structure embedded in a PDMS flow cell. (b) The PPC lasers can be seen underneath the flow channels. The channels are 40 μm wide and spaced 15 μm apart.

Chemical Sensing Using Photonic Crystal Nanolasers

Fabricated structures were tested at room temperature using micro-photoluminescence approach (μPL). Due to poor heat sinking in the membrane-based devices, optical pumping was performed in pulsed regime, with limited duty cycles. The experimental setup is shown in Figure 45. A diode laser emitting at $\lambda=830\text{ nm}$ was used to pump the PPC structures. In most cases structures were pumped with .5-1% duty cycles, using 15-30 ns pulses with 3 μs periodicity. The pump beam was focused through 100x objective lens onto the sample surface to obtain a spot size of about $2.5 \cdot 1.5\ \mu\text{m}^2$. The emission from the cavities was collected through the same lens, and the spectrum of the emitted signal was analyzed with an optical spectrum analyzer (OSA). Flip-up mirrors were used to obtain the optical images of the excitation pump-spot and the cavity modes.

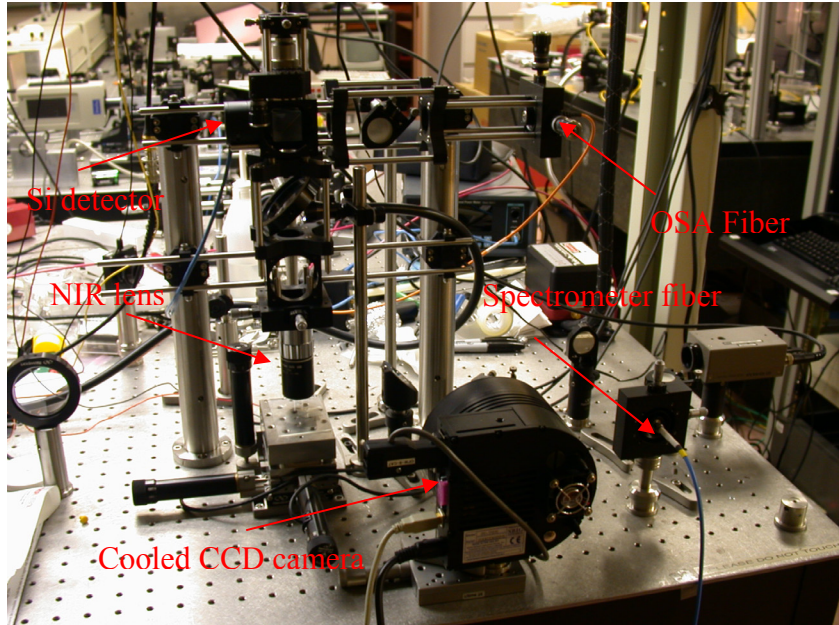


Figure 45. Experimental setup. Pump beam ($\lambda=830$ nm) is focused on the sample using high-power NIR lens (100x). Si detector behind beam splitter (BS) is used to monitor the pump power. Emission from the sample is collected using the same lens, and is analyzed with an optical spectrum analyzer (OSA). The emission from photonic crystal resonators can also be monitored with a cooled CCD camera or a fiber-optic spectrometer using a pair of flip-up mirrors.

First one has to measure the emission from the unprocessed InGaAsP material and obtain the gain spectrum of the active material. It is found that emission exists between 1300 nm and 1650 nm, with a maximum at around 1550 nm. Assuming the lattice constant of $a=436$ nm (as in the case of the most of the fabricated structures) this wavelength range corresponds to normalized frequencies of $a/\lambda \in (0.264, 0.335)$, which is within the bandgap of the bulk photonic crystal mirrors surrounding the cavity.

The simplest method of optically sensing ambient material uses wavelength shifts in the laser spectrum to measure refractive index of ambient. In this method, the sensitivity of the sensor depends on the smallest change in

refractive index that can be optically detected. In passive devices, this is related to the width of the cavity resonance peak which in turn is determined by cavity quality Q . However, a laser linewidth is much narrower than a passive cavity resonance, and even smaller shifts in the lasing wavelength can be detected by taking advantage of the spectral narrowing from stimulated emission above laser threshold.

To test the influence of a change in ambient refractive index on the laser spectrum of a cavity, the photonic crystal lasers was backfilled with isopropyl alcohol and methanol. Figure 46 shows position of the resonances from six different lasers after immersion in air, isopropyl alcohol (IPA) and methanol. It can be seen that wavelength shifts of up to 67 nm can be observed when a cavity is immersed in IPA. This red-shift corresponds to a change in refractive index from 1.0 to 1.377, and yields roughly 1nm spectral shift for a 0.0056 change in refractive index. When IPA is replaced with methanol ($n=1.328$), the laser resonance experiences a blue shift of ≈ 9 nm, which is again in good agreement with predicted shift of ≈ 13 nm from the theoretical predictions (Figure 39). The dependence of the cavity resonance wavelength on the lithographic laser geometry, particularly the lattice constant (a) and the dislocation (p/a) in the photonic crystal cavity has also been studied. Resonances experience red shifts of ≈ 80 nm when the periodicity is changed from $a=446$ nm (dashed lines) to $a=460$ nm (solid lines). This lithographic tuning of the emission wavelength can be used to ensure an overlap of the cavity resonance peak with the InGaAsP quantum well emission gain curve even when the cavities are immersed in a

reagent. Laser threshold curves before and after immersion into alcohol are also presented in Figure 46. After immersion, the laser threshold power for the cavity measured was reduced since the emission wavelength was shifted to match the maximum gain of the quantum wells. However, the differential quantum efficiency of the immersed cavity is slightly lower, which may reflect the lower laser cavity Q after immersion.

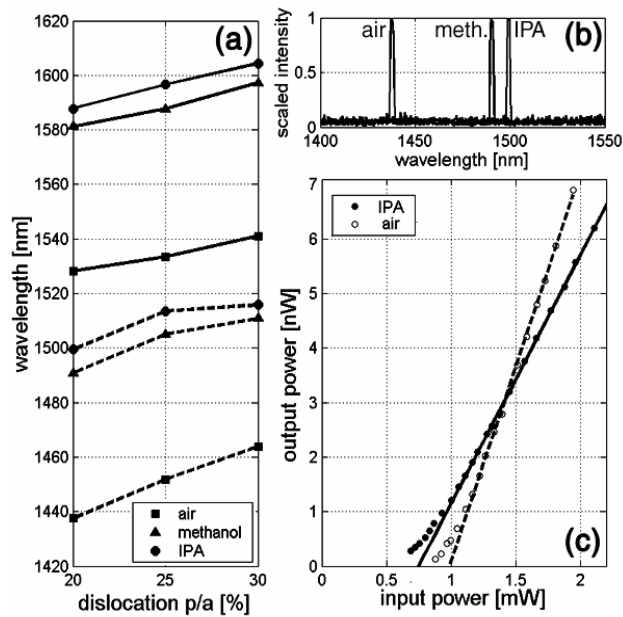


Figure 46. (a) Sensor response measured from 6 nanocavities with a lattice parameter of $a=446$ nm (dashed lines) and $a=460$ nm (solid lines) as a function of p/a dislocation parameter. The three curves correspond to the laser wavelength with air, methanol and IPA backfilled into the cavity. (b) Spectrum change and (c) threshold curve change of laser before and after filling with IPA.

In order to explore the sensitivity of the lasers on the changes in the refractive index of environment fluids with known refractive index⁶, in the range $n_{\text{env}} \in (1.295, 1.335)$ (specified at $\lambda=1.5$ μm) with step $\Delta n_{\text{env}}=0.005$ were used. A

⁶ Refractive index fluids are based on mixture between perfluorocarbon and chlorofluorocarbon.

new sample was fabricated, with total of 9x8 cavities [nine rows (R) and eight columns (C)]. Here the results for three different cavities, labeled R_6C_3 , R_7C_5 and R_7C_3 according to their position within the 9x8 matrix. Cavities in column 5 (C_5) have fractional edge dislocation $p/a=20\%$, whereas cavities in column 3 (C_3) have dislocation of $p/a=10\%$. Structures in row 6 (R_6) have lattice constant $a=427$ nm, and structures in row 7 (R_7) have lattice constant $a=454$ nm. Figure 47 (a) shows the dependence of the frequency of the resonant HQ mode as a function of the refractive index of environment (n_{env}). It can be seen that frequency shifts depend linearly on n_{env} , as predicted by numerical analysis. The experimentally obtained sensitivities (slopes) are in good agreement with numerical results.

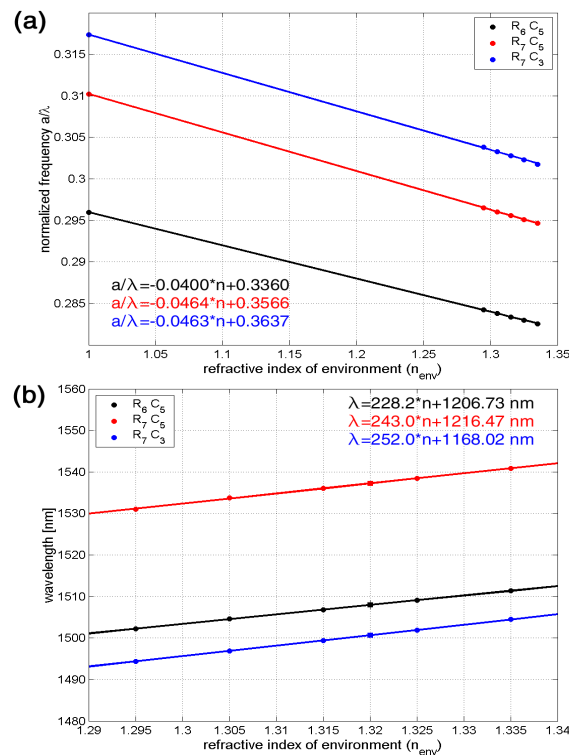


Figure 47. Dependence of (a) a/λ and (b) λ of HQ mode on refractive index of the environment (n_{env}). Three different cavities, labeled R_6C_3 , R_7C_5 and R_7C_3 were tested.

While the relation between a/λ and n_{env} is useful for comparison between theory and experiments, relation between λ and n_{env} is of more practical importance. That dependence is shown in Figure 47 (b) and one can see that the emission wavelength depends almost linearly on the refractive index of environment. The sensitivity of the laser emission wavelength on the changes in n_{env} is $\Delta\lambda=243 \cdot \Delta n_{\text{env}}$ in case of structure R_7C_3 , and this is very close to sensitivity obtained using 3-D FDTD model ($\Delta\lambda=266 \cdot \Delta n_{\text{env}}$). In the experiments n_{env} was changed in steps $\Delta n_{\text{env}}=0.01$. The data points represented by squares in Figure 47 (b) correspond to $\Delta n_{\text{env}}=0.005$. It can be seen that they also follow the predicted linear trend, and red shift of ≈ 1.2 nm is measured (structure R_7C_3) when n_{env} is changed from 1.315 to 1.32.

Detection and Quantization of Nanoparticles

The PPC nanolaser has been very useful for detecting chemicals and has been shown to have a linear response in lasing wavelength with index of refraction. This is very useful for many other applications including sensing of very small particles. A large number of biological specimens of interest can be dissolved in water. A suspension of this can be passed over one of the PPC detectors and information should be able to be determined from the sensor. In order to test this, a solution of carboxylate modified latex beads were suspended in water and placed onto the sensor. The concentration of beads to water was approximately .25% by volume. A PPC nanolaser with suitable wavelength was tested using an 830 nm laser diode operating at .5% duty cycle. The PPC laser emission was detected by an optical spectrum analyzer. The water/bead solution

was contained in a small PDMS well which surrounded the PPC substrate. This method was chosen so that a large volume of solution could easily interact with all of the PPC lasers of interest.

The spectral response of the nanolaser was measured as the beads interacted with the cavity through Brownian motion. As can be seen from Figure 48, the wavelength of the cavity shifted between distinct quantized wavelengths. This is due to multiple beads entering and leaving the cavity. The shift that a single 100 nm diameter bead would cause can easily be calculated by analyzing the volumetric index of refraction change. For the sample under test, the volume of the cavity is given by

$$V = \pi r_{def}^2 t \quad 5.1$$

where r_{def} is the radius of the defect and t is the membrane thickness. For the sample under test r_{def} is 165 nm and t is 380 nm which yields a volume of approximately $.0325 \mu\text{m}^3$. A single 100 nm diameter bead has a volume of approximately $.000606 \mu\text{m}^3$. Thus one bead's volume is roughly 2% of the total cavity volume. The total index of refraction for the cavity volume can then be determined as a function of the number of beads and is given by

$$n_{cav} = \left(\frac{N}{N_{total}} n_{bead} \right) + \left(1 - \frac{N}{N_{total}} \right) n_{env} \quad 5.2$$

$$\Delta n_{cav} = n_{cav} - n_{env}$$

where n_{bead} is the index of refraction of the bead, N is the number of beads inside the cavity and N_{total} is the total number of beads that can fit within the cavity. The PPC laser response shown in Figure 48 corresponds to laser R7,C3 discussed previously. The wavelength change induced by the beads can then be calculated

by using the slope and intercept of the line shown for R7,C3 in Figure 47. For the case of R7,C3 the change in wavelength is approximately .08 nm. This is in good agreement with the spectra obtained in Figure 48. The first predicted value is for the cavity immersed in water with a surfactant added. The other predicted values are for one, two, three, four and five beads interacting with the cavity in the water/surfactant solution. Error bars are shown which correlate to approximately 2.5 times the standard deviation of the bead diameter.

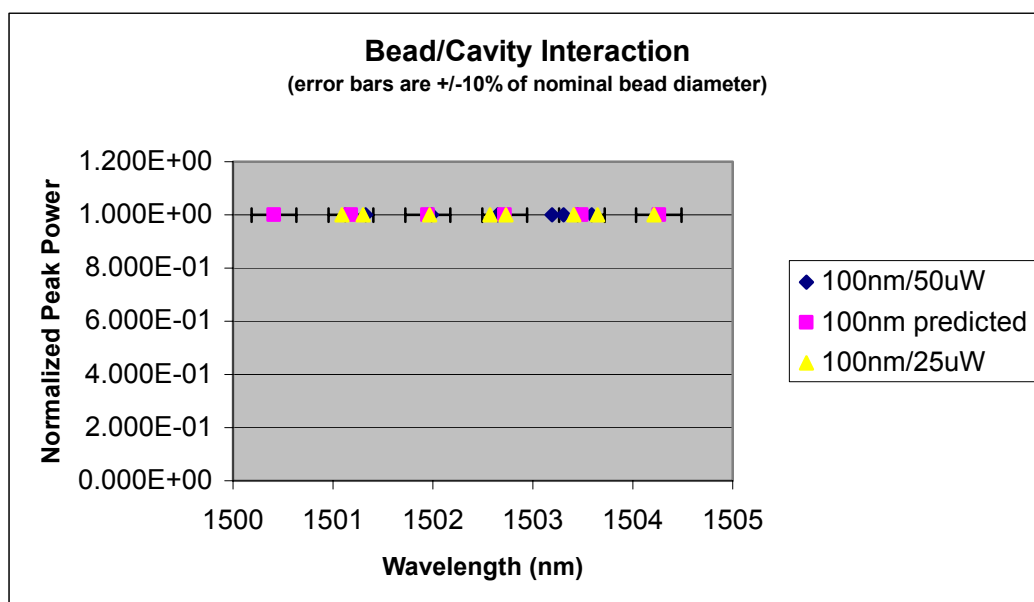


Figure 48. The photoluminescence spectra of PPC laser R7,C3 with 100nm diameter beads in water interfacing with the cavity. The spectra show that the peak wavelength shift is quantized according to the number of beads interacting with the cavity.

Multiphoton Cavity Processes

As discussed earlier, fluorescence is an incredibly valuable tool for identifying biological and chemical species. Single molecule detection is possible

through fluorescence; however, the PPC lasers currently operate in the infrared which makes directly pumping typical visible fluorophores nearly impossible. Although three photon processes such as second harmonic generation are permitted and have some probability of occurring, the wavelength would still be too long for fluorescence pumping. A four-photon process involving third harmonic generation would be needed for direct pumping to occur and the probability of this occurring is miniscule.

A better approach for a four-photon process is to take advantage of specific molecular energy states. Examples such as Coherent anti-Stokes Raman Scattering (CARS) and four wave mixing have been demonstrated in various systems [59]. The process can best be described by the Jablonski diagram shown in Figure 49.

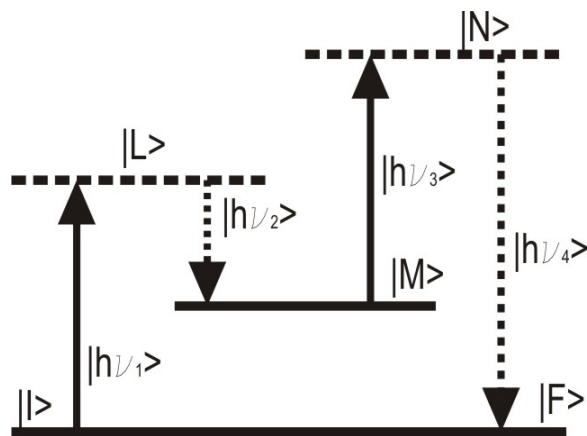


Figure 49. A Jablonski diagram of a four-photon process. The planar photonic crystal laser could supply the necessary energy to pump the molecule into its highest excited state $|N\rangle$.

Since the PPC lasers are normally pumped optically with an 830nm laser diode, this pump laser could supply the necessary energy to excite a molecule into state $|L\rangle$. Once the molecule decays to state $|M\rangle$ either by photon emission or

vibrational energy conversion, the PPC laser could provide the energy for the molecule to be excited into state $|N\rangle$ which would then decay via photon emission back to its ground state. The photon emission described by $h\nu_4$ could readily be detected. For example, the wavelength of the final emitted photon given an 830 nm pump and a 1550 nm PPC laser would typically be around 600 to 650 nm which is of course visible light. Since PPC lasers can be tuned lithographically, a multitude of wavelengths could be achieved granted the right molecule could be found.

In order for this process to occur, an organic molecule which has the necessary energy states must be found. Not only must it be excitable in the near infrared, it must also decay to a stable intermediate state $|M\rangle$ which is stable enough to allow the photonic crystal laser to pump it into state $|N\rangle$. Although the most appropriate molecule has yet to be identified, several candidates do exist. These include infrared dye laser molecules, excimer and exciplexes. This technique could yield another exciting application for PPC lasers once all the pieces have been assembled.

Dense Integration of Laser Sensors

Structures with different defect hole sizes (r_{def}/a) within the same photonic crystal platform have been tested in order to explore the integration of multi-wavelength photonic crystal lasers with lithographically predetermined spectra. These devices are particularly interesting as compact multiwavelength light sources, but are also useful if many reactions have to be monitored at the same

time. Individual reactions can be observed in laser cavities which have predetermined spectral signatures, and optically read by observing changes in the collective spectrum of a multiwavelength laser array. In Figure 50 one can see both the structure and accompanying spectra of three optical cavities fabricated within a common photonic crystal slab with $a=446$ nm and $r=134$ nm. The sizes of the defect holes which define the optical cavities were varied from $r_{\text{small}}=74$ nm, $r_{\text{mid}}=85$ nm and $r_{\text{big}}=97$ nm, and a detailed view of one of the cavities is shown in the inset. The distance between the cavities is 10 lattice periods or $.5 \mu\text{m}$. This distance can be even further reduced (to about $2 \mu\text{m}$) since the radiation of the HQ dipole mode of the cavity is predominantly along y -axis direction [Figure 41 (b)] and therefore the cross-talk between two adjacent cavities is minimal.

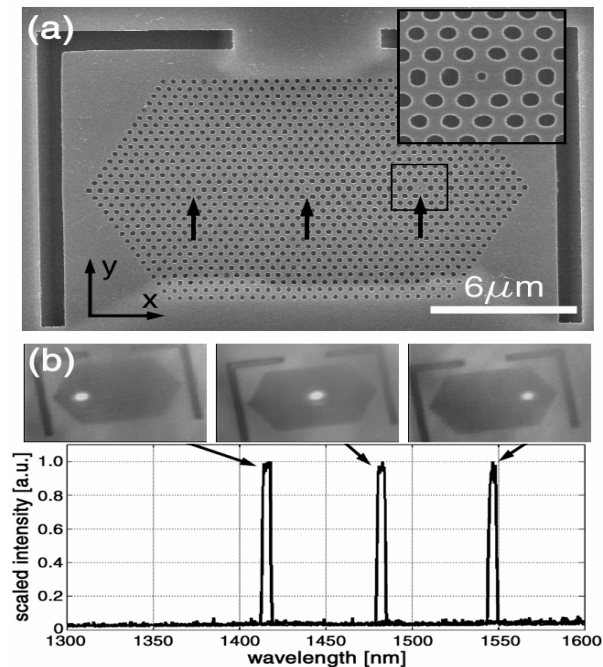


Figure 50. (a) Fabricated structure consists of three cavities integrated within the same photonic crystal mirror. Defect holes are indicated by arrows, and their size increases from

right to left. (b) Resonances detected in each cavity. Mode experience blue-shift as the size of defect hole increases. Positions of pump-beam are shown.

To characterize the highly integrated lasers, cavities were pumped individually, and well-confined spectra were obtained from each of these cavities. The lasing wavelength of the cavities could be tuned from $\lambda=1420$ nm (for r_{big}) to $\lambda=1550$ nm (for r_{small}). It is important to emphasize that the emission from each nanocavity could be observed only when the pump beam was positioned exactly on top of the nanocavity. Even slight variations in the position of the pump beam resulted in turn-off of the laser.

Simultaneous emission from two adjacent nanolasers can also be achieved by de-focusing the pump beam so that the pump spot covers the whole structure shown in Figure 50 (a). The results are shown in Figure 51. Emission from cavities with defect hole radius r_{small} and r_{mid} was detected. As it can be seen, by lithographic tuning the nanocavities and by the choice of pump position, it is possible to achieve simultaneous lasing at two different wavelengths with comparable output powers. By adjusting position of the pump beam one is also able to choose between the two lasers, and enhance the signal from one laser while suppressing the other one. Insets show the near field image of the emitted signal obtained using a NIR camera. This time, pump beam is cut-off with filter (GaAs wafer) and cannot be seen in the image. As expected, the strong emission exists at positions of the nanocavities, only.

The combination of multiple integrated cavities and microfluidics creates a unique chemical sensor. Since the operating wavelength of the PPC lasers can

be lithographically controlled, an array of varying wavelength devices can be created and embedded in a fluidic channel. This system is similar to the CMOS imaging system described earlier except, instead of passive devices combined with lithographically tuned filters, the array of PPC lasers provides active feedback. The laser sensors can be used to provide not only index of refraction measurements, but can also provide absorption spectroscopy information. Since the lasers operate in the infrared many molecules, especially organics, absorb in this wavelength range due to combination bands of the vibrational modes. Through an array of PPC lasers, NIR absorption spectra could yield valuable information about the molecular makeup of an analyte.

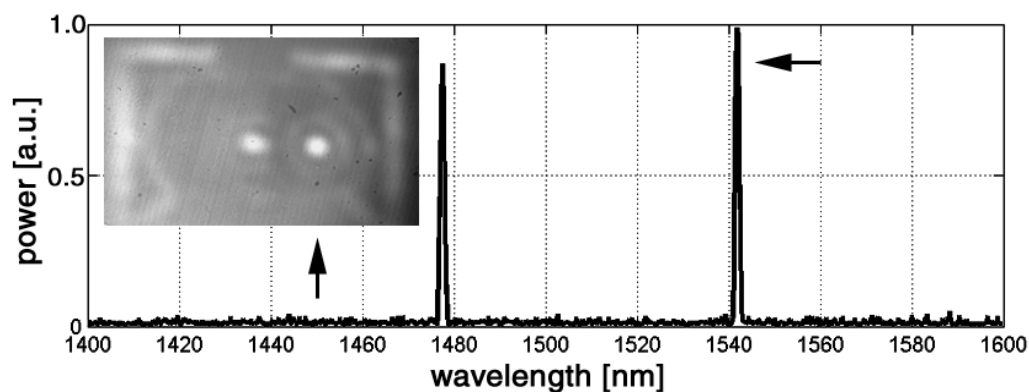


Figure 51. Simultaneous emission from two adjacent nano-lasers pumped simultaneously using big pump spot. Insets show near-field image of the light emitted from nanolasers.

Conclusions

Throughout this thesis, several approaches for optoelectronic integration with microfluidics have been presented and novel microfluidic devices have been discussed. Many of the concepts presented have proven effective and these items can be further applied to other tasks. For instance, the microfluidic diode can form a basic building block of a whole family of new devices. These include a fluidic inverter, fluidic nand gate and fluidic oscillators. All of these devices can be implemented in a single layer of elastomer which could have a tremendous impact on large scale integration of microfluidics. Through this technology, the functionality of microfluidic devices will continue to increase.

With the development of an integrated microfluidic spectroscopy system, the creation of a true lab-on-a-chip is even closer to reality. Although a special CMOS imager was used for most of the experiments, a commercial imager could be used which leads to easy commercialization of a similar system. The combination of an imager, the appropriate filters, microfluidics, and light source allows for the creation of a powerful experimental tool. Not only can one perform spectroscopy, but the system can also be used for imaging the contents of the flow channel. CMOS technology also allows for all the external control electronics and image processing to be combined onto a single die with the imager which would create an incredibly powerful system. Even the current system described previously, is a great step forward in miniaturization and integration.

Although the vertical cavity system described did not function as well as expected, a noticeable enhancement was shown. By combining the multiwavelength graded filter technology with the vertical cavity system, a more sensitive spectroscopy device could be created. Although the system would still be susceptible to detuning, this could be compensated for with special care taken during the measurements. The vertical cavity structure makes for a very interesting device which could be further explored and optimized.

One of the most exciting aspects has to be the fluidic integration of the PPC lasers. The spectroscopic information that can be obtained through this technology is immense. Not only can one gather information based on index of refraction, but even molecular information can also be obtained. Other interesting phenomena can also be studied such as multiphoton generation, optical trapping, and Raman processes. The integration of microfluidics allows for very precise control and regulation of analyte that interacts with the PPC lasers. With further work, a PPC laser membrane may even be placed between two microfluidic channels such that individual molecules can be passed through a photonic crystal.

References

1. Roylance, L.M. and J.B. Angell, *Batch-fabricated silicon accelerometer*. IEEE Trans. Electron. Devices, 1979. 26(12): p. 1911-1917.
2. Yazdi, N., F. Ayazi, and K. Najafi, *Micromachined inertial sensors*. Proc. IEEE, 1998. 86(8): p. 1640-1659.
3. Tufte, O.N., P.W. Chapman, and D. Long, *Silicon diffused-element piezoresistive diaphragms*. J. Appl. Physics, 1962. 33(11): p. 3322.
4. Kuhn, L., E. Bassous, and R. Lane, *Silicon charge electrode array for ink jet printing*. IEEE Trans. Electron. Devices, 1978. 25(10): p. 1257-1260.
5. Lin, L.Y., E.L. Goodstein, and R.W. Tkach, *Free-space micromachined optical switches for optical networking*. IEEE J. Selected Top. Quantum Electron., 1999. 5(1): p. 4-9.
6. Muller, R.S. and K.Y. Lau, *Surface-micromachined microoptical elements and systems*. Proc. IEEE, 1998. 86(8): p. 1705-1720.
7. Hornbeck, L.J. and W.E. Nelson, OSA Tech. Dig. Ser., 1988. 8: p. 107.
8. Harrison, D.J. and e. al., *Micromachining a miniaturized capillary electrophoresis-based chemical-analysis system on a chip*. Science, 1993. 261: p. 895-897.
9. Jacobson, S.C., et al., *High-speed separations on a microchip*. Anal. Chem., 1994. 66(7): p. 1114-1118.
10. Kopp, M.U., A.J.d. Mello, and A. Manz, *Chemical amplification: Continuous-flow PCR on a chip*. Science, 1998. 280: p. 1046-1048.
11. Shoji, S., *Fluids for sensor systems*. Top. Curr. Chem., 1998. 194: p. 163-188.
12. Gravesen, P., J. Branebjerg, and O.S. Jensen, J. Micromech. Microeng., 1993. 3: p. 168.
13. Xi, Y.N. and e. al., *Complex Optical Surfaces Formed by Replica Molding Against Elastomeric Masters*. Science, 1996. 273: p. 347-349.
14. Xia, Y.N. and G.M. Whitesides, *Soft Lithography*. Angew. Chem. Int. Ed. Engl., 1998. 37: p. 550-575.
15. Fu, A.Y., et al., *A microfabricated fluorescence-activated cell sorter*. Nature Biotechnol., 1999. 17: p. 1109-1111.
16. Unger, M.A., et al., *Monolithic microfabricated valves and pumps by multilayer soft lithography*. Science, 2000. 288: p. 113-116.
17. Chou, H., et al., *A microfabricated device for sizing and sorting DNA molecules*. Proc. Natl. Acad. Sci. USA, 1999. 96: p. 11-13.
18. Potter, M.C. and D.C. Wiggert, *Mechanics of Fluids*. Third ed. 2002, Pacific Grove, CA: Brooks/Cole. 863.
19. Kovacs, G., *Micromachine Transducers Sourcebook*. 1998, Palo Alto, CA: WCB/McGraw-Hill. 911.

20. Shoji, S., et al., *A study of a high-pressure micropump for integrated chemical analyzing systems*. Sensors and Actuators A, 1992. 32(1-3): p. 335-339.
21. Seidemann, V., S. Butefisch, and S. Buttgenbach, *Fabrication and investigation of in-plane compliant SU8 structures for MEMS and their application to micro valves and micro grippers*. Sensors and Actuators A, 2002. 97(8): p. 457-461.
22. Seidemann, V., et al., *SU8-micromechanical structures with in-situ fabricated movable parts*. Microsystems Technologies, 2002. 8(4-5): p. 348-350.
23. Hasselbrink, E.F., T.J. Shepodd, and J.E. Rehm, *High-pressure microfluidic control in lab-on-a-chip devices using mobile polymer monoliths*. Anal. Chem., 2002. 74(19): p. 4913-4918.
24. Sim, W.Y., et al., *A phase-change type micropump with aluminum flap valves*. Journal of Micromech. and Microeng., 2003. 13(2): p. 286-294.
25. Hosokawa, K. and R. Maeda, *A pneumatically-actuated three-way microvalve fabricated with polydimethylsiloxane using the membrane transfer technique*. Journal of Micromech. and Microeng., 2000. 10(3): p. 415-420.
26. Heavens, O.S., *Optical Properties of Thin Solid Films*. 1965, New York: Dover. 261.
27. Macleod, H.A., *Thin-film Optical Filters*. third ed. 2001, Tuscon, AZ: Institute of Physics. 641.
28. Yariv, A., *Optical Electronics in Modern Communications*. fifth ed. 1997, Pasadena, CA: Oxford University Press. 744.
29. Yablonovitch, E., *Inhibited spontaneous emission in solid-state physics and electronics*. Phys. Rev. Lett., 1987. 58: p. 2059-2062.
30. Sakoda, K., *Optical Properties of Photonic Crystals*. 2001, Berlin: Springer.
31. John, S., *Strong localization of photons in certain disordered dielectric superlattices*. Phys. Rev. Lett., 1987. 58: p. 2486-2488.
32. Joannopolous, J.D., R.D. Meade, and J.N. Winn, *Photonic Crystals*. 1995, Princeton, New Jersey: Princeton University Press.
33. Jewell, J., J. Harbison, and A. Scherer, *Microlasers*. Scientific American, 1991. 86: p. 56.
34. Cregan, R.F., et al., *Single mode photonic band gap guidance of light in air*. Science, 1999. 285: p. 1537-1539.
35. Cheng, C. and A. Scherer, *Fabrication of photonic band-gap crystals*. J. Vac. Scie. Tech. B., 1995. 13(6): p. 2696-2700.
36. Krauss, T., R. DeLaRue, and S. Brand, *Two-dimensional photonic bandgap structures operating at near infrared wavelengths*. Nature, 1996. 383: p. 699-702.
37. Villeneuve, P., et al., *Three-dimensional photon confinement in photonic crystals of low-dimensional periodicity*. IEEE Proc. Optoe., 1998. 145(6): p. 384-390.

38. Painter, O., et al., *Lithographic tuning of a two-dimensional photonic crystal laser array*. IEEE Phot. Tech. Lett., 2000. 12(9): p. 1126-1128.
39. Vuckovic, J., et al., *Design of photonic crystal microcavities for cavity qed*. Phys. Rev. E, 2002. 6501(1): p. 016608.
40. Loncar, M., A. Scherer, and Y. Qiu, *Photonic crystal laser sources for chemical detection*. Appl. Phys. Lett., 2003. 82: p. 648.
41. Yablonovitch, E., et al., *Donor and acceptor modes in photonic band-structure*. Phys. Rev. Lett., 1991. 67(24): p. 3380-3383.
42. Painter, O., J. Vuckovic, and A. Scherer, *Defect modes of a two-dimensional photonic crystal in an optically thin dielectric slab*. J. Opt. Soc. Am. B, 1999. 16(2): p. 275-285.
43. Vuckovic, J., M. Loncar, and A. Scherer, *Design of photonic crystal optical microcavities*. Proc. SPIE Photonics West Conf., 2001.
44. Vuckovic, J. and Y. Yamamoto, *Photonic crystal microcavities for cavity quantum electrodynamics with a single quantum dot*. Appl. Phys. Lett., 2003. 82(15): p. 2374-2376.
45. Watts, M., et al., *Electromagnetic cavity with arbitrary q and small modal volume without a complete photonic bandgap*. Opt. Lett., 2002. 27(20): p. 1785-1787.
46. Srinivasan, K. and O. Painter, *Momentum space design of high- q photonic crystal optical cavities*. Opt. Exp., 2002. 10: p. 670.
47. Vuckovic, J., et al., *Optimization of the q factor in photonic crystal microcavities*. IEEE J. Quant. El., 2002. 38(7): p. 850-856.
48. Loncar, M., et al., *Low-threshold photonic crystal laser*. Appl. Phys. Lett., 2002. 81(15): p. 2680-2682.
49. Ryu, H., et al., *Square-lattice photonic band-gap single-cell laser operating in the lowest-order whispering gallery mode*. Appl. Phys. Lett., 2002. 80(21): p. 3883-3885.
50. Miyai, E. and K. Sakoda, *Quality factor for localized defect modes in a photonic crystal slab upon a low-index dielectric substrate*. Opt. Lett., 2001. 26(10): p. 740-742.
51. Yoshie, T., et al., *High quality two-dimensional photonic crystal slab cavities*. Appl. Phys. Lett., 2001. 79(26): p. 4289-4291.
52. Johnson, S., et al., *Multipole-cancellation mechanism for high- q cavities in the absence of a complete photonic band gap*. Appl. Phys. Lett., 2001. 78(22): p. 3388-3390.
53. Park, H., et al., *Nondegenerate monopole-mode two-dimensional photonic band gap laser*. Appl. Phys. Lett., 2001. 79(19): p. 3032-3034.
54. Meier, M., et al., *Laser action from two-dimensional distributed feedback in photonic crystals*. Appl. Phys. Lett., 1999. 74(1): p. 7-9.
55. Imada, M., et al., *Coherent two-dimensional lasing action in surface-emitting laser with triangular-lattice photonic crystal structure*. Appl. Phys. Lett., 1999. 75(3): p. 316-318.
56. Notomi, M., H. Suzuki, and T. Tamamura, *Directional lasing oscillation of two-dimensional organic photonic crystal lasers at several photonic band gaps*. Appl. Phys. Lett., 2001. 78(10): p. 1325-1327.

57. Ryu, H., et al., *Very-low threshold photonic band-edge lasers from free-standing triangular photonic crystal slabs*. Appl. Phys. Lett., 2002. 80(19): p. 3476-3478.
58. Noda, S., et al., *Polarization mode control of two-dimensional photonic crystal laser by unit cell structure design*. Science, 2001. 293: p. 1123-1125.
59. Horie, K., H. Ushiki, and F.M. Winnik, *Molecular Photonics Fundamentals and Practical Aspects*. 2000, Weinheim: Kodansha/Wiley-VCH. 204.

Appendix A – FDTD Computer Code

Two sets of code are provided below. The first is the latest set of code that was written to run under the Windows environment. The code was developed using Borland C++ Builder and includes a graphical user interface. Only the critical parts of the code are included here. This includes the discretization algorithm and the calculation routines for solving the FDTD equations. The second set of code is based on the LAM-MPI libraries for distributed computing. The code can be run on any cluster that has LAM-MPI installed. The multi computer code runs under Unix or Linux. However, the interface is all command line driven so the Windows version is much easier to use. The program can be downloaded from my website at no cost. Please visit <http://www.markladams.com/~2Dflow> to download the program.

Windows Code

```
//-----
#include <vcl.h>
#pragma hdrstop

#include "disp.h"
#include "NDabout.h"
#include "NDdist.h"
#include "NDdatagrid.h"
#include "NDstats.h"
#include "NDimage.h"
# include <stdio.h>
# include <time.h>
# include <math.h>
# include <stdlib.h>
# include <stddef.h>
# include <exception.h>
# include <iostream.h>
# include <fstream.h>
# include <dstring.h>

# define MAXGRIDX 1500 /* max number of x nodes */
# define MAXGRIDY 200 /* max number of y nodes */
# define COORDINATOR 0 /* rank of Coordinator */
# define TAG 0
# define true 1
# define false 0

static double start, stop, extime;
```

```

static bool acc, stats, estimate;
static bool distribute, type;
using std::cout;
using std::endl;

AnsiString infilename, outfilename;
ifstream in;
ofstream out;
TFileStream *stream1, *stream2;

//-----
#pragma package(smart_init)
#pragma link "PERFGRAP"
#pragma link "Excel_2K_SRVR"
#pragma resource "*_dfm"
TfrmDiffCalc *frmDiffCalc;
//-----
__fastcall TfrmDiffCalc::TfrmDiffCalc(TComponent* Owner)
: TForm(Owner)
{
    cmbVelProf->ItemIndex = 0;
    acc = false;
    stats = false;
    estimate = false;
}
//-----
void __fastcall TfrmDiffCalc::btnCalcClick(TObject *Sender)
{
    int numIters;
    int gridSizeX, gridSizeY, slugl, slugpos;
    int stripSizeX, numpics, velprof;
    int iters;
    int current = 0, next = 1;          /* current and next grids */
    int gridXext = 0, gridYext = 0, estgridX = 0;
    int x = 0, y = 0, q = 1, n = 0, c = 0;
    int i, j, k;
    float ***grid, *V;
    float mydiff = 0.0, gridval = 0.0, yl = 0.0;
    float a = 0.0, T = 1.0, Vt = 0.0, FS = 0.0; // initialize velocity variables
    bool flowtype = false;
    float dif, inic, vel, time, dx, dy, dt;
    float smax = 0.0, smean = 0.0, sdev = 0.0, sxmean = 0.0; // initialize statistical variables
    int sx = 0, sy = 0;

    start = (float) clock(); // start the timer

    frmDiffCalc->Caption = "Working";
    pgbarCalc->Position = 0;
    pgbarCalc->Smooth = true;
    pgbarCalc->Visible = true;

    // initialize visual objects
    frmDataGrid->Visible = false;
    frmImageDisp->Visible = false;
    frmStatData->sgXmean->Visible = false;
    eExecTime->Visible = false;
    frmImageDisp->Label15->Visible = false;
    Label16->Visible = false;
    frmImageDisp->cmbFrameNo->Visible = false;
    btnGraph->Visible = false;
    frmStatData->sgStats->Visible = false;
    frmStatData->btnPlot->Visible = false;
    frmStatData->cbAllSeries->Visible = false;

    //get parameters
    dif = StrToFloat(eDifVel->Text);
    inic = StrToFloat(eInitConc->Text);
    vel = StrToFloat(eVel->Text);

```

```

time = StrToFloat(eTime->Text);
dx = StrToFloat(eDX->Text);
dy = StrToFloat(eDY->Text);
dt = StrToFloat(eDT->Text);
slugl = ceil(StrToFloat(eSlugL->Text)/dx);
slugpos = ceil(StrToFloat(eSlugP->Text)/dx);
gridSizeX = ceil(StrToFloat(eXGrid->Text)/dx);
gridSizeY = ceil(StrToFloat(eYGrid->Text)/dy);
numpics = StrToInt(eNoPics->Text);
velprof = cmbVelProf->ItemIndex;

// check to see if estimation has been enabled and set value if true
if (estimate) {
    estgridX = slugpos + slugl + (int)(vel*4*time + dif*2*time);
    if (estgridX > gridSizeX) {
        estgridX = gridSizeX;
    }
}
else {
    estgridX = gridSizeX;
}

// initialize combobox for graphing
frmImageDisp->cmbFrameNo->Items->Clear();

for (int zz = 0; zz < numpics; zz++) {
    frmImageDisp->cmbFrameNo->Items->Add(IntToStr(zz));
}

frmImageDisp->cmbFrameNo->ItemIndex = 0;

// initialize all statistical limits for max iterations
frmStatData->sgStats->RowCount = numpics + 1;
frmStatData->sgXmean->ColCount = numpics + 1;
frmStatData->sgXmean->RowCount = gridSizeX + 1;

// hide/show appropriate labels depending on number of events
if (numpics > 1) {
    eEvent->Visible = true;
    Label14->Visible = true;
}
else {
    eEvent->Visible = false;
    Label14->Visible = false;
}

// initialize main calculation parameters
numIters = (int)(time/dt);

pgbarCalc->Min = 0;
pgbarCalc->Max = numIters;

yl = (float)gridSizeY;

frmDataGrid->sgData->RowCount = gridSizeX*(numpics+1);
frmDataGrid->sgData->ColCount = gridSizeY;

/* initialize memory for array allocation */

gridXext = gridSizeX + 2;
gridYext = gridSizeY + 2;

try {
    // TEST FOR EXCEPTIONS.
    grid = new float**[2]; // STEP 1: SET UP THE Current and Next Grid.
    for ( i = 0; i < 2; i++) {
        grid[i] = new float*[gridXext]; // Step 2: Set up the rows
        for ( j = 0; j < gridXext; j++) {
            grid[i][j] = new float[gridYext]; // STEP 2: SET UP THE COLUMNS
        }
    }
}

```

```

    }
    V = new float[gridYext];
}

catch (std::bad_alloc) { // ENTER THIS BLOCK ONLY IF bad_alloc IS THROWN.
// YOU COULD REQUEST OTHER ACTIONS BEFORE TERMINATING
lbleM->Caption = "Could not allocate. Bye ...";
lbleM->Visible = true;
exit(-1);
}

/* initialize velocity matrix */
/* check for plug (0), slug flow (1), sinusoidal flow (2), or peristaltic flow (3) */

switch (velprof) {

    case 0: for (i=0; i < gridSizeY; i++) {
                V[i]=vel;
            }
        a = 0.0;
        flowtype = false;
        break;

    case 1:   for (i=0; i < gridSizeY; i++) {
                V[i]=-vel*(4/(((yl-1)*(yl-1))))*((i)*(i)-(i)*(yl-1)));
            }
        a = 0.0;
        flowtype = false;
        break;

    case 2: for (i=0; i < gridSizeY; i++) {
                V[i]=vel;
            }
        a = 2*M_PI;
        T = (float)StrToFloat(ePeriod->Text);
        flowtype = false;
        break;

    case 3: for (i=0; i < gridSizeY; i++) {
                V[i]=-vel*(4/(((yl-1)*(yl-1))))*((i)*(i)-(i)*(yl-1)));
            }
        a = 0.0;
        T = (float)StrToFloat(ePeriod->Text);
        flowtype = true;
        break;

        default;

    }

/* initialize grids */
for (i = 0; i <= gridSizeX+1; i++) {
    for (j = 0; j <= gridSizeY+1; j++) {
        if ((i >= slugpos) && (i < (slugpos+slugl))) {
            grid[current][i][j] = inic;
        }
        else {
            grid[current][i][j] = 0.0*inic;
        }
        grid[next][i][j] = grid[current][i][j];
    }
}

// solve 2D velocity/diffusion

for (iters = 1; iters <= numIters; iters++) {

//ouput to grid

```

```

if (iters >= (q-1)*numIters/numpics) {
    smax = 0.0;
    smean = 0.0;
    sx = 0;
    sy = 0;
/* print output */
    for (i = 0; i < gridSizeX; i++) {
        frmDataGrid->sgData->Row = (q-1)*gridSizeX + i;
        sxmean = 0.0;
        for (j = 0; j < gridSizeY; j++) {
            frmDataGrid->sgData->Col = j;
            frmDataGrid->sgData->Cells[j][(q-1)*gridSizeX+i] = FloatToStr(grid[current][i][j]);
            if (stats) {
                if (smax <= grid[current][i][j]) {
                    smax = grid[current][i][j];
                    sx = i;
                    sy = j;
                }
                smean = smean + grid[current][i][j];
                sxmean = sxmean + grid[current][i][j];
            }
        }
        if (stats) {
            sxmean = sxmean / gridSizeX;
            frmStatData->sgXmean->Cells[q][0] = IntToStr(q);
            frmStatData->sgXmean->Cells[0][i+1] = IntToStr(i + 1);
            frmStatData->sgXmean->Cells[q][i+1] = FloatToStrF(sxmean, ffGeneral, 8, 3);
        }
    }

    if (stats) {
        smean = (smean / (float) (gridSizeX * gridSizeY));
        frmStatData->sgStats->Cells[0][q] = IntToStr(q);
        frmStatData->sgStats->Cells[1][q] = FloatToStrF(smax, ffGeneral, 8, 3);
        frmStatData->sgStats->Cells[2][q] = IntToStr(sx);
        frmStatData->sgStats->Cells[3][q] = IntToStr(sy);
        frmStatData->sgStats->Cells[4][q] = FloatToStrF(smean, ffGeneral, 8, 3);
        //frmStatData->sgStats->Cells[5][q] = "n/a";
    }
    eEvent->Text = IntToStr(q);
    q++;
}

//Solve FDTD model
if (flowtype) {
    FS = 0.0; //initialize for peristaltic pumping

    /*for (int kk = 1; kk < 32; kk = kk + 2) {
        FS = FS + (1/kk)*(sin(kk*M_PI*iters*dt/T));
    }
    */
    if (fabs(cos(M_PI*iters*dt/T))<=.5) {
        FS = 0.0;
    }
    else {
        FS = 1.0;
    }
}

/* make indexing easier */
n = next;
c = current;

/* update my points */
//lower noflux boundary y-1 = y+1

```

```

        y = 0;
        for (x = 1; x <= estgridX; x++) {
    if (flowtype) {

        //Vt = V[y]*(1/2)*(1 - (4/M_PI)*FS);
        Vt = fabs(V[y])*FS;
    }
    else {
        Vt = fabs(V[y])*cos((a/T)*dt);
    }
    grid[n][x][y] = (dif*dt/(dx*dx))*(grid[c][x+1][y]-2*grid[c][x][y]+grid[c][x-
1][y])+(dif*dt/(dy*dy))*(grid[c][x][y+1]-2*grid[c][x][y]+grid[c][x][y-1])+(-Vt*dt/(2*dx))*(grid[c][x+1][y]-grid[c][x-
1][y])+grid[c][x][y];
    }
    //high noflux boundary y+1 = y-1
    y = gridSizeY-1;
    for (x = 1; x <= estgridX; x++) {
    if (flowtype) {

        //Vt = V[y]*(1/2)*(1 - (4/M_PI)*FS);
        Vt = fabs(V[y])*FS;
    }
    else {
        Vt = fabs(V[y])*cos((a/T)*dt);
    }
    grid[n][x][y] = (dif*dt/(dx*dx))*(grid[c][x+1][y]-2*grid[c][x][y]+grid[c][x-
1][y])+(dif*dt/(dy*dy))*(grid[c][x][y+1]-2*grid[c][x][y]+grid[c][x][y-1])+(-Vt*dt/(2*dx))*(grid[c][x+1][y]-grid[c][x-
1][y])+grid[c][x][y];
    }

    //everything in between
    for (x = 1; x <= estgridX; x++) {
        for (y = 1; y < gridSizeY-1; y++) {
    if (flowtype) {

        //Vt = V[y]*(1/2)*(1 - (4/M_PI)*FS);
        Vt = fabs(V[y])*FS;
    }
    else {
        Vt = fabs(V[y])*cos((a/T)*dt);
    }
    grid[n][x][y] = (dif*dt/(dx*dx))*(grid[c][x+1][y]-2*grid[c][x][y]+grid[c][x-
1][y])+(dif*dt/(dy*dy))*(grid[c][x][y+1]-2*grid[c][x][y]+grid[c][x][y-1])+(-Vt*dt/(2*dx))*(grid[c][x+1][y]-grid[c][x-
1][y])+grid[c][x][y];
    }
        }
    }
    current = next; next = 1-next; /* swap grids */

pgbarCalc->StepBy(1);
}

frmDataGrid->Visible = true;

SaveData1->Enabled = true;
//ExportData1->Enabled = true;

btnGraph->Visible = true;

// display stats
if (stats) {
    frmStatData->sgStats->Visible = true;
    frmStatData->Visible = true;
    //frmStatData->sgXmean->Visible = true;
}

```

```

        /* compute maxdiff */
    if (acc) {
        for (i = 0; i <= gridSizeX; i++) {
            for (j = 0; j <= gridSizeY; j++) {
                gridval = grid[current][i][j] - grid[next][i][j];
                if (gridval < 0.0)
                    gridval = -gridval;
                if (mydiff <= gridval)
                    mydiff = gridval;
            }
        }
        lblMaxDiff->Visible = true;
        eMaxDiff->Visible = true;
        eMaxDiff->Text = FloatToStrF(mydiff, ffGeneral, 5, 8);
    }

    frmDiffCalc->Caption = "2D Flow Simulator";

    stop = (float) clock();
    extime = (stop - start) / CLOCKS_PER_SEC;

    eExecTime->Text = FloatToStr(extime);
    eExecTime->Visible = true;
    Label16->Visible = true;

    //fclose(*OUP);

    delete[] V;

    for (i = 0; i < 2; i++)
        for (j = 0; j < gridXext; j++)
            //for (k = 0; k < gridYext; k++)
                delete[] grid[i][j]; // STEP 2: DELETE THE ROWS
    delete[] grid;

}
//-----

void __fastcall TfrmDiffCalc::Exit1Click(TObject *Sender)
{
    in.close();
    out.close();
    Close();
}
//-----

void __fastcall TfrmDiffCalc::btnGraphClick(TObject *Sender)
{
    float maxval;
    int rc = 0, cc = 0;
    int xorg = 0, yorg = 0, x = 0, y = 0, xmax = 800, ymax = 200;
    int picnum = 0, rowstart = 0, numpics = 1;
    int pixcolor = 0;
    float xratio = 0, yratio = 0, xyratio = 0, maxratio = 0, gridSizeX = 0, gridSizeY = 0, dx = 0, dy = 0;

    dx = (float) StrToFloat(eDX->Text);
    dy = (float) StrToFloat(eDY->Text);
    gridSizeX = (float) StrToFloat(eXGrid->Text)/dx;
    gridSizeY = (float) StrToFloat(eYGrid->Text)/dy;
    numpics = StrToInt(eNoPics->Text);

    frmImageDisp->Visible = true;

    if (numpics > 1) {
        frmImageDisp->cmbFrameNo->Visible = true;
        frmImageDisp->Label15->Visible = true;
    }
    else {
        frmImageDisp->cmbFrameNo->Visible = false;

```

```

    frmImageDisp->Label15->Visible = false;
}

picnum = frmImageDisp->cmbFrameNo->ItemIndex;

rc = frmDataGrid->sgData->RowCount;
cc = frmDataGrid->sgData->ColCount;

xorg = 0;
yorg = 0;

xratio = (float)xmax / gridsizeX;
yratio = (float)ymax / gridsizeY;
xyratio = gridsizeY / gridsizeX;
maxratio = (float) ymax / (float) xmax;

if ( xyratio <= maxratio ) {
    xyratio = maxratio;
}

maxval = 0.0;

rowstart = picnum * ceil(gridsizeX);

frmImageDisp->imGraph->Height = ceil(ymax*xyratio);
//imGraph->Repaint();

//find max value for normalization
for (int i = rowstart; i < rowstart + (rc/numpics); i++) {
    for (int j = 0; j < cc; j++) {
        if (maxval < StrToFloat(frmDataGrid->sgData->Cells[j][i])) {
            maxval = StrToFloat(frmDataGrid->sgData->Cells[j][i]);
        }
    }
}

frmImageDisp->imGraph->Canvas->Pen->Color = clWindow;
//imGraph->Canvas->Rectangle(xorg,yorg,xorg+xmax,yorg+(int)(ymax * xyratio) + 1);

for (int i = 0; i < (rc/numpics); i++) {
    for (int j = 0; j < cc; j++) {
        pixcolor = ceil((StrToFloat(frmDataGrid->sgData->Cells[j][i + rowstart])/maxval)*255);
        if (xratio >= 1.0) {
            if (yratio >= 1.0) {
                for (int k = 0; k <= (int)xratio; k++) {
                    for (int l = 0; l <= ceil(yratio * xyratio); l++) {
                        x = xorg + ceil(i*xratio) + k;
                        y = yorg + ceil(j * yratio * xyratio) + l;
                        frmImageDisp->imGraph->Canvas->Pixels[x][y] = (Graphics::TColor) pixcolor;
                    }
                }
            }
            else {
                for (int k = 0; k <= ceil(xratio); k++) {
                    for (int l = 0; l <= ceil(yratio); l++) {
                        x = xorg + ceil(i * xratio) + k;
                        y = yorg + ceil(j * yratio) + l;
                        frmImageDisp->imGraph->Canvas->Pixels[x][y] = (Graphics::TColor) pixcolor;
                    }
                }
            }
        }
        else {
            if (yratio >= 1.0) {
                x = xorg + ceil(i*xratio);
                for (int l = 0; l <= ceil(yratio * xyratio); l++) {
                    y = yorg + ceil(j * yratio * xyratio) + l;
                    frmImageDisp->imGraph->Canvas->Pixels[x][y] = (Graphics::TColor) pixcolor;
                }
            }
        }
    }
}

```

```

        else {
            x = xorg + i*ceil(xratio);
            for (int l = 0; l <= ceil(yratio); l++) {
                y = yorg + ceil(j * yratio) + l;
                frmImageDisp->imGraph->Canvas->Pixels[x][y] = (Graphics::TColor) pixcolor;
            }
        }
    }
}

SaveImage1->Enabled = true;

//Canvas->Brush->Color = clBtnFace;
//Canvas->Font->Name = "Arial";
//Canvas->TextOut( Canvas->PenPos.x, Canvas->PenPos.y,"This is the end of the line" );

}
//-----

void __fastcall TfrmDiffCalc::Open1Click(TObject *Sender)
{
    float temp;

    //OpenFile->InitialDir="C:\\Documents and Settings\\Mark L. Adams\\My Documents\\";

    if(OpenFile->Execute()){
        infilename = OpenFile->FileName;
    }
    in.open(infilename.c_str());
    if (in.fail() ) {
        lblEM->Caption = "File could not be opened.";
        lblEM->Visible = true;
    }

    in >> temp;
    eDifVel->Text = FloatToStr(temp);
    in >> temp;
    eInitConc->Text = FloatToStr(temp);
    in >> temp;
    eVel->Text = FloatToStr(temp);
    in >> temp;
    eXGrid->Text = FloatToStr(temp);
    in >> temp;
    eYGrid->Text = FloatToStr(temp);
    in >> temp;
    eTime->Text = FloatToStr(temp);
    in >> temp;
    eDX->Text = FloatToStr(temp);
    in >> temp;
    eDY->Text = FloatToStr(temp);
    in >> temp;
    eDT->Text = FloatToStr(temp);
    in >> temp;
    eSlugL->Text = FloatToStr(temp);
    in >> temp;
    eSlugP->Text = FloatToStr(temp);
    in >> temp;
    eNoPics->Text = FloatToStr(temp);

    in.close();
}
//-----

void __fastcall TfrmDiffCalc::SaveData1Click(TObject *Sender)
{
    int rc = 0, cc = 0;

```

```

int numpics = 0;

//SaveFile->InitialDir = "C:\\Documents and Settings\\Mark L. Adams\\My Documents\\";
//SaveImage->FileName = infilename;

if(SaveFile->Execute()){
    outfilename = SaveFile->FileName + ".txt";
}

out.open(outfilename.c_str(),ios::out);

if (out.fail() ) {
    lblEM->Caption = "File could not be opened.";
    lblEM->Visible = true;
}

numpics = StrToInt(eNoPics->Text);

rc = frmDataGrid->sgData->RowCount;
cc = frmDataGrid->sgData->ColCount;

for (int i = 0; i < rc; i++) {
    for (int j = 0; j < cc; j++) {
        out << frmDataGrid->sgData->Cells[j][i].c_str();
        out << '\t';
    }
    out << '\n';
}

out.close();

}
//-----

void __fastcall TfrmDiffCalc::SaveParms1Click(TObject *Sender)
{
    SaveFile->InitialDir = "C:\\Documents and Settings\\Mark L. Adams\\My Documents\\";
    //SaveImage->FileName = infilename;

    if(SaveFile->Execute()){
        outfilename = SaveFile->FileName + ".txt";
    }

    out.open(outfilename.c_str(),ios::out);
    if (out.fail() ) {
        lblEM->Caption = "File could not be opened.";
        lblEM->Visible = true;
    }

    out << eDifVel->Text.c_str();
    out << '\n';
    out << eInitConc->Text.c_str();
    out << '\n';
    out << eVel->Text.c_str();
    out << '\n';
    out << eXGrid->Text.c_str();
    out << '\n';
    out << eYGrid->Text.c_str();
    out << '\n';
    out << eTime->Text.c_str();
    out << '\n';
    out << eDX->Text.c_str();
    out << '\n';
    out << eDY->Text.c_str();
    out << '\n';
    out << eDT->Text.c_str();
    out << '\n';
    out << eSlugL->Text.c_str();
    out << '\n';
}

```

```

out << eSlugP->Text.c_str();
out << '\n';
out << eNoPics->Text.c_str();
out << '\n';
out << cmbVelProf->Text.c_str();

out.close();
}
//-----

void __fastcall TfrmDiffCalc::EnableAccuracy1Click(TObject *Sender)
{
    if (!acc) {
        acc = true;
        EnableAccuracy1->Caption = "Disable &Accuracy";
    }
    else {
        acc = false;
        EnableAccuracy1->Caption = "Enable &Accuracy";
        lblMaxDiff->Visible = false;
        eMaxDiff->Visible = false;
    }
}
//-----

void __fastcall TfrmDiffCalc::About1Click(TObject *Sender)
{
    frmAbout->Visible = true;
}
//-----

void __fastcall TfrmDiffCalc::EnableStatistics1Click(TObject *Sender)
{
    if (!stats) {
        stats = true;
        EnableStatistics1->Caption = "&Disable Statistics";
        frmStatData->sgStats->Cells[0][0] = "Frame No";
        frmStatData->sgStats->Cells[1][0] = "Max Value";
        frmStatData->sgStats->Cells[2][0] = "Max X Pos";
        frmStatData->sgStats->Cells[3][0] = "Max Y Pos";
        frmStatData->sgStats->Cells[4][0] = "Mean";
        //frmStatData->sgStats->Cells[5][0] = "Std. Dev.";
        frmStatData->sgXmean->Cells[0][0] = "X Pos";
        SaveMean1->Enabled = true;
        //ExportMean1->Enabled = true;
    }
    else {
        stats = false;
        EnableStatistics1->Caption = "&Enable Statistics";
        frmStatData->Visible = false;
        frmStatData->sgXmean->Visible = false;
        frmStatData->sgStats->Visible = false;
        frmStatData->btnPlot->Visible = false;
        SaveMean1->Enabled = false;
        //ExportMean1->Enabled = false;
    }
}
//-----

void __fastcall TfrmDiffCalc::cmbVelProfChange(TObject *Sender)
{
    if (cmbVelProf->ItemIndex >= 2) {
        Label17->Visible = true;
        ePeriod->Visible = true;
    }
    else {
        Label17->Visible = false;
    }
}

```

```

        ePeriod->Visible = false;
    }
}
//-----

void __fastcall TfrmDiffCalc::SaveMean1Click(TObject *Sender)
{
    int rc = 0, cc = 0;

    //SaveFile->InitialDir = "C:\\Documents and Settings\\Mark L. Adams\\My Documents\\";
    //SaveImage->FileName = infilename;

    if(SaveFile->Execute()){
        outfilename = SaveFile->FileName + ".txt";
    }

    out.open(outfilename.c_str(),ios::out);

    if (out.fail() ) {
        lblEM->Caption = "File could not be opened.";
        lblEM->Visible = true;
    }

    rc = frmStatData->sgXmean->RowCount;
    cc = frmStatData->sgXmean->ColCount;

    for (int i = 1; i < rc; i++) {
        for (int j = 1; j < cc; j++) {
            out << frmStatData->sgXmean->Cells[j][i].c_str();
            out << '\t';
        }
        out << '\n';
    }

    out.close();
}
//-----

void __fastcall TfrmDiffCalc::SaveImage1Click(TObject *Sender)
{
    if(SavePicture->Execute()){
        outfilename = SavePicture->FileName + ".bmp";
        frmImageDisp->imGraph->Picture->SaveToFile(outfilename);
    }
}
//-----

void __fastcall TfrmDiffCalc::Copy1Click(TObject *Sender)
{
    AnsiString tmpstr = "";
    redCopy->Clear();

    for (int i = 1; i < frmDataGrid->sgData->RowCount; i++) {
        tmpstr = "";
        for (int j = 1; j < frmDataGrid->sgData->ColCount; j++) {
            tmpstr = tmpstr + frmDataGrid->sgData->Cells[j][i] + ",";
        }
        redCopy->Lines->Add(tmpstr);
    }
}
//-----

```

```

void __fastcall TfrmDiffCalc::Copy2Click(TObject *Sender)
{
    AnsiString tmpstr = "";
    redCopy->Clear();

    for (int i = 1; i < frmStatData->sgXmean->RowCount; i++) {
        tmpstr = "";
        for (int j = 1; j < frmStatData->sgXmean->ColCount; j++) {
            tmpstr = tmpstr + frmStatData->sgXmean->Cells[j][i] + ",";
        }
        redCopy->Lines->Add(tmpstr);
    }
}
//-----

void __fastcall TfrmDiffCalc::ExportData1Click(TObject *Sender)
{
    Copy1Click(frmDiffCalc);
    redCopy->SelectAll();
    redCopy->CopyToClipboard();
}
//-----

void __fastcall TfrmDiffCalc::ExportMean1Click(TObject *Sender)
{
    Copy2Click(frmDiffCalc);
    redCopy->SelectAll();
    redCopy->CopyToClipboard();
}
//-----

void __fastcall TfrmDiffCalc::EnblEstClick(TObject *Sender)
{
    if (!estimate) {
        estimate = true;
        EnblEst->Caption = "Disable &Estimation";
    }
    else {
        estimate = false;
        EnblEst->Caption = "Enable &Estimation";
    }
}
//-----

void __fastcall TfrmDiffCalc::Distribute1Click(TObject *Sender)
{
    if (!distribute) {
        distribute = true;
        Distribute1->Caption = "&Disable Distribution";
        frmDist->Visible = true;
    }
    else {
        distribute = false;
        Distribute1->Caption = "&Distribute";
        ServerSocket1->Close();
        ClientSocket1->Close();
    }
}
//-----

```

MPI Code

```

/*
 * Dispersion in tube with laminar flow velocity profile solved with Jacobi
 * iteration on LAM/MPI
 *
 * INPUT: Filename, diffusion constant, initial concentration,
 *        max velocity, length of tube, width of tube, simulation
 *        time, step size x-dir, step size y-dir, timestep, slug length
 *        No. events saved
 * OUTPUT: approximation w to y at the (N+1) values of t.
 */

#include <mpi.h>
#include <stdio.h>
#include <time.h>
#include <math.h>
#include <stdlib.h>
#include <stddef.h>
#define MAXGRIDX 1500 /* max number of x nodes */
#define MAXGRIDY 200 /* max number of y nodes */
#define COORDINATOR 0 /* rank of Coordinator */
#define TAG 0
#define true 1
#define false 0

static void Coordinator(int, int, int, int, int, double, double, double, double, double, double, int, int, double, int);
static void Worker(int, int, int, int, int, double, double, double, double, double, double, int, int, int, int);
static double start, stop, extime;

int main(int argc, char *argv[]) {
    int myid, numIters;
    int numWorkers, gridSizeX, gridSizeY, slugl, slugpos;
    int stripSizeX, numpics, velprof;
    double dif, inic, vel, time, dx, dy, dt;

    start = (double) clock();

    MPI_Init(&argc, &argv); /* initialize MPI */
    MPI_Comm_rank(MPI_COMM_WORLD, &myid);
    MPI_Comm_size(MPI_COMM_WORLD, &numWorkers);
    numWorkers--; /* one coordinator rest are workers */

    /* read command line arguments; assume gridSize is a multiple of numWorkers */
    dif = (double)atoi(argv[1]);
    inic = (double)atoi(argv[2]);
    vel = (double)atoi(argv[3]);
    gridSizeX = atoi(argv[4]);
    gridSizeY = atoi(argv[5]);
    time = ((double)atoi(argv[6]))/1000.0;
    dx = ((double)atoi(argv[7]))/1000.0;
    dy = ((double)atoi(argv[8]))/1000.0;
    dt = ((double)atoi(argv[9]))/1000000.0;
    slugl = atoi(argv[10]);
    slugpos = atoi(argv[11]);
    numpics = atoi(argv[12]);
    velprof = atoi(argv[13]);

    numIters = (int)(time/dt);
    stripSizeX = gridSizeX/numWorkers;

    if (myid == COORDINATOR)
        Coordinator(numWorkers, stripSizeX, gridSizeX, gridSizeY, numpics, dif, inic, vel, dx, dy, dt, slugl,
        slugpos, time, numIters);
    else
        Worker(myid, numWorkers, stripSizeX, gridSizeX, gridSizeY, dif, inic, vel, dx, dy, dt, slugl,
        slugpos, numpics, numIters, velprof);
}

```

```

    MPI_Finalize();
}

static void Coordinator(int numWorkers, int stripSizeX, int gridSizeX, int gridSizeY, int numpics, double dif, double inic,
double vel, double dx,
double dy, double dt, int slugl, int slugpos, double time, int numIters) {
    double *grid;
    double mydiff = 0.0, maxdiff = 0.0;
    int i, j, k, worker, startrow = 0, endrow = 0;
    int gridXext = 0, gridYext = 0;
    MPI_Status status;
    FILE *OUP[1];

    *OUP = fopen("data.txt", "w");

    printf("Nodes in X: %d\nNodes in Y: %d\nInitial Concentration: %6.3lf\nDiffusion Constant: %6.3lf\nInitial
Velocity: %6.3lf\ndx: %6.3lf\ndy:
%6.3lf\ndt: %6.6lf\nSlug length: %d\nSlug Position: %d\nEvents saved: %d\nSimulation time: %6.6lf\nNum of iterations:
%d\nStrip size: %d\nNumber of
workers: %d\n\n", gridSizeX, gridSizeY, inic, dif, vel, dx, dy, dt, slugl, slugpos, numpics, time, numIters, stripSizeX,
numWorkers);

    /* initialize memory for array allocation */

    gridXext = gridSizeX + 2;
    gridYext = gridSizeY + 2;

    grid = new double[gridXext*gridYext];

    /* get grid values from workers */

    for (k = 0; k < numpics; k++) {
        for (worker = 1; worker <= numWorkers; worker++) {
            startrow = (worker-1)*stripSizeX + 1;
            endrow = startrow + stripSizeX - 1;
            for (i = startrow - 1; i < endrow; i++) {
                MPI_Recv(&grid[(i)*(gridSizeY)], gridSizeY+1, MPI_DOUBLE, worker,
TAG, MPI_COMM_WORLD, &status);
            }
            /* print output */
            for (i = 0; i < gridSizeX; i++) {
                for (j = 0; j < gridSizeY; j++) {
                    fprintf(*OUP, "%12.8lf\t", grid[i*gridSizeY+j]);
                }
                fprintf(*OUP, "\n");
            }
            fprintf(*OUP, "\n");
        }
        printf("Event number %d is complete\n",k);
    }
    fclose(*OUP);

    /* reduce differences from Workers */
    MPI_Reduce(&mydiff, &maxdiff, 1, MPI_DOUBLE, MPI_MAX, COORDINATOR, MPI_COMM_WORLD);
    stop = (double) clock();
    extime = (double) (stop - start) / CLOCKS_PER_SEC;
    printf("The maximum difference is %12.6f\nThe execution time is %12.6f\n",maxdiff,extime);

    delete [] grid;
}

static void Worker(int myid, int numWorkers, int stripSizeX, int gridSizeX, int gridSizeY, double dif, double inic, double
vel, double dx, double dy,
double dt, int slugl, int slugpos, int numpics, int numIters, int velprof) {
    double *grid, *V;
    double mydiff = 0.0, maxdiff = 0.0, gridval = 0.0, yl = 0.0;
    int i, j, iters, startrow = 0, endrow = 0;
    int current = 0, next = 1; /* current and next grids */
    int left, right; /* neighboring workers */
    int gridXext = 0, gridYext = 0;

```

```

int x = 0, y = 0, q = 1, n = 0, c = 0;
MPI_Status status;

yl = (double)gridSizeY;

/* initialize memory for array allocation */

gridXext = gridSizeX + 2;
gridYext = gridSizeY + 2;

grid = new double[2*gridXext*gridYext];
V = new double[gridYext];

/* initialize velocity matrix */
/* check for plug (0) or slug flow (1) */

switch (velprof) {

    case 0: for (i=0; i <= gridSizeY; i++) {
                V[i]=vel;
            }
            break;

    case 1:   for (i=0; i <= gridSizeY; i++) {
                V[i]=-vel*(4/(((yl-1)*(yl-1)))*((i*(i)-(i)*(yl-1)));
            }
            break;

    default;

}

/* initialize my grids and determine left and right neighbors */
for (i = 0; i <= gridSizeX+1; i++) {
    for (j = 0; j <= gridSizeY+1; j++) {
        if ((i >= slugpos) && (i < (slugpos+slug))) {
            grid[current * gridSizeX * gridSizeY + i * gridSizeY + j] = inic;
        }
        else {
            grid[current * gridSizeX * gridSizeY + i * gridSizeY + j] =
0.0*inic;
        }
        grid[next * gridSizeX * gridSizeY + i * gridSizeY + j] = grid[current *
gridSizeX * gridSizeY + i * gridSizeY + j];
    }
}

left = myid - 1;
if (myid == numWorkers )
    right = 0;
else
    right = myid + 1;

if (myid == 1)
    startrow = (myid - 1)*stripSizeX + 1;
else
    startrow = (myid - 1)*stripSizeX + 1;

endrow = startrow + stripSizeX - 1;
for (iters = 1; iters <= numIters; iters++) {

    /* make indexing easier */
    n = next*gridSizeX*gridSizeY;
    c = current*gridSizeX*gridSizeY;

    /* exchange my boundaries with my neighbors */
    if (right != 0) MPI_Send(&grid[n + endrow * gridSizeY + 0], gridSizeY+1, MPI_DOUBLE, right,
TAG, MPI_COMM_WORLD);
    if (left != 0) MPI_Send(&grid[n + startrow * gridSizeY + 0], gridSizeY+1, MPI_DOUBLE, left,
TAG, MPI_COMM_WORLD);
}

```

```

        if (left != 0) MPI_Recv(&grid[n + (startrow-1) * gridSizeY + 0], gridSizeY+1, MPI_DOUBLE, left,
TAG, MPI_COMM_WORLD, &status);
        if (right != 0) MPI_Recv(&grid[n + (endrow+1) * gridSizeY + 0], gridSizeY+1, MPI_DOUBLE,
right, TAG, MPI_COMM_WORLD, &status);

        /* update my points */
        //lower noflux boundary y-1 = y+1
        y = 0;
        for (x = startrow; x <= endrow; x++) {
            grid[n + x * gridSizeY + y] =
(dif*dt/(dx*dx))*(grid[c + (x+1) * gridSizeY + y]-2*grid[c + x * gridSizeY + y]+grid[c + (x-1) * gridSizeY +
y])+(dif*dt/(dy*dy))*(grid[c + x * gridSizeY + (y+1)]-2*grid[c + x * gridSizeY + y]+grid[c + x * gridSizeY +
(y+1)])+(V[y]*dt/dx)*(-grid[c + x * gridSizeY + y]+grid[c + (x-1) * gridSizeY + y]+grid[c + x * gridSizeY + y]);
        }
        //high noflux boundary y+1 = y-1
        y = gridSizeY;
        for (x = startrow; x <= endrow; x++) {
            grid[n + x * gridSizeY + y] =
(dif*dt/(dx*dx))*(grid[c + (x+1) * gridSizeY + y]-2*grid[c + x * gridSizeY + y]+grid[c + (x-1) * gridSizeY +
y])+(dif*dt/(dy*dy))*(grid[c + x * gridSizeY + (y-1)]-2*grid[c + x * gridSizeY + y]+grid[c + x * gridSizeY + (y-
1)])+(V[y]*dt/dx)*(-grid[c + x * gridSizeY + y]+grid[c + (x-1) * gridSizeY + y]+grid[c + x * gridSizeY + y]);
        }

        //everything in between
        for (x = startrow; x <= endrow; x++) {
            for (y = 1; y < gridSizeY; y++) {
                grid[n + x * gridSizeY + y] =
(dif*dt/(dx*dx))*(grid[c + (x+1) * gridSizeY + y]-2*grid[c + x * gridSizeY + y]+grid[c + (x-1) * gridSizeY +
y])+(dif*dt/(dy*dy))*(grid[c + x * gridSizeY + (y+1)]-2*grid[c + x * gridSizeY + y]+grid[c + x * gridSizeY + (y-
1)])+(V[y]*dt/dx)*(-grid[c + x * gridSizeY + y]+grid[c + (x-1) * gridSizeY + y]+grid[c + x * gridSizeY + y]);
            }
        }

        current = next; next = 1-next; /* swap grids */

        if (iters >= q*numIters/numpics) {

            /* send my rows of grid to the coordinator */
            for (i = startrow; i <= endrow; i++) {
                MPI_Send(&grid[current * gridSizeX * gridSizeY + i * gridSizeY + 0],
gridSizeY+1, MPI_DOUBLE, COORDINATOR, TAG, MPI_COMM_WORLD);
            }
            q++;
        }
    }
    /* compute mydiff */
    for (i = startrow; i <= endrow; i++) {
        for (j = 0; j <= gridSizeY; j++) {
            gridval = grid[current * gridSizeX * gridSizeY + i * gridSizeY + j] - grid[next *
gridSizeX * gridSizeY + i * gridSizeY + j];
            if (gridval < 0.0)
                gridval = -gridval;
            if (mydiff <= gridval)
                mydiff = gridval;
        }
    }
    /* reduce mydiff with coordinator */
    MPI_Reduce(&mydiff, &maxdiff, 1, MPI_DOUBLE, MPI_MAX, COORDINATOR, MPI_COMM_WORLD);

    delete [] grid;
    delete [] V;
}

```

Appendix B – Fabrication Procedures**Poiseuille Flow Molds****100 μm wide by 10 μm high**

| | Flow | Control |
|--------------------|---|--|
| Photoresist Type | SU8-2010 | SU8-2025 |
| Spinning | 500 RPM Spread (8s) 3000 RPM Spin (39s) | 500 RPM Spread (8s) 3400 RPM Spin (40s) |
| Soft Bake | 1 min @ 65°C 3 min @ 95°C 1 min @ 65°C | 2 min @ 65°C 5 min @ 95°C 1 min @ 65°C |
| Exposure | 30s @ 5.6mW/cm ² | 15s @ 5.6mW/cm ² |
| Post Exposure Bake | 1 min @ 65°C 2 min @ 95°C 1 min @ 65°C | 1 min @ 65°C 3 min @ 95°C 1 min @ 65°C |
| Develop | SU-8 Developer – 2 min | SU-8 Developer – 2 min |
| Hard Bake | 2 hrs @ 150°C | 4 hrs @ 150°C |
| | | |
| Photoresist Type | SPR-5740 | |
| Spinning | 2500 RPM Spin (60s) | |
| Soft Bake | 2 min @ 105°C | |
| Exposure | 30s @ 5.6mW/cm ² | |
| Post Exposure Bake | N/A | |
| Develop | 5:1 Water to MF 2401 Developer – 5 min 45s | |
| Hard Bake | 2 hrs @ 140°C | |

50 μm wide by 5 μm high

| | Flow | Control |
|--------------------|--|--|
| Photoresist Type | SU8-2005 | SU8-2025 |
| Spinning | 500 RPM Spread (8s) 3000 RPM Spin (39s) | 500 RPM Spread (8s) 3400 RPM Spin (40s) |
| Soft Bake | 1 min @ 65°C 2 min @ 95°C 1 min @ 65°C | 2 min @ 65°C 5 min @ 95°C 1 min @ 65°C |
| Exposure | 20s @ 5.6mW/cm ² | 15s @ 5.6mW/cm ² |
| Post Exposure Bake | 1 min @ 65°C 2 min @ 95°C 1 min @ 65°C | 1 min @ 65°C 3 min @ 95°C 1 min @ 65°C |
| Develop | SU-8 Developer – 90s | SU-8 Developer – 2 min |
| Hard Bake | 2 hrs @ 150°C | 4 hrs @ 150°C |
| | | |
| Photoresist Type | SPR-5740 | |
| Spinning | 5000 RPM Spin (60s) | |

| | | |
|--------------------|---|--|
| Soft Bake | 1.5 min @ 105°C | |
| Exposure | 30s @ 5.6mW/cm ² | |
| Post Exposure Bake | N/A | |
| Develop | 5:1 Water to MF 2401 Developer – 3 min 30s | |
| Hard Bake | 2 hrs @ 140°C | |

10 μm wide by 1 μm high

| | Flow | Control |
|--------------------|--|--|
| Photoresist Type | 1:1 SU8-2002 to Cyclopentone | SU8-2025 |
| Spinning | 500 RPM Spread (8s) 3000 RPM Spin (39s) | 500 RPM Spread (8s) 3400 RPM Spin (40s) |
| Soft Bake | 1 min @ 65°C 1 min @ 95°C 1 min @ 65°C | 2 min @ 65°C 5 min @ 95°C 1 min @ 65°C |
| Exposure | 10s @ 5.6mW/cm ² | 15s @ 5.6mW/cm ² |
| Post Exposure Bake | 1 min @ 65°C 1 min @ 95°C 1 min @ 65°C | 1 min @ 65°C 3 min @ 95°C 1 min @ 65°C |
| Develop | SU-8 Developer – 40s | SU-8 Developer – 2 min |
| Hard Bake | 2 hrs @ 150°C | 4 hrs @ 150°C |
| | | |
| Photoresist Type | SPR-1813 | |
| Spinning | 5000 RPM Spin (45s) | |
| Soft Bake | 3 min @ 90°C | |
| Exposure | 30s @ 5.6mW/cm ² | |
| Post Exposure Bake | 1 min @ 65°C 2 min @ 95°C 1 min @ 65°C | |
| Develop | 1:3 Water to MF-319 Developer – 4 min | |
| Hard Bake | 3 hrs @ 150°C | |
| | | |
| Photoresist Type | SPR-5740 | |
| Spinning | 2500 RPM Spin (60s) | |
| Soft Bake | 2 min @ 105°C | |
| Exposure | 30s @ 5.6mW/cm ² | |
| Post Exposure Bake | N/A | |
| Develop | 5:1 Water to MF 2401 Developer – 3 min | |
| Hard Bake | 2 hrs @ 140°C | |

Fluidic Diode Mold

| | 2:1 Flap Ratio | 3:1 Flap Ratio |
|--------------------|--|--|
| Photoresist Type | SU8-2010 | SU8-2010 |
| Spinning | 500 RPM Spread (8s) 5000 RPM Spin (44s) | 500 RPM Spread (8s) 5000 RPM Spin (44s) |
| Soft Bake | 1 min @ 65°C 2 min @ 95°C 1 min @ 65°C | 1 min @ 65°C 2 min @ 95°C 1 min @ 65°C |
| Exposure | 10s @ 5.6mW/cm ² | 10s @ 5.6mW/cm ² |
| Post Exposure Bake | 1 min @ 65°C 2 min @ 95°C 1 min @ 65°C | 1 min @ 65°C 2 min @ 95°C 1 min @ 65°C |
| Develop | SU-8 Developer – 2 min | SU-8 Developer – 2 min |
| Hard Bake | N/A | N/A |
| | | |
| Photoresist Type | SU8-2015 | SU8-2025 |
| Spinning | 500 RPM Spread (8s) 2000 RPM Spin (36s) | 500 RPM Spread (8s) 3400 RPM Spin (40s) |
| Soft Bake | 3 min @ 65°C 6 min @ 95°C 1 min @ 65°C | 2 min @ 65°C 5 min @ 95°C 1 min @ 65°C |
| Exposure | 12s @ 5.6mW/cm ² | 15s @ 5.6mW/cm ² |
| Post Exposure Bake | 1 min @ 65°C 3 min @ 95°C 1 min @ 65°C | 1 min @ 65°C 3 min @ 95°C 1 min @ 65°C |
| Develop | SU-8 Developer – 2 min | SU-8 Developer – 2 min |
| Hard Bake | 4 hrs @ 150°C | 4 hrs @ 150°C |

Microfluidic Amplifier

| | Control/Flow | Amplifier |
|--------------------|--|--|
| Photoresist Type | SU8-2015 | SU8-2025 |
| Spinning | 500 RPM Spread (8s) 5000 RPM Spin (46s) | 500 RPM Spread (8s) 2000 RPM Spin (37s) |
| Soft Bake | 1 min @ 65°C 2 min @ 95°C 1 min @ 65°C | 3 min @ 65°C 5 min @ 95°C 1 min @ 65°C |
| Exposure | 10s @ 5.6mW/cm ² | 30s @ 5.6mW/cm ² |
| Post Exposure Bake | 1 min @ 65°C 2 min @ 95°C 1 min @ 65°C | 1 min @ 65°C 3 min @ 95°C 1 min @ 65°C |
| Develop | SU-8 Developer – 2 min | SU-8 Developer – 2 min |
| Hard Bake | N/A | N/A |
| | | |

The amplifier layer is spun onto a silicon wafer which has previously been patterned with KOH to form the inverted pyramid structures as described in Chapter 2.

Appendix C – Computer Model for Vertical Cavity

Mathcad 2001i was used to perform the simulation.

Define Constants

Desired BR Wavelengths (nm):

$$\begin{aligned}\lambda_f &:= 591 \\ \lambda_s &:= 400 \\ \lambda_l &:= 602 \\ \lambda_{ml} &:= 730 \\ \lambda_{ll} &:= 860 \\ \lambda_{vl} &:= 1010\end{aligned}$$

Desired TR Wavelengths (nm):

$$\lambda_{trf} := 591$$

Adjustment Factor for layer thickness:

$$\begin{aligned}f_{ox} &:= 1 \\ f_{ni} &:= 1 \\ f_{si} &:= 1\end{aligned}$$

Incident Angle in radians:

$$\phi_{inc} := 0$$

Substrate Thickness (nm):

$$d_{sub} := 15000$$

PDMS Thickness (nm):

$$\begin{aligned}\iota &:= 25, 25.1.. 35 \quad \text{flow channel membrane thickness (um)} \\ \kappa &:= 5, 5.05.. 15 \quad \text{flow channel height (um)} \\ \sigma &:= 8, 8.05.. 12 \quad \text{sealing membrane thickness (um)}\end{aligned}$$

Convert thickness to nanometers

$$\begin{aligned}dfc(\kappa) &:= \kappa \cdot 10^3 \\ dfsub(\iota, \kappa) &:= \iota \cdot 10^3 - dfc(\kappa) \\ dmem(\sigma) &:= \sigma \cdot 10^3 \\ dpdms &:= 3.5 \cdot 10^6\end{aligned}$$

Define Variables

Wavelength Range (nm):

$$\lambda := 580, 580.01.. 600$$

Refractive Indices:

$$N_{air} := 1$$

$$k_{ox}(\lambda) := 0.00000$$

$$N_{ox}(\lambda) := 1.46 - i \cdot k_{ox}(\lambda)$$

$$k_{ni}(\lambda) := 0.00000$$

$$N_{ni}(\lambda) := 2.05 - i \cdot k_{ni}(\lambda)$$

$$k_{sub}(\lambda) := 0.00000$$

$$N_{sub}(\lambda) := 1.45 - i \cdot k_{sub}(\lambda)$$

$$k_{si}(\lambda) := \text{if}(\lambda > 430, 40.541650040.989484244^{\lambda}, 36794.190680.9739777^{\lambda})$$

$$N_{si}(\lambda) := 3.40 - i \cdot k_{si}(\lambda)$$

$$k_{pdms}(\lambda) := 0.00000$$

$$N_{pdms}(\lambda) := 1.406 - i \cdot k_{pdms}(\lambda)$$

$$\Sigma := 40$$

$$\mu := 591$$

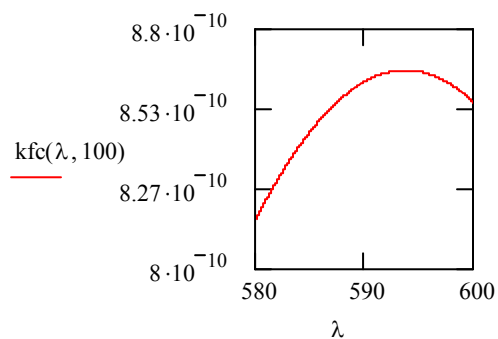
$$\varepsilon := 8 \cdot 10^4 \frac{\text{L}}{\text{mol} \cdot \text{cm}}$$

$$c := 0, 100.. 5 \cdot 10^4$$

$$k_{fc}(\lambda, c) := .18323 \lambda \cdot 10^{-7} \text{cm} \cdot \varepsilon \cdot c \cdot 10^{-9} \frac{\text{mol}}{\text{L}} \cdot \frac{1}{\Sigma \cdot \sqrt{2 \cdot \pi}} \cdot \exp\left[\frac{-(\lambda - \mu)^2}{2 \cdot \Sigma^2}\right]$$

$$n_{fc}(c) := .1 \cdot 10^{-7} \cdot c$$

$$N_{fc}(\lambda, c) := \frac{4}{3} + n_{fc}(c) - i k_{fc}(\lambda, c)$$



Calculate Reflection Bandwidth

$$vf := \frac{1}{\lambda f \cdot 10^{-9}} \cdot 10^{-6}$$

$$vf = 1.692$$

$$vtrf := \frac{1}{\lambda trf \cdot 10^{-9}} \cdot 10^{-6}$$

$$vtrf = 1.692$$

$$v\mu := \frac{1}{\mu \cdot 10^{-9}} \cdot 10^{-6}$$

$$v\mu = 1.692$$

$$\Delta g(\lambda) := \frac{2}{\pi} \cdot \text{asin} \left(\frac{\text{Re}(\text{Nni}(\lambda)) - \text{Nox}(\lambda)}{\text{Re}(\text{Nni}(\lambda)) + \text{Nox}(\lambda)} \right)$$

$$\Delta g(\mu) = 0.108$$

$$\text{BW} := 2 \cdot \Delta g(\mu)$$

$$\text{BW} = 0.215$$

Reflection Bandwidth for 591nm Filter

$$\text{Rl} := \Delta g(\mu) + v\mu$$

$$\text{Rh} := -\Delta g(\mu) + v\mu$$

$$\text{Rl} = 1.8$$

$$\text{Rh} = 1.585$$

$$\text{Rbw} := \left(\frac{\text{Rh} \cdot 10^{-9}}{10^{-6}} \right)^{-1} - \left(\frac{\text{Rl} \cdot 10^{-9}}{10^{-6}} \right)^{-1}$$

$$\text{Rbw} = 75.414$$

Calculate Layer Thickness

Layer Thickness for BR FP Reflectors:

$$d_{box} := \frac{\lambda_f \cdot f_{ox}}{4 \cdot \text{Re}(N_{ox}(\lambda_f))}$$

$$d_{bni} := \frac{\lambda_f \cdot f_{ni}}{4 \cdot \text{Re}(N_{ni}(\lambda_f))}$$

Layer Thickness for BR FP Cavity:

$$d_{cav} := \frac{\lambda_f \cdot f_{ox}}{2 \text{Re}(N_{ox}(\lambda_f))}$$

Layer Thickness for BR LW Filter:

$$d_{lw_{ox}} := \frac{\lambda_l \cdot f_{ox}}{4 \cdot \text{Re}(N_{ox}(\lambda_l))}$$

$$d_{lw_{ni}} := \frac{\lambda_l \cdot f_{ni}}{4 \cdot \text{Re}(N_{ni}(\lambda_l))}$$

Layer Thickness for BR MLW Filter:

$$d_{mlw_{ox}} := \frac{\lambda_{ml} \cdot f_{ox}}{4 \cdot \text{Re}(N_{ox}(\lambda_{ml}))}$$

$$d_{mlw_{ni}} := \frac{\lambda_{ml} \cdot f_{ni}}{4 \cdot \text{Re}(N_{ni}(\lambda_{ml}))}$$

Layer Thickness for BR LLW Filter:

$$d_{llw_{ox}} := \frac{\lambda_{ll} \cdot f_{ox}}{4 \cdot \text{Re}(N_{ox}(\lambda_{ll}))}$$

$$d_{llw_{ni}} := \frac{\lambda_{ll} \cdot f_{ni}}{4 \cdot \text{Re}(N_{ni}(\lambda_{ll}))}$$

Layer Thickness for BR VLW Filter:

$$d_{vlw_{ox}} := \frac{\lambda_{vl} \cdot f_{ox}}{4 \cdot \text{Re}(N_{ox}(\lambda_{vl}))}$$

$$d_{vlw_{ni}} := \frac{\lambda_{vl} \cdot f_{ni}}{4 \cdot \text{Re}(N_{ni}(\lambda_{vl}))}$$

Layer Thickness for BR SW Filter:

$$d_{sw_{ox}} := \frac{\lambda_s \cdot f_{ox}}{4 \cdot \text{Re}(N_{ox}(\lambda_s))}$$

$$d_{sw_{ni}} := \frac{\lambda_s \cdot f_{ni}}{4 \cdot \text{Re}(N_{ni}(\lambda_s))}$$

Layer Thickness for TR FP Reflectors:

$$d_{tox} := \frac{\lambda_{trf} \cdot f_{ox}}{4 \cdot \text{Re}(N_{ox}(\lambda_{trf}))}$$

$$d_{tni} := \frac{\lambda_{trf} \cdot f_{ni}}{4 \cdot \text{Re}(N_{ni}(\lambda_{trf}))}$$

Layer Thickness for TR FP Cavity:

$$d_{cav} := \frac{\lambda_{trf} \cdot f_{ox}}{2 \text{Re}(N_{ox}(\lambda_{trf}))}$$

General Angle Determination

$$\theta(N1, N2, \phi) := \text{asin}\left(\frac{N1}{N2} \cdot \sin(\phi)\right)$$

General Optical Admittance

$$\eta_p(N, \phi) := \frac{N}{\cos(\phi)}$$

$$\eta_s(N, \phi) := N \cdot \cos(\phi)$$

Phase change function

$$\delta(\lambda, n, d, \phi) := \frac{2 \cdot \pi}{\lambda} \cdot n \cdot d \cdot \cos(\phi)$$

Admittance Matrices

Define the incident layer (light is incident on the thick PDMS)

$$d_{inc} := d_{pdms}$$

$$\phi_{pdms}(\lambda) := \theta(N_{air}, N_{pdms}(\lambda), \phi_{inc})$$

$$\phi_{pdms}(\mu) = 0$$

$$\eta_{ipdms}(\lambda) := \eta_p(N_{pdms}(\lambda), \phi_{pdms}(\lambda))$$

$$\eta_{ipdms}(\mu) = 1.406 - i \times 10^{-6}$$

$$\text{Incp}(\lambda) := \begin{bmatrix} \cos(\delta(\lambda, N_{pdms}(\lambda), d_{inc}, \phi_{pdms}(\lambda))) & \frac{(i \cdot \sin(\delta(\lambda, N_{pdms}(\lambda), d_{inc}, \phi_{pdms}(\lambda))))}{\eta_{ipdms}(\lambda)} \\ i \cdot \eta_{ipdms}(\lambda) \cdot \sin(\delta(\lambda, N_{pdms}(\lambda), d_{inc}, \phi_{pdms}(\lambda))) & \cos(\delta(\lambda, N_{pdms}(\lambda), d_{inc}, \phi_{pdms}(\lambda))) \end{bmatrix}$$

Noncavity Structure Model

Define the incident layer for non cavity structure

$$d_{incnc}(\tau, \kappa) := d_{pdms} - d_{sub}(\tau, \kappa)$$

$$\text{Incnep}(\lambda, \tau, \kappa) := \begin{bmatrix} \cos(\delta(\lambda, N_{pdms}(\lambda), d_{incnc}(\tau, \kappa), \phi_{pdms}(\lambda))) & \frac{(i \cdot \sin(\delta(\lambda, N_{pdms}(\lambda), d_{incnc}(\tau, \kappa), \phi_{pdms}(\lambda))))}{\eta_{ipdms}(\lambda)} \\ i \cdot \eta_{ipdms}(\lambda) \cdot \sin(\delta(\lambda, N_{pdms}(\lambda), d_{incnc}(\tau, \kappa), \phi_{pdms}(\lambda))) & \cos(\delta(\lambda, N_{pdms}(\lambda), d_{incnc}(\tau, \kappa), \phi_{pdms}(\lambda))) \end{bmatrix}$$

Calculate Flow Structure / Flow Channel Interface

$$\begin{aligned}\phi_{fsfcnc}(\lambda, c) &:= \theta(N_{pdms}(\lambda), N_{fc}(\lambda, c), \phi_{pdms}(\lambda)) \\ \phi_{fsfcnc}(\mu, 1000) &= 0 \\ \eta_{pfsfcnc}(\lambda, c) &:= \eta_p(N_{fc}(\lambda, c), \phi_{fsfcnc}(\lambda, c)) \\ \eta_{pfsfcnc}(\mu, 1000) &= 1.333 - 8.64i \times 10^{-9} \\ Ifsfcnc(\lambda, c, \kappa) &:= \begin{bmatrix} \cos(\delta(\lambda, N_{fc}(\lambda, c), d_{fc}(\kappa), \phi_{fsfcnc}(\lambda, c))) & \frac{(i \cdot \sin(\delta(\lambda, N_{fc}(\lambda, c), d_{fc}(\kappa), \phi_{fsfcnc}(\lambda, c))))}{\eta_{pfsfcnc}(\lambda, c)} \\ i \cdot \eta_{pfsfcnc}(\lambda, c) \cdot \sin(\delta(\lambda, N_{fc}(\lambda, c), d_{fc}(\kappa), \phi_{fsfcnc}(\lambda, c))) & \cos(\delta(\lambda, N_{fc}(\lambda, c), d_{fc}(\kappa), \phi_{fsfcnc}(\lambda, c))) \end{bmatrix}\end{aligned}$$

Calculate Flow Channel / Substrate Interface

$$\begin{aligned}\phi_{fsubnc}(\lambda, c) &:= \theta(N_{fc}(\lambda, c), N_{sub}(\lambda), \phi_{fsfcnc}(\lambda, c)) \\ \phi_{fsubnc}(\mu, 1000) &= 0 \\ \eta_{pfsubnc}(\lambda, c) &:= \eta_p(N_{sub}(\lambda), \phi_{fsubnc}(\lambda, c)) \\ \eta_{pfsubnc}(\mu, 1000) &= 1.45 - i \times 10^{-6} \\ Ifsubnc(\lambda, c) &:= \begin{bmatrix} \cos(\delta(\lambda, N_{sub}(\lambda), d_{sub}, \phi_{fsubnc}(\lambda, c))) & \frac{(i \cdot \sin(\delta(\lambda, N_{sub}(\lambda), d_{sub}, \phi_{fsubnc}(\lambda, c))))}{\eta_{pfsubnc}(\lambda, c)} \\ i \cdot \eta_{pfsubnc}(\lambda, c) \cdot \sin(\delta(\lambda, N_{sub}(\lambda), d_{sub}, \phi_{fsubnc}(\lambda, c))) & \cos(\delta(\lambda, N_{sub}(\lambda), d_{sub}, \phi_{fsubnc}(\lambda, c))) \end{bmatrix}\end{aligned}$$

Calculate Substrate / Air interface

$$\begin{aligned}\eta_{psanc}(\lambda, c) &:= \eta_p(N_{air}, \phi_{fsubnc}(\lambda, c)) \\ \eta_{pair} &:= \frac{N_{air}}{\cos(\phi_{inc})} \\ Airpnc(\lambda, c) &:= \begin{pmatrix} 1 \\ \eta_{psanc}(\lambda, c) \end{pmatrix}\end{aligned}$$

Calculate Total system Matrix for Noncavity Structure

$$\begin{aligned}M_{pnc}(\lambda, c, t, \kappa) &:= Incncp(\lambda, t, \kappa) \cdot Ifsfcnc(\lambda, c, \kappa) \cdot Ifsubnc(\lambda, c) \cdot Airpnc(\lambda, c) \\ B_{pnc}(\lambda, c, t, \kappa) &:= M_{pnc}(\lambda, c, t, \kappa)_0 \\ C_{pnc}(\lambda, c, t, \kappa) &:= M_{pnc}(\lambda, c, t, \kappa)_1\end{aligned}$$

Calculate Reflectance, Transmittance, Absorptance, Finesse, Potential Transmittance, Phase Shift on Reflectance, and Phase shift on Transmission

$$\begin{aligned}R_{pnc}(\lambda, c, t, \kappa) &:= \frac{(\eta_{pair} \cdot B_{pnc}(\lambda, c, t, \kappa) - C_{pnc}(\lambda, c, t, \kappa)) \cdot \overline{(\eta_{pair} \cdot B_{pnc}(\lambda, c, t, \kappa) - C_{pnc}(\lambda, c, t, \kappa))}}{\eta_{pair} \cdot B_{pnc}(\lambda, c, t, \kappa) + C_{pnc}(\lambda, c, t, \kappa) \cdot \overline{(\eta_{pair} \cdot B_{pnc}(\lambda, c, t, \kappa) + C_{pnc}(\lambda, c, t, \kappa))}} \\ T_{pnc}(\lambda, c, t, \kappa) &:= \frac{4 \cdot \eta_{pair} \cdot \text{Re}(\eta_{psanc}(\lambda, c))}{(\eta_{pair} \cdot B_{pnc}(\lambda, c, t, \kappa) + C_{pnc}(\lambda, c, t, \kappa)) \cdot \overline{(\eta_{pair} \cdot B_{pnc}(\lambda, c, t, \kappa) + C_{pnc}(\lambda, c, t, \kappa))}} \\ A_{pnc}(\lambda, c, t, \kappa) &:= \frac{4 \cdot \eta_{pair} \cdot \text{Re}(B_{pnc}(\lambda, c, t, \kappa) \cdot \overline{C_{pnc}(\lambda, c, t, \kappa)} - \eta_{psanc}(\lambda, c))}{(\eta_{pair} \cdot B_{pnc}(\lambda, c, t, \kappa) + C_{pnc}(\lambda, c, t, \kappa)) \cdot \overline{(\eta_{pair} \cdot B_{pnc}(\lambda, c, t, \kappa) + C_{pnc}(\lambda, c, t, \kappa))}} \\ F_{pnc}(\lambda, c, t, \kappa) &:= \frac{4 \cdot R_{pnc}(\lambda, c, t, \kappa)}{(1 - R_{pnc}(\lambda, c, t, \kappa))^2} \\ \Psi_{pnc}(\lambda, c, t, \kappa) &:= \frac{T_{pnc}(\lambda, c, t, \kappa)}{(1 - R_{pnc}(\lambda, c, t, \kappa))}\end{aligned}$$

$$\begin{aligned}\phi_{\text{pnc}}(\lambda, c, t, \kappa) &:= \text{atan} \left[\frac{\text{Im} \left[\eta_{\text{psanc}}(\lambda, c) \left(\text{Bpnc}(\lambda, c, t, \kappa) \cdot \overline{\text{Cpnc}(\lambda, c, t, \kappa)} - \text{Cpnc}(\lambda, c, t, \kappa) \cdot \overline{\text{Bpnc}(\lambda, c, t, \kappa)} \right) \right]}{\left(\eta_{\text{psanc}}(\lambda, c)^2 \cdot \text{Bpnc}(\lambda, c, t, \kappa) \cdot \overline{\text{Bpnc}(\lambda, c, t, \kappa)} - \text{Cpnc}(\lambda, c, t, \kappa) \cdot \overline{\text{Cpnc}(\lambda, c, t, \kappa)} \right)} \right] \\ \zeta_{\text{pnc}}(\lambda, c, t, \kappa) &:= \text{atan} \left(\frac{-\text{Im}(\eta_{\text{pair}} \cdot \text{Bpnc}(\lambda, c, t, \kappa) + \text{Cpnc}(\lambda, c, t, \kappa))}{\text{Re}(\eta_{\text{pair}} \cdot \text{Bpnc}(\lambda, c, t, \kappa) + \text{Cpnc}(\lambda, c, t, \kappa))} \right)\end{aligned}$$

Veritcal Cavity Model

Calculate the PDMS / Substrate Interface

$$\begin{aligned}\phi_{\text{pdmssub}}(\lambda) &:= \theta(\text{Npdm}(\lambda), \text{Nsub}(\lambda), \phi_{\text{inc}}) \\ \phi_{\text{pdmssub}}(\mu) &= 0 \\ \eta_{\text{pdmssub}}(\lambda) &:= \eta_{\text{p}}(\text{Nsub}(\lambda), \phi_{\text{pdmssub}}(\lambda)) \\ \eta_{\text{pdmssub}}(\mu) &= 1.45 - i \times 10^{-6} \\ \text{Ipdmsub}(\lambda) &:= \begin{bmatrix} \cos(\delta(\lambda, \text{Nsub}(\lambda), \text{dsub}, \phi_{\text{pdmssub}}(\lambda))) & \frac{(i \cdot \sin(\delta(\lambda, \text{Nsub}(\lambda), \text{dsub}, \phi_{\text{pdmssub}}(\lambda))))}{\eta_{\text{pdmssub}}(\lambda)} \\ i \cdot \eta_{\text{pdmssub}}(\lambda) \cdot \sin(\delta(\lambda, \text{Nsub}(\lambda), \text{dsub}, \phi_{\text{pdmssub}}(\lambda))) & \cos(\delta(\lambda, \text{Nsub}(\lambda), \text{dsub}, \phi_{\text{pdmssub}}(\lambda))) \end{bmatrix}\end{aligned}$$

Calculate Top Reflector Parameters

$$\begin{aligned}\phi_{\text{sbni}}(\lambda) &:= \theta(\text{Nsub}(\lambda), \text{Nni}(\lambda), \phi_{\text{pdmssub}}(\lambda)) \\ \phi_{\text{sbni}}(\mu) &= 0 \\ \eta_{\text{psbni}}(\lambda) &:= \eta_{\text{p}}(\text{Nni}(\lambda), \phi_{\text{sbni}}(\lambda)) \\ \eta_{\text{psbni}}(\mu) &= 2.05 - i \times 10^{-6} \\ \text{Htrp}(\lambda) &:= \begin{bmatrix} \cos(\delta(\lambda, \text{Nni}(\lambda), \text{dtni}, \phi_{\text{sbni}}(\lambda))) & \frac{(i \cdot \sin(\delta(\lambda, \text{Nni}(\lambda), \text{dtni}, \phi_{\text{sbni}}(\lambda))))}{\eta_{\text{psbni}}(\lambda)} \\ i \cdot \eta_{\text{psbni}}(\lambda) \cdot \sin(\delta(\lambda, \text{Nni}(\lambda), \text{dtni}, \phi_{\text{sbni}}(\lambda))) & \cos(\delta(\lambda, \text{Nni}(\lambda), \text{dtni}, \phi_{\text{sbni}}(\lambda))) \end{bmatrix} \\ \phi_{\text{sbniiox}}(\lambda) &:= \theta(\text{Nni}(\lambda), \text{Nox}(\lambda), \phi_{\text{sbni}}(\lambda)) \\ \phi_{\text{sbniiox}}(\mu) &= 0 \\ \eta_{\text{psbniiox}}(\lambda) &:= \eta_{\text{p}}(\text{Nox}(\lambda), \phi_{\text{sbniiox}}(\lambda)) \\ \eta_{\text{psbniiox}}(\mu) &= 1.46 - i \times 10^{-6} \\ \text{Ltrp}(\lambda) &:= \begin{bmatrix} \cos(\delta(\lambda, \text{Nox}(\lambda), \text{dtox}, \phi_{\text{sbniiox}}(\lambda))) & \frac{(i \cdot \sin(\delta(\lambda, \text{Nox}(\lambda), \text{dtox}, \phi_{\text{sbniiox}}(\lambda))))}{\eta_{\text{psbniiox}}(\lambda)} \\ i \cdot \eta_{\text{psbniiox}}(\lambda) \cdot \sin(\delta(\lambda, \text{Nox}(\lambda), \text{dtox}, \phi_{\text{sbniiox}}(\lambda))) & \cos(\delta(\lambda, \text{Nox}(\lambda), \text{dtox}, \phi_{\text{sbniiox}}(\lambda))) \end{bmatrix}\end{aligned}$$

For a $\lambda/4$ SiO₂ / Si₃N₄ Bragg stack with a $\lambda/2$ SiO₂ cavity in the middle

$$\text{LLtrp}(\lambda) := \begin{bmatrix} \cos(\delta(\lambda, \text{Nox}(\lambda), \text{dteav}, \phi_{\text{sbniiox}}(\lambda))) & \frac{(i \cdot \sin(\delta(\lambda, \text{Nox}(\lambda), \text{dteav}, \phi_{\text{sbniiox}}(\lambda))))}{\eta_{\text{psbniiox}}(\lambda)} \\ i \cdot \eta_{\text{psbniiox}}(\lambda) \cdot \sin(\delta(\lambda, \text{Nox}(\lambda), \text{dteav}, \phi_{\text{sbniiox}}(\lambda))) & \cos(\delta(\lambda, \text{Nox}(\lambda), \text{dteav}, \phi_{\text{sbniiox}}(\lambda))) \end{bmatrix}$$

Calculate Charateristic Matrix for DHW Filter with Single Stack/Spacer

$$\begin{aligned}\Gamma &:= 6 \text{ pairs of layers} \\ \text{Mtrp}(\lambda) &:= (\text{Htrp}(\lambda) \cdot \text{Ltrp}(\lambda))^\Gamma \cdot \text{Htrp}(\lambda)\end{aligned}$$

$$R_{tr}(\lambda) := \left[\frac{1 - \left(\frac{\text{Re}(N_{ni}(\lambda))}{\text{Re}(N_{ox}(\lambda))} \right)^{2 \cdot \Gamma} \cdot \left(\frac{\text{Re}(N_{ni}(\lambda))^2}{\text{Re}(N_{sub}(\lambda))} \right)}{1 + \left(\frac{\text{Re}(N_{ni}(\lambda))}{\text{Re}(N_{ox}(\lambda))} \right)^{2 \cdot \Gamma} \cdot \left(\frac{\text{Re}(N_{ni}(\lambda))^2}{\text{Re}(N_{sub}(\lambda))} \right)} \right]^2$$

$$R_{tr}(\mu) = 0.977$$

Calculate Top Reflector / PDMS Flow Structure Interface

$$\phi_{nifs}(\lambda) := \theta(N_{ni}(\lambda), N_{pdms}(\lambda), \phi_{sbni}(\lambda))$$

$$\eta_{pnifs}(\lambda) := \eta_p(N_{pdms}(\lambda), \phi_{sbni}(\lambda))$$

$$I_{nifs}(\lambda, \iota, \kappa) := \begin{bmatrix} \cos(\delta(\lambda, N_{pdms}(\lambda), d_{sub}(\iota, \kappa), \phi_{nifs}(\lambda))) & \frac{(i \cdot \sin(\delta(\lambda, N_{pdms}(\lambda), d_{sub}(\iota, \kappa), \phi_{nifs}(\lambda))))}{\eta_{pnifs}(\lambda)} \\ i \cdot \eta_{pnifs}(\lambda) \cdot \sin(\delta(\lambda, N_{pdms}(\lambda), d_{sub}(\iota, \kappa), \phi_{nifs}(\lambda))) & \cos(\delta(\lambda, N_{pdms}(\lambda), d_{sub}(\iota, \kappa), \phi_{nifs}(\lambda))) \end{bmatrix}$$

Calculate Flow Structure / Flow Channel Interface

$$\phi_{fsfc}(\lambda, c) := \theta(N_{pdms}(\lambda), N_{fc}(\lambda, c), \phi_{nifs}(\lambda))$$

$$\phi_{fsfc}(\mu, 1000) = 0$$

$$\eta_{pfsc}(\lambda, c) := \eta_p(N_{fc}(\lambda, c), \phi_{fsfc}(\lambda, c))$$

$$\eta_{pfsc}(\mu, 1000) = 1.333 - 8.64i \times 10^{-9}$$

$$I_{fsfc}(\lambda, c, \kappa) := \begin{bmatrix} \cos(\delta(\lambda, N_{fc}(\lambda, c), d_{fc}(\kappa), \phi_{fsfc}(\lambda, c))) & \frac{(i \cdot \sin(\delta(\lambda, N_{fc}(\lambda, c), d_{fc}(\kappa), \phi_{fsfc}(\lambda, c))))}{\eta_{pfsc}(\lambda, c)} \\ i \cdot \eta_{pfsc}(\lambda, c) \cdot \sin(\delta(\lambda, N_{fc}(\lambda, c), d_{fc}(\kappa), \phi_{fsfc}(\lambda, c))) & \cos(\delta(\lambda, N_{fc}(\lambda, c), d_{fc}(\kappa), \phi_{fsfc}(\lambda, c))) \end{bmatrix}$$

Calculate Flow Channel / Membrane Interface

$$\phi_{fcmen}(\lambda, c) := \theta(N_{fc}(\lambda, c), N_{pdms}(\lambda), \phi_{fsfc}(\lambda, c))$$

$$\eta_{pfcmem}(\lambda, c) := \eta_p(N_{pdms}(\lambda), \phi_{fcmen}(\lambda, c))$$

$$I_{fcmen}(\lambda, c, \sigma) := \begin{bmatrix} \cos(\delta(\lambda, N_{pdms}(\lambda), d_{mem}(\sigma), \phi_{fcmen}(\lambda, c))) & \frac{(i \cdot \sin(\delta(\lambda, N_{pdms}(\lambda), d_{mem}(\sigma), \phi_{fcmen}(\lambda, c))))}{\eta_{pfcmem}(\lambda, c)} \\ i \cdot \eta_{pfcmem}(\lambda, c) \cdot \sin(\delta(\lambda, N_{pdms}(\lambda), d_{mem}(\sigma), \phi_{fcmen}(\lambda, c))) & \cos(\delta(\lambda, N_{pdms}(\lambda), d_{mem}(\sigma), \phi_{fcmen}(\lambda, c))) \end{bmatrix}$$

$$\phi_{pnc}(\mu, 1000, 30, 11.3) = 51.569 \text{deg}$$

Assemble the total flow structure matrix

$$\zeta_{pnc}(\mu, 1000, 30, 11.3) = -34.421 \text{deg}$$

$$M_{fsp}(\lambda, c, \iota, \kappa, \sigma) := I_{nifs}(\lambda, \iota, \kappa) \cdot I_{fsfc}(\lambda, c, \kappa) \cdot I_{fcmen}(\lambda, c, \sigma)$$

Calculate Bottom Reflector Parameters

Calculate Membrane / Nitride interface

$$\begin{aligned} \phi_{\text{memni}}(\lambda, c) &:= \theta(\text{Npdms}(\lambda), \text{Nni}(\lambda), \phi_{\text{cmem}}(\lambda, c)) \\ \phi_{\text{memni}}(\mu, 1000) &= 0 \\ \eta_{\text{pmemni}}(\lambda, c) &:= \eta_{\text{p}}(\text{Nni}(\lambda), \phi_{\text{memni}}(\lambda, c)) \\ \eta_{\text{pmemni}}(\mu, 1000) &= 2.05 - i \times 10^{-6} \end{aligned}$$

$$\text{Hbrp}(\lambda, c) := \begin{bmatrix} \cos(\delta(\lambda, \text{Nni}(\lambda), \text{dbni}, \phi_{\text{memni}}(\lambda, c))) & \frac{(i \cdot \sin(\delta(\lambda, \text{Nni}(\lambda), \text{dbni}, \phi_{\text{memni}}(\lambda, c))))}{\eta_{\text{pmemni}}(\lambda, c)} \\ i \cdot \eta_{\text{pmemni}}(\lambda, c) \cdot \sin(\delta(\lambda, \text{Nni}(\lambda), \text{dbni}, \phi_{\text{memni}}(\lambda, c))) & \cos(\delta(\lambda, \text{Nni}(\lambda), \text{dbni}, \phi_{\text{memni}}(\lambda, c))) \end{bmatrix}$$

Nitride / Oxide Interface

$$\begin{aligned} \phi_{\text{niox}}(\lambda, c) &:= \theta(\text{Nni}(\lambda), \text{Nox}(\lambda), \phi_{\text{memni}}(\lambda, c)) \\ \eta_{\text{pniox}}(\lambda, c) &:= \eta_{\text{p}}(\text{Nox}(\lambda), \phi_{\text{niox}}(\lambda, c)) \end{aligned}$$

$$\text{Lbrp}(\lambda, c) := \begin{bmatrix} \cos(\delta(\lambda, \text{Nox}(\lambda), \text{dbox}, \phi_{\text{niox}}(\lambda, c))) & \frac{(i \cdot \sin(\delta(\lambda, \text{Nox}(\lambda), \text{dbox}, \phi_{\text{niox}}(\lambda, c))))}{\eta_{\text{pniox}}(\lambda, c)} \\ i \cdot \eta_{\text{pniox}}(\lambda, c) \cdot \sin(\delta(\lambda, \text{Nox}(\lambda), \text{dbox}, \phi_{\text{niox}}(\lambda, c))) & \cos(\delta(\lambda, \text{Nox}(\lambda), \text{dbox}, \phi_{\text{niox}}(\lambda, c))) \end{bmatrix}$$

For a $\lambda/4$ SiO_2 / Si_3N_4 Bragg stack with a $\lambda/2$ SiO_2 cavity in the middle

$$\text{LLbrp}(\lambda, c) := \begin{bmatrix} \cos(\delta(\lambda, \text{Nox}(\lambda), \text{dccav}, \phi_{\text{niox}}(\lambda, c))) & \frac{(i \cdot \sin(\delta(\lambda, \text{Nox}(\lambda), \text{dccav}, \phi_{\text{niox}}(\lambda, c))))}{\eta_{\text{pniox}}(\lambda)} \\ i \cdot \eta_{\text{pniox}}(\lambda) \cdot \sin(\delta(\lambda, \text{Nox}(\lambda), \text{dccav}, \phi_{\text{niox}}(\lambda, c))) & \cos(\delta(\lambda, \text{Nox}(\lambda), \text{dccav}, \phi_{\text{niox}}(\lambda, c))) \end{bmatrix}$$

Calculate Characteristic Matrix for DHW Filter with Single Stack/Spacer

$\Gamma := 6$ pairs of layers

$$\text{Mbrp}(\lambda, c) := (\text{Hbrp}(\lambda, c) \cdot \text{Lbrp}(\lambda, c))^{\Gamma} \cdot \text{Hbrp}(\lambda, c)$$

$$\text{Rbr}(\lambda) := \left[\frac{1 - \left(\frac{\text{Re}(\text{Nni}(\lambda))}{\text{Re}(\text{Nox}(\lambda))} \right)^{2\Gamma} \cdot \left(\frac{\text{Re}(\text{Nni}(\lambda))^2}{\text{Re}(\text{Nsub}(\lambda))} \right)}{1 + \left(\frac{\text{Re}(\text{Nni}(\lambda))}{\text{Re}(\text{Nox}(\lambda))} \right)^{2\Gamma} \cdot \left(\frac{\text{Re}(\text{Nni}(\lambda))^2}{\text{Re}(\text{Nsub}(\lambda))} \right)} \right]^2$$

$$\text{Rbr}(\mu) = 0.977$$

Calculate Nitride / Substrate Interface

$$\begin{aligned} \phi_{\text{nisub}}(\lambda, c) &:= \theta(\text{Nni}(\lambda), \text{Nsub}(\lambda), \phi_{\text{memni}}(\lambda, c)) \\ \phi_{\text{nisub}}(\mu, 1000) &= 0 \\ \eta_{\text{pnisub}}(\lambda, c) &:= \eta_{\text{p}}(\text{Nsub}(\lambda), \phi_{\text{nisub}}(\lambda, c)) \\ \eta_{\text{pnisub}}(\mu, 1000) &= 1.45 - i \times 10^{-6} \end{aligned}$$

$$\text{Inisub}(\lambda, c) := \begin{bmatrix} \cos(\delta(\lambda, \text{Nsub}(\lambda), \text{dsub}, \phi_{\text{nisub}}(\lambda, c))) & \frac{(i \cdot \sin(\delta(\lambda, \text{Nsub}(\lambda), \text{dsub}, \phi_{\text{nisub}}(\lambda, c))))}{\eta_{\text{pnisub}}(\lambda, c)} \\ i \cdot \eta_{\text{pnisub}}(\lambda, c) \cdot \sin(\delta(\lambda, \text{Nsub}(\lambda), \text{dsub}, \phi_{\text{nisub}}(\lambda, c))) & \cos(\delta(\lambda, \text{Nsub}(\lambda), \text{dsub}, \phi_{\text{nisub}}(\lambda, c))) \end{bmatrix}$$

Calculate Substrate / Air interface

$$\eta_{psa}(\lambda, c) := \eta_p(\text{Nair}, \phi_{\text{nisub}}(\lambda, c))$$

$$\eta_{\text{pair}} := \frac{\text{Nair}}{\cos(\phi_{\text{inc}})}$$

$$\text{Airp}(\lambda, c) := \begin{pmatrix} 1 \\ \eta_{psa}(\lambda, c) \end{pmatrix}$$

Calculate Total system Matrix for VC structure

$$\text{Mp}(\lambda, c, i, \kappa, \sigma) := \text{Incp}(\lambda) \cdot \text{Ipdmsul}(\lambda) \cdot \text{Mtrp}(\lambda) \cdot \text{Mfsp}(\lambda, c, i, \kappa, \sigma) \cdot \text{Mbrp}(\lambda, c) \cdot \text{Inisubp}(\lambda, c) \cdot \text{Airp}(\lambda, c)$$

$$\text{Bp}(\lambda, c, i, \kappa, \sigma) := \text{Mp}(\lambda, c, i, \kappa, \sigma)_0$$

$$\text{Cp}(\lambda, c, i, \kappa, \sigma) := \text{Mp}(\lambda, c, i, \kappa, \sigma)_1$$

Calculate Reflectance, Transmittance, Absorptance, Finesse, Potential**Transmittance, Phase Shift on Reflectance, and Phase shift on Transmission**

$$\text{Rp}(\lambda, c, i, \kappa, \sigma) := \frac{(\eta_{\text{pair}} \cdot \text{Bp}(\lambda, c, i, \kappa, \sigma) - \text{Cp}(\lambda, c, i, \kappa, \sigma)) \cdot \overline{(\eta_{\text{pair}} \cdot \text{Bp}(\lambda, c, i, \kappa, \sigma) - \text{Cp}(\lambda, c, i, \kappa, \sigma))}}{\eta_{\text{pair}} \cdot \text{Bp}(\lambda, c, i, \kappa, \sigma) + \text{Cp}(\lambda, c, i, \kappa, \sigma) \cdot \overline{(\eta_{\text{pair}} \cdot \text{Bp}(\lambda, c, i, \kappa, \sigma) + \text{Cp}(\lambda, c, i, \kappa, \sigma))}}$$

$$\text{Tp}(\lambda, c, i, \kappa, \sigma) := \frac{4 \eta_{\text{pair}} \cdot \text{Re}(\eta_{psa}(\lambda, c))}{(\eta_{\text{pair}} \cdot \text{Bp}(\lambda, c, i, \kappa, \sigma) + \text{Cp}(\lambda, c, i, \kappa, \sigma)) \cdot \overline{(\eta_{\text{pair}} \cdot \text{Bp}(\lambda, c, i, \kappa, \sigma) + \text{Cp}(\lambda, c, i, \kappa, \sigma))}}$$

$$\text{Ap}(\lambda, c, i, \kappa, \sigma) := \frac{4 \eta_{\text{pair}} \cdot \text{Re}(\text{Bp}(\lambda, c, i, \kappa, \sigma) \cdot \overline{\text{Cp}(\lambda, c, i, \kappa, \sigma)} - \eta_{psa}(\lambda, c))}{(\eta_{\text{pair}} \cdot \text{Bp}(\lambda, c, i, \kappa, \sigma) + \text{Cp}(\lambda, c, i, \kappa, \sigma)) \cdot \overline{(\eta_{\text{pair}} \cdot \text{Bp}(\lambda, c, i, \kappa, \sigma) + \text{Cp}(\lambda, c, i, \kappa, \sigma))}}$$

$$\text{Fp}(\lambda, c, i, \kappa, \sigma) := \frac{4 \text{Rp}(\lambda, c, i, \kappa, \sigma)}{(1 - \text{Rp}(\lambda, c, i, \kappa, \sigma))^2}$$

$$\Psi_p(\lambda, c, i, \kappa, \sigma) := \frac{\text{Tp}(\lambda, c, i, \kappa, \sigma)}{(1 - \text{Rp}(\lambda, c, i, \kappa, \sigma))}$$

$$\phi_p(\lambda, c, i, \kappa, \sigma) := \text{atan} \left[\frac{\text{Im}[\eta_{psa}(\lambda, c) (\text{Bp}(\lambda, c, i, \kappa, \sigma) \cdot \overline{\text{Cp}(\lambda, c, i, \kappa, \sigma)} - \text{Cp}(\lambda, c, i, \kappa, \sigma) \cdot \overline{\text{Bp}(\lambda, c, i, \kappa, \sigma)})]}{(\eta_{psa}(\lambda, c))^2 \cdot \text{Bp}(\lambda, c, i, \kappa, \sigma) \cdot \overline{\text{Bp}(\lambda, c, i, \kappa, \sigma)} - \text{Cp}(\lambda, c, i, \kappa, \sigma) \cdot \overline{\text{Cp}(\lambda, c, i, \kappa, \sigma)}} \right]$$

$$\zeta_p(\lambda, c, i, \kappa, \sigma) := \text{atan} \left(\frac{-\text{Im}(\eta_{\text{pair}} \cdot \text{Bp}(\lambda, c, i, \kappa, \sigma) + \text{Cp}(\lambda, c, i, \kappa, \sigma))}{\text{Re}(\eta_{\text{pair}} \cdot \text{Bp}(\lambda, c, i, \kappa, \sigma) + \text{Cp}(\lambda, c, i, \kappa, \sigma))} \right)$$

For Resonance the phase shift between the top reflector-flow substrate interface and the flow channel-bottom reflector interface must be an integral multiple of π .

for now look only a p polarized light

$$\zeta_{\text{sub}}(\lambda, i, \kappa) := \delta(\lambda, \text{Npdms}(\lambda), \text{dfsub}(i, \kappa), \phi_{\text{nifs}}(\lambda))$$

$$\zeta_{\text{sub}}(\mu, 20, 10) = 149.478 - 1.063i \times 10^{-4}$$

$$\zeta_{\text{sf}}(\lambda, c, \kappa) := \delta(\lambda, \text{Nfc}(\lambda, c), \text{dfc}(\kappa), \phi_{\text{sf}}(\lambda, c))$$

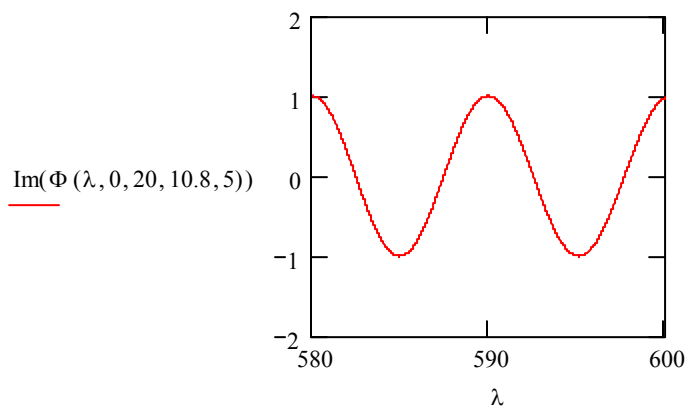
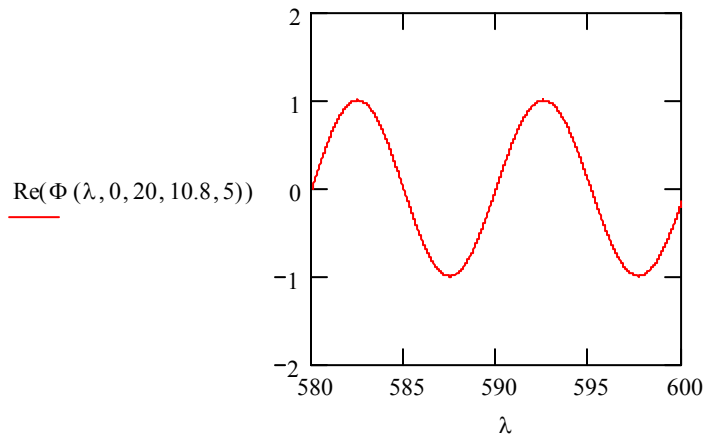
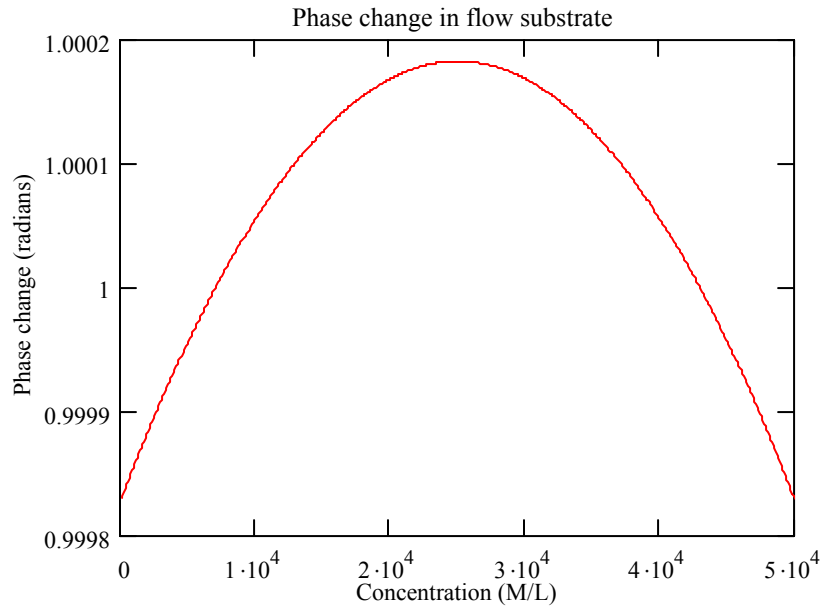
$$\zeta_{\text{sf}}(\mu, 20, 10) = 141.753 - 1.837i \times 10^{-8}$$

$$\zeta_{\text{mem}}(\lambda, c, \sigma) := \delta(\lambda, \text{Npdms}(\lambda), \text{dmem}(\sigma), \phi_{\text{cmem}}(\lambda, c))$$

$$\zeta_{\text{fs}}(\lambda, c, i, \kappa, \sigma) := \zeta_{\text{sub}}(\lambda, i, \kappa) + \zeta_{\text{sf}}(\lambda, c, \kappa) + \zeta_{\text{mem}}(\lambda, c, \sigma)$$

The phase shift for the positive traveling wave is then given by

$$\Phi(\lambda, c, i, \kappa, \sigma) := \exp(i \cdot \zeta_{\text{fs}}(\lambda, c, i, \kappa, \sigma))$$



```

W := | for m ∈ 0..100
      | for n ∈ 0..100
      |   Wm,n ← Tp(580 + m/5, n·100, 25.2, 12.6, 9.5)
      | return W

```

Solve block for determining ideal flow channel parameters

```

S := | j ← 0
      a ← 25
      b ← 5
      c ← 8
      for m ∈ 0..100
        for n ∈ 0..200
          for p ∈ 0..80
            if  $\text{Tp}\left(\mu, 0, \frac{m}{10} + a, \frac{n}{20} + b, \frac{p}{20} + c\right) > .75$ 
              Sj,0 ←  $\frac{m}{10} + a$ 
              Sj,1 ←  $\frac{n}{20} + b$ 
              Sj,2 ←  $\frac{p}{20} + c$ 
              Sj,3 ←  $\text{Im}\left(\Phi\left(\mu, 0, \frac{m}{10} + a, \frac{n}{20} + b, \frac{p}{20} + c\right)\right)$ 
              Sj,4 ←  $\text{Tp}\left(\mu, 0, \frac{m}{10} + a, \frac{n}{20} + b, \frac{p}{20} + c\right)$ 
              j ← j + 1
            return S

```

```

S = ■
xx := 25.2
yy := 12.6
zz := 9.5

```

Appendix D – Imager Maker Code

Imager maker is an application which takes an array of numbers in a text file and converts it into 8 bit and 16 bit bitmap format. The program was created in Borland C++ builder and runs under the Windows operating system. The code is listed below.

```
//-----
#include <vcl.h>

#pragma hdrstop

#include "IMmain.h"
#include "DataDisplay.h"
#include <stddef.h>
#include <exception.h>
//-----
#pragma package(smart_init)
#pragma resource "*.dfm"

#define RED 0
#define GREEN 1
#define BLUE 2

TMainForm *MainForm;
AnsiString infilename, outfilename, fsHex, rawfilename;
ifstream in;
ofstream out, raw;
int height=0,width=0;
unsigned int hval = 0, wval = 0, gridh = 0, gridw = 0, BitsPerPixel = 0;
float maxval=0.0 ,minval=0.0 ,input = 0.0;
float **rawdata;
int count=0, filesize = 0, index=0;
int rawsize = 0;
int bmpsize = 0;
BitmapFileHeader bmfh;
BitmapInfo bmi;
short *rawfiledata;
unsigned char *bmpdata;
unsigned char cbyte;
char inbyte;
TFileStream *stream1, *stream2;
bool stop = false;

//-----
__fastcall TMainForm::TMainForm(TComponent* Owner)
: TForm(Owner)
{
}
//-----

void __fastcall TMainForm::Open1Click(TObject *Sender)
{
    OpenFile->InitialDir=edInitDir->Text;

    if(OpenFile->Execute()){
        infilename = OpenFile->FileName;
    }
    in.open(infilename.c_str());
}
```

```

if (in.fail()) {
    //open failed
    stop = true;
}

Open1->Visible = false;
Close1->Visible = true;

in >> noskipws;

in >> height;
in >> inbyte >> inbyte >> inbyte;
in >> width;
in >> inbyte >> inbyte;

IHval->Text = IntToStr((int)height);
IWval->Text = IntToStr((int)width);

hval = StrToInt(IHval->Text);
wval = StrToInt(IWval->Text);

rawsize = hval*wval;
bmpsize = rawsize*3;

try {
    // TEST FOR EXCEPTIONS.
    rawdata = new float*[hval]; // Step 2: Set up the rows
    for (int j = 0; j < wval; j++) {
        rawdata[j] = new float[wval]; // STEP 2: SET UP THE COLUMNS
    }
    rawfiledata = new short[rawsize];
    bmpdata = new unsigned char[bmpsize];

}

catch (std::bad_alloc) { // ENTER THIS BLOCK ONLY IF bad_alloc IS THROWN.
    // YOU COULD REQUEST OTHER ACTIONS BEFORE TERMINATING
    //lblEM->Caption = "Could not allocate. Bye ...";
    //lblEM->Visible = true;
    exit(-1);
}

MainForm->Caption = "Loading Data...Please Wait";

gridh = hval;
gridw = wval;

for (int i = 0; i < hval; i++) {
    for (int j = 0; j < wval; j++){
        in >> rawdata[i][j];
        in >> inbyte;
    }
    //in >> input;
}

for (int i = 0; i < gridh; i++) {
    DataTable->DataGrid->Row = i;

    for (int j = 0; j < gridw; j++) {

        DataTable->DataGrid->Col = j;
        DataTable->DataGrid->Cells[j][i] = FloatToStrF(rawdata[i][j],2,7,3);
    }
}

```

```

    MainForm->Caption = "Image Maker";
    ConvertFile->Visible = true;
    DataTable->Visible = true;
    in.close();
}
//-----

void __fastcall TMainForm::Exit1Click(TObject *Sender)
{
    in.close();
    out.close();
    raw.close();
    Close();
}
//-----

void __fastcall TMainForm::ConvertFileClick(TObject *Sender)
{
    index = 0;
    BitsPerPixel = StrToInt(BitsPerPix->Text);
    filesize = ((hval*wval*(BitsPerPixel/8))+54);
    fsHex = IntToHex(filesize,6);

    bmfh.type = 'BM';
    bmfh.size = filesize;
    bmfh.reserved1 = 0;
    bmfh.reserved2 = 0;
    bmfh.offset = 54;

    bmi.header.size = 40;
    bmi.header.width = (long)wval;
    bmi.header.height = (long)hval;
    bmi.header.planes = 1;
    bmi.header.bitcount = BitsPerPixel;
    bmi.header.compression = 0;
    bmi.header.imagesize = 0;
    bmi.header.xpixmap = 185729024;
    bmi.header.ypixmap = 185729024;
    bmi.header.colorsused = 16777216;
    bmi.header.colorsimportant = 16777216;

    MainForm->Caption = "Converting File...Please Wait";

    for (int i = 0; i < hval; i++) {
        for (int j = 0; j < wval; j++) {
            maxval = max(maxval,rawdata[i][j]);
            minval = min(minval,rawdata[i][j]);
        }
    }

    for (int i = 0; i < hval; i++) {
        for (int j = 0; j < wval; j++) {
            rawdata[i][j] = (256.0*rawdata[i][j])/maxval;
        }
    }

    MaxVal->Text = FloatToStr(maxval);
    MinVal->Text = FloatToStr(minval);
    count = 0;

    for (int i = 0; i < hval; i++) {
        for (int j = 0; j < wval; j++) {
            for (int c = 0; c < 256; c++) {
                if ((rawdata[i][j]>=c)&&(rawdata[i][j]< (c+1)))
                {
                    bmpdata[count] = c;
                    count++;
                    bmpdata[count] = c;
                    count++;
                    bmpdata[count] = c;
                }
            }
        }
    }
}

```

```

        count++;
    }
    /*else {
        bmpdata[count] = 255;
        count++;
        bmpdata[count] = 255;
        count++;
        bmpdata[count] = 255;
        count++;
    } */

    }
    rawfiledata[index] = (short)rawdata[i][j];
    index++;
}
}

MainForm->Caption = "Converting File...Please Wait";

MainForm->Caption = "Image Maker...File Converted";

Save1->Visible = true;

ConvertFile->Visible = False;

}
//-----

void __fastcall TMainForm::Save1Click(TObject *Sender)
{
    MainForm->Caption = "Image Maker";

    //SaveImage->InitialDir = "C:\\Documents and Settings\\Mark L. Adams\\My Documents\\My Pictures\\Absorption
Data";
    SaveImage->FileName = infilename;

    //if(SaveImage->Execute()){
        outfilename = SaveImage->FileName + ".bmp";
        rawfilename = SaveImage->FileName + ".raw";
    //}

    out.open(outfilename.c_str(),ios::out|ios::binary);
    if (out.fail()) {
        //report error message
    }

    //out.write((char *)&bmfh, sizeof (bmfh));
    out.write((char *)&bmfh.type, sizeof (bmfh.type));
    out.write((char *)&bmfh.size, sizeof (bmfh.size));
    out.write((char *)&bmfh.reserved1, sizeof (bmfh.reserved1));
    out.write((char *)&bmfh.reserved2, sizeof (bmfh.reserved2));
    out.write((char *)&bmfh.offset, sizeof (bmfh.offset));
    out.write((char *)&bmi, sizeof (bmi));
    out.write((char *) bmpdata, bmpsize);
    out.close();

    raw.open(rawfilename.c_str(),ios::out|ios::binary);
    if (raw.fail()) {
        //report error message
    }

    raw.write((char *) rawfiledata, rawsize);
    raw.close();

    Save1->Visible = false;

```

```

}
//-----

void __fastcall TMainForm::Close1Click(TObject *Sender)
{
    MainForm->Caption = "Image Maker";
    ConvertFile->Visible = false;

    in.close();
    out.close();
    raw.close();
    Close1->Visible = false;
    Open1->Visible = true;

    for (int j = 0; j < wval; j++)
        //for (k = 0; k < gridYext; k++)
            delete[] rawdata[j]; // STEP 2: DELETE THE ROWS
    delete[] rawdata;
    delete[] rawfiledata;
    delete[] bmpdata;
}
//-----

void __fastcall TMainForm::Batch1Click(TObject *Sender)
{
    int fileindex = 0;

    while (!stop) {

        infilename = edInitDir->Text+IntToStr(fileindex);

        in.open(infilename.c_str());
        if (in.fail()) {
            //open failed
            stop = true;
            MainForm->Exit1Click(MainForm);
        }

        Open1->Visible = false;
        Close1->Visible = true;

        in >> noskipws;

        in >> height;
        in >> inbyte >> inbyte >> inbyte;
        in >> width;
        in >> inbyte >> inbyte;

        IHval->Text = IntToStr((int)height);
        IWval->Text = IntToStr((int)width);

        hval = StrToInt(IHval->Text);
        wval = StrToInt(IWval->Text);

        rawsize = hval*wval;
        bmpsize = rawsize*3;

        try {
            // TEST FOR EXCEPTIONS.
            rawdata = new float*[hval]; // Step 2: Set up the rows
            for (int j = 0; j < wval; j++) {
                rawdata[j] = new float[wval]; // STEP 2: SET UP THE COLUMNS
            }
            rawfiledata = new short[rawsize];
            bmpdata = new unsigned char[bmpsize];
        }
    }
}

```

```
    }  
    catch (std::bad_alloc) { // ENTER THIS BLOCK ONLY IF bad_alloc IS THROWN.  
        // YOU COULD REQUEST OTHER ACTIONS BEFORE TERMINATING  
        //lblEM->Caption = "Could not allocate. Bye ...";  
        //lblEM->Visible = true;  
        exit(-1);  
    }  
  
    MainForm->Caption = "Loading Data...Please Wait";  
  
    for (int i = 0; i < hval; i++) {  
        for (int j = 0; j < wval; j++){  
            in >> rawdata[i][j];  
            in >> inbyte;  
        }  
    }  
  
    MainForm->Caption = "Image Maker";  
    ConvertFile->Visible = true;  
    in.close();  
  
    MainForm->ConvertFileClick(MainForm);  
    MainForm->Save1Click(MainForm);  
    MainForm->Close1Click(MainForm);  
  
    fileindex++;  
}  
}  
//-----
```